THE CHAOS DETECTOR AND COMMISSIONING RESULTS

By

Mohammad Arjomand Kermani

B.Sc., The University of British Columbia, 1991

A THESIS SUBMITTED IN PARTIAL FULFILLMENT OF

THE REQUIREMENTS FOR THE DEGREE OF

MASTER OF SCIENCE

IN

THE FACULTY OF GRADUATE STUDIES

DEPARTMENT OF PHYSICS

WE ACCEPT THIS THESIS AS CONFORMING

TO THE REQUIRED STANDARD

THE UNIVERSITY OF BRITISH COLUMBIA

DECEMBER 1993

In presenting this thesis in partial fulfilment of the requirements for an advanced degree at the University of British Columbia, I agree that the Library shall make it freely available for reference and study. I further agree that permission for extensive copying of this thesis for scholarly purposes may be granted by the head of my department or by his or her representatives. It is understood that copying or publication of this thesis for financial gain shall not be allowed without my written permission.

(Signature)

Department of Physics

The University of British Columbia
Vancouver, Canada

Date Dec 6, 1993.

DE-6 (2/88)

Abstract

The Canadian High Acceptance Orbit Spectrometer (CHAOS), which is a 360 degree magnetic spectrometer designed for use in various πN experiments, is introduced. The physics program, constituent elements of the detector, analysis techniques, and commissioning results are discussed. In particular, $\pi^+ p$ elastic scattering data acquired at an incident pion energy of 280 MeV with a singles trigger on a liquid hydrogen target are presented.

Table of Contents

List of Tables

List of Figures

Acknowledgements

There are many people who deserve thanks, however to list them all would require a book in itself. I would like to say thanks to my supervisor of many years, Dr. Greg Smith, for his help and guidance and the late nights he had to spend reading this thesis. In addition, I would like to thank my co-reader Dr. Garth Jones. I want to say a special thanks to the following people whose help is greatly appreciated: Pierre Amaudruz, Jeff Brack, Gertjan Hofman, Doug Maas, Martin Sevior, and Roman Tacik. I would also like to acknowledge the efforts of Faustino Bonutti, Paolo Camerini, Nevio Grion, Dave Ottewell, and Rinaldo Rui during the running period, which at the time seemed to have no end. I also want to thank my friends Chris König, Alan Poon, and Dean Featherling. Finally I would like to thank my mother Salehe, my father Mehdi, and Sheila McFarland for their support through the years.

Chapter 1

Introduction

The field of particle physics has made great advances in the past fifty years. The design and construction of new detectors and laboratories along with the development of powerful theories has allowed us to understand a great deal about the building blocks of nature. However an enormous amount is still unknown. To date the most complete model of particle physics provides the following classification for the basic building blocks of nature:

$$\begin{pmatrix} e \\ \nu_e \end{pmatrix} \begin{pmatrix} \mu \\ \nu_\mu \end{pmatrix} \begin{pmatrix} \tau \\ \nu_\tau \end{pmatrix} \quad (Lepton\ family)$$

$$\begin{pmatrix} u \\ d \end{pmatrix} \begin{pmatrix} c \\ s \end{pmatrix} \begin{pmatrix} t \\ b \end{pmatrix} \quad (Quark\ family)$$

All interactions studied in particle physics take place between the above families and are mediated by the strong, weak, electromagnetic, and gravitational forces. The strong interactions take place between the quark constituents that make up the hadrons. Since before the start of the meson factories the pion has been used as a probe to study the strong force, and a great deal of physics has been learned from the interactions of pions with nucleons. The Canadian High Acceptance Orbit Spectrometer (CHAOS) built at TRIUMF will study various πN reactions. This unique new device is a 360 degree magnetic spectrometer capable of making simultaneous measurements over the entire

angular region. The CHAOS physics program and detector will be described and recent commissioning results will be presented in this thesis.

1.1 The Physics Program

The major objective of CHAOS is to study the πN system. These measurements will be used to determine scattering amplitudes and scattering lengths which are needed to test QCD models. The physics program can be divided into two parts: the πp program and the $(\pi, 2\pi)$ program. Each of these programs will be discussed in this section.

1.1.1 The $\pi^{\pm}p$ Program

The aim of this program is to measure analysing powers for elastic $\pi^{\pm}p$ scattering at low incident pion energies. The analysing power for a given reaction on a spin 1/2 target with its spin polarized perpendicular to the reaction plane (along the unit vector $\hat{P}$) and a spin zero projectile of a given momentum along the unit vector $\hat{K}_{in}$ is defined as the following:

$$A(\theta) = \frac{N_r - N_l}{N_r + N_l}\frac{1}{P} \tag{1.1}$$

where N_r and N_l represent the number of particles scattered to the right and the left at a given scattering angle θ and P is the magnitude of the target polarization. In addition, left is defined along the vector pointing in the direction of $\hat{P} \times \hat{K}_{in}$.

In the case of two identical detectors one would be able to make this measurement by simply placing the two detectors on either side of the polarized target. However this is not an easy task since the measurement is extremely sensitive to instrumental asymmetries. Instead one can measure the analysing power by determining the differential cross section at a given scattering angle for positive and negative target spin polarizations. The latter approach is much less prone to instrumental asymmetries.

Polarizations	$\hat{P} \cdot (\hat{K}_{In} \times \hat{K}_{Out})$
+	1
-	-1

Table 1.1: Table showing polarization definitions

Positive and negative polarizations are defined in table 1.1. In this table $\hat{K}_{Out}$ represents the unit vector along the direction of momentum of the scattered particle. In this case the analysing power is given by

$$A(\theta) = \frac{\sigma^+(\theta) - \sigma^-(\theta)}{p^-\sigma^+(\theta) + p^+\sigma^-(\theta)} \tag{1.2}$$

In the above equation $\sigma^+(\theta)$ and $\sigma^-(\theta)$ are the differential cross sections at positive and negative target polarizations, and likewise p^+ and p^- are the magnitudes of the positive and negative polarizations. The analysing power is sensitive to the interference between the spin flip and the non spin flip components of the scattering amplitude, whereas the cross section is a measurement of the incoherent sum of the squares of these terms.

It is true that πN scattering amplitudes can be extracted from the absolute differential cross section and spin-dependent measurements via partial wave analysis (PWA). However the existing cross section data below 100 MeV are not consistent and since the phase shifts are obtained by fitting the measured cross sections using a partial wave expansion it is clear that the phase shifts will be inconsistent as well. A brief review of $\pi^{\pm}p$ scattering experiments is as follows. In 1953 H.L. Anderson and E.Fermi et. al. [1] were the first to measure $\pi^{\pm}p$ differential cross sections. The next thorough study did not occur for another twenty years. In 1973 Bussey et. al. [2] made an extensive set of $\pi^{\pm}p$ measurements between 88 and 292 MeV; in 1976 π^+p data at energies below 100 MeV were obtained by Bertin et. al. [3]. At this point different measurements seemed to be

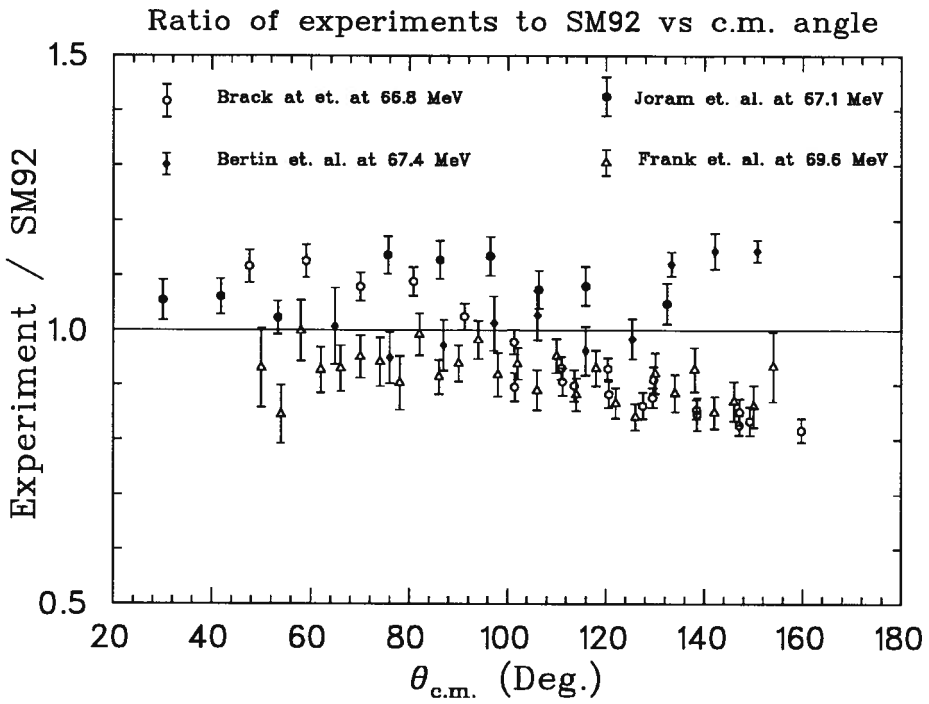

Figure 1.1: Figure showing the ratio of the various measured cross sections to the SM92 phase shifts near 67 MeV.

consistent with each other. In 1978 yet another study was done by E.Auld et. al. at 48 MeV [4]; however the Auld data did not agree with the phase shifts that were extracted using the previous two experiments. In the years that followed more data were obtained by Frank [5], Ritchie [6], Brack [7][8], and Joram [9] and further disagreement surfaced. An example of the discrepancy at 67 MeV is shown in figure 1.1. The absolute differential cross section at a given scattering angle θ can be obtained from the experimental data using the following relation.

$$\frac{d\sigma}{d\Omega}(\theta) = \frac{Yield(\theta)\cos(\theta_{tgt})}{N_i N_{tgt} d\Omega \epsilon} \tag{1.3}$$

Where θ_{tgt} is the target angle with respect to the incident beam, N_{tgt} is the number of target particles per unit area. N_i represents the number of incident particles, $d\Omega$ is the solid angle defined by the detector and ϵ is the detection efficiency. In the case of an absolute measurement all the above parameters must be known accurately and any systematic errors will directly translate into an error in the cross sections. In an analysing power measurement, most of these factors need not be known absolutely if one can rely on the fact that they stay the same for both target polarizations. Hence, an analysing power measurement is not sensitive to the same normalization problems encountered when making an absolute differential cross section measurement. Thus the $\pi^{\pm}p$ analysing powers measured with CHAOS will place an extra constraint on the partial wave analysis. This will be crucial in resolving the current impasse with the cross sections as well as providing a more sensitive measure of the smaller partial waves. The amplitudes obtained from the PWA can then be used to calculate the pion nucleon sigma term, discussed in a later section.

1.1.2 The (π,2π) program

The aim of this program is to study $\pi N \rightarrow \pi\pi N$ reactions for a wide range of energies and various nuclei. Further measurements of $(\pi, 2\pi)$ differential cross sections on nuclei will be used to study effects arising from the nuclear medium. There has been some discussion regarding the enhancement of the cross section due to nuclear matter for complex nuclei such as lead. The primary goal of this experiment is, however, to study the following reactions at energies close to threshold for pion production:

$$\pi^+ p \rightarrow \pi^+ \pi^+ n$$

$$\pi^+ p \rightarrow \pi^+ \pi^0 p$$

$$\pi^- p \rightarrow \pi^- \pi^0 p$$

$$\pi^- p \rightarrow \pi^+ \pi^- n \tag{1.4}$$

The amplitudes obtained from the above can then be related to the $(\pi\pi)$ scattering lengths. This will provide a good test of low energy QCD models. The theoretical perspective is briefly discussed in the next section.

1.2 Theoretical Perspective

Quantum Electrodynamics (QED) is perhaps the most successful theory describing interactions between elementary particles. The success of QED is demonstrated, for example, by the very precise agreement between the theoretical and experimental values of the electron and the muon anomalous magnetic moments. It seems logical to use QED techniques to study the strong force. The corresponding theory of the strong interactions is Quantum Chromo Dynamics (QCD); however, significant differences exist between the two theories. In QED the interactions are mediated by photons; in QCD this task is performed by gluons. The photon is neutral and thus is not capable of self interactions. The gluon, on the other hand, although electrically neutral carries the strong color charge and thus acts as a field source. In other words gluon-gluon vertices are allowed in QCD. The fact that gluons self interact makes QCD calculations difficult. The other major difference is in the magnitude of the coupling constant. The strong coupling constant, α_s is dependent on the energy scale and the momentum transfer. To first order the strong coupling constant can be written as [10]:

$$\alpha_s(Q^2) = \frac{12\pi}{(33 - 2n_f) ln(\frac{Q^2}{\Lambda})} \tag{1.5}$$

where Q^2 is the absolute value of the momentum transfer squared, n_f is the number of quark flavors involved in the interaction and Λ represents the energy scale, thought to

be in the range of 50 to 500 MeV [1]. It is clear that as $Q^2 \rightarrow \infty$ the coupling constant vanishes and thus perturbations in the coupling constant are acceptable. However in the low energy region (E $\leq$ 1GeV) the coupling constant is large and perturbation theory is no longer useful. This is why QCD symmetries have to be exploited.

1.2.1 Symmetries

The concept of symmetries is used widely in physics. It is a powerful tool that sometimes allows one to simplify and solve otherwise impossible problems. An entity is said to be symmetric under a given transformation if that entity is unchanged after the transformation has been performed. For example the Minkowski-space dot product $x_\mu x^\mu$ is invariant under a Lorentz transformation.

To a given symmetry corresponds a conserved quantity. For example, in classical mechanics translational invariance results in conservation of momentum, and time translation symmetry yields conservation of energy. The concepts of symmetry and conservation also hold in quantum field theory and this is manifested in the form of Noether's theorem. Consider a lagrangian density $\mathcal{L}(\phi^a(x), \partial_\mu \phi^a(x))$ and the following transformation:

$$\phi^a(x) \rightarrow \phi^a(x) + \delta\phi^a(x) \tag{1.6}$$

where $\phi^a(x)$ is the field. The above transformation results in

$$\mathcal{L} \rightarrow \mathcal{L} + D\mathcal{L} \tag{1.7}$$

where $D\mathcal{L}$ is given by the equation 1.8.

$$D\mathcal{L} = \sum_a \left((\frac{\partial \mathcal{L}}{\partial \phi^a})\delta\phi^a + \frac{\partial \mathcal{L}}{\partial(\partial_\mu \phi^a)}\delta(\partial_\mu \phi^a) \right) \tag{1.8}$$

The theory described by $\mathcal{L}$ is said to be invariant if

$$\delta S = \int d^4x D\mathcal{L} = 0 \tag{1.9}$$

[1] Λ is a renormalization group parameter.

where δS is the variation in the action. The above equation holds if

$$D\mathcal{L} = \partial_\mu F^\mu \tag{1.10}$$

where F is a differentiable function. In this case, Noether's theorem states that there are associated conserved currents given by the following:

$$\mathcal{J}^\mu = \sum_a (\Pi^{a\mu}\delta\phi^a - F^\mu) \tag{1.11}$$

where

$$\Pi^{\mu a} = \frac{\partial\mathcal{L}}{\partial(\partial_\mu\phi_a)} \tag{1.12}$$

Using equations 1.8 and 1.10 it can easily be shown that $\partial_\mu\mathcal{J}^\mu$ vanishes. Therefore, $\mathcal{J}^\mu$ is the conserved current.

1.2.2 Spontaneous Symmetry Breaking

The best way to get an understanding of spontaneous symmetry breaking (SSB) is via an example. A typical example is that of magnetic domains. The hamiltonian for a system having spins $\vec{S}_i$ is given by the following:

$$H = \frac{-\lambda}{2}\sum_{i,j}\vec{S}_i \cdot \vec{S}_j \tag{1.13}$$

It is clear that the above hamiltonian is symmetric under rotations and that the ground state of the system occurs when all of the spins are aligned. Invariance of H under rotations implies that there exists an infinite number of ground states related to each other by a rotation. However each of those states are not rotationally invariant; and the physical ground state was chosen by some initial condition or interaction with the rest of the universe. This is an example of SSB; the original hamiltonian displayed rotational symmetry but the ground state does not. The implications of SSB were studied by Goldstone, who suggested that massless particles (Goldstone bosons) appear when a

continuous symmetry is spontaneously broken. In the case of the magnetic domains example, these are called spin waves. This is when the spins in each domain vary in a wave like configuration with wave length λ. As $\lambda \to \infty$ a rotation of all the spins in the system is performed; since the system has rotational symmetry this does not require any energy and for large λ, $E \sim \frac{c}{\lambda}$ [12]. Here c is the speed of light. This corresponds to a massless particle as predicted by Goldstones's theorem. At this point a valid question is whether the Goldstone bosons seen in nature are massless. The answer is no; often the original lagrangian does not have complete symmetry. In other words, there is a small part that explicitly breaks the symmetry so that it is an approximate one. This phenomenon causes the Goldstone modes to acquire mass.

1.2.3 Chiral Symmetry

Consider the QCD lagrangian for the light quarks (ie: u, d, s) [11].

$$\mathcal{L}_{QCD} = \bar{q}i\gamma^{\mu}(\partial_{\mu} - iA_{\mu})q + M\bar{q}q \tag{1.14}$$

where A_{μ} is the gluon field, q is the column vector consisting of u, d and s, and M is a 3×3 diagonal matrix consisting of the masses of the three quarks. Now consider the limiting case of zero quark masses and define the following:

$$\Gamma_{L,R} = (1 \pm \gamma^5) \tag{1.15}$$

$$q_L = \Gamma_L q \tag{1.16}$$

$$q_R = \Gamma_R q \tag{1.17}$$

where the subscripts R, L correspond to the right and left handed quarks and projection operators. Using the above form for Γ_L, Γ_R it is clear that the quark field, q can be written as $q = q_L + q_R$. Thus in the limit of zero quark masses in equation 1.14 the right and the left handed quarks are decoupled; in other words there is a symmetry of

handedness. In the limit of zero quark masses the theory described by 1.14 exhibits *chiral symmetry* [2].

According to Noether's theorem there are 8 conserved axial vector and 8 conserved vector currents. Chiral symmetry also indicates that there are many different possible combinations of left and right handed quarks of equal energy that form the ground state of the system. In this case one would expect to observe particle multiplets (particles of same mass but opposite parity), however this does not appear in nature. The proton does not have a partner of the same mass and opposite parity; this indicates that *chiral symmetry is spontaneously broken.* Since SSB occurs there must exist Goldstone bosons and these are (π, K, η). Clearly all of the Goldstone modes mentioned have mass. So, is the chiral symmetry argument incorrect? Recall that 1.14 was chirally symmetric in the limit of zero quark masses but in reality the nonzero quark masses *explicitly break* this symmetry and as a result the Goldstone modes acquire mass.

At low energies the constraints imposed by chiral symmetry are employed in terms of an effective theory. In the effective lagrangian, $\mathcal{L}_{eff}$, the concepts of chiral symmetry parity, unitarity and all other symmetries of the original lagrangian are manifest. The explicit symmetry breaking terms arising from the light quark masses are then treated in a perturbative fashion; this is the framework of *chiral perturbation theory (CHPT).*[3] In the effective theory chiral symmetry is spontaneously broken and the Goldstone bosons in the form of pions appear. In the framework of the effective lagrangian and CHPT the S wave isospin zero scattering length for (π π) scattering to leading lowest order is given by equation 1.18 [11]:

$$a_0^0 = \frac{7m_\pi^2}{32\pi F_\pi^2} \tag{1.18}$$

[2]It is invariant under $q_L \rightarrow \Gamma_L q_L$ and $q_R \rightarrow \Gamma_R q_R$.

[3]The quark mass expansion is not the ordinary Taylor expansion. It also includes nonanalytic terms [11].

where m_π is the pion mass and F_π is the pion decay constant. Since colliding pion beams and meson targets do not exist one has to use reactions like $\pi + N \rightarrow \pi\pi N$ to obtain this information. This is a major goal of the $(\pi, 2\pi)$ program. Using this information, one can perform a good test of CHPT and the low energy effective theory of strong interactions.

1.2.4 The πN sigma term

The σ term is a measure of the explicit breaking of chiral symmetry in the QCD lagrangian, and it is defined as [11]:

$$\sigma = \frac{M}{2m_p} < p|\bar{u}u + \bar{d}d|p > \tag{1.19}$$

where $|p>$ is the single proton state, m_p is the proton mass and $M = \frac{1}{2}(m_u + m_d)$. In order to understand how this quantity is related to the πN scattering amplitudes, define [11]

$$\Sigma = F_\pi^2 \bar{D}(\nu = 0, t = 2m_\pi^2) \tag{1.20}$$

where $\bar{D}$ is the πN scattering amplitude without the Born term, $\nu = (s - u)/4m_p$, and s, t, u are the usual Mandelstam variables. This unphysical point (ie: choice of ν and t) is called the Chang-Dashen point. The relation between Σ and σ is a complex one and will not be discussed here; it suffices to say that these two parameters are related at the Chang-Dashen point via CHPT. Using the baryon mass spectrum the value of σ has been calculated to be [11]

$$\sigma = \frac{35 \pm 5MeV}{1 - y} \tag{1.21}$$

where the variable y is given by

$$y = \frac{2 < p|\bar{s}s|p >}{< p|\bar{u}u + \bar{d}d|p >} \tag{1.22}$$

In other words y determines the *strange quark content of the proton.* Work done by Gasser, Leutwyler and Sainio has determined the value of Σ to be 60 MeV; this indicates

that $\sigma = 45$ MeV, thus making $y \approx 0.2$ [11].

The πN scattering amplitudes measured with CHAOS will be used to calculate y and test yet another prediction of CHPT.

Chapter 2

A Brief Description of CHAOS

The CHAOS physics program was discussed in the last chapter. In this chapter, a brief description of the detector will be provided and some of the technical details will be discussed. The CHAOS detector consists of a cylindrical dipole magnet, a solid, cryogenic, or polarized target located at the center, four cylindrical wire chambers (WC1, WC2, WC3, WC4) for particle tracking, and an array of scintillators and lead glass Cerenkov counters. This is shown in figure 2.2.

The design of the spectrometer was primarily driven by the physical constraints imposed by small cross sections, large backgrounds and the need to resolve nuclear final states.[1] These factors combined require the momentum resolution of the detector to be ($\Delta P/P \leq 1\%$), and the incident beam rate capability $\geq$ 5 MHz.

Since the majority of the reactions to be studied have small cross sections, it is crucial to maximize the angular coverage of the detector. The existence of large backgrounds necessitates coincidence mode operation and the ability to perform fast hardware rejection of unwanted events. These two factors are clearly seen in the following examples. The $\pi^{\pm}p$ reaction requires the use of a polarized target; however since liquid hydrogen can not be polarized, one is forced to use molecules which contain other nuclei such as carbon and oxygen. This leads to high background in addition to that caused by the interaction of the pions with the target cryostat. All of the backgrounds mentioned can virtually be eliminated if the recoil proton is detected in coincidence with the scattered pion. In the

[1]Some of the proposed measurements are experiments whose goal is to study nuclear structure.

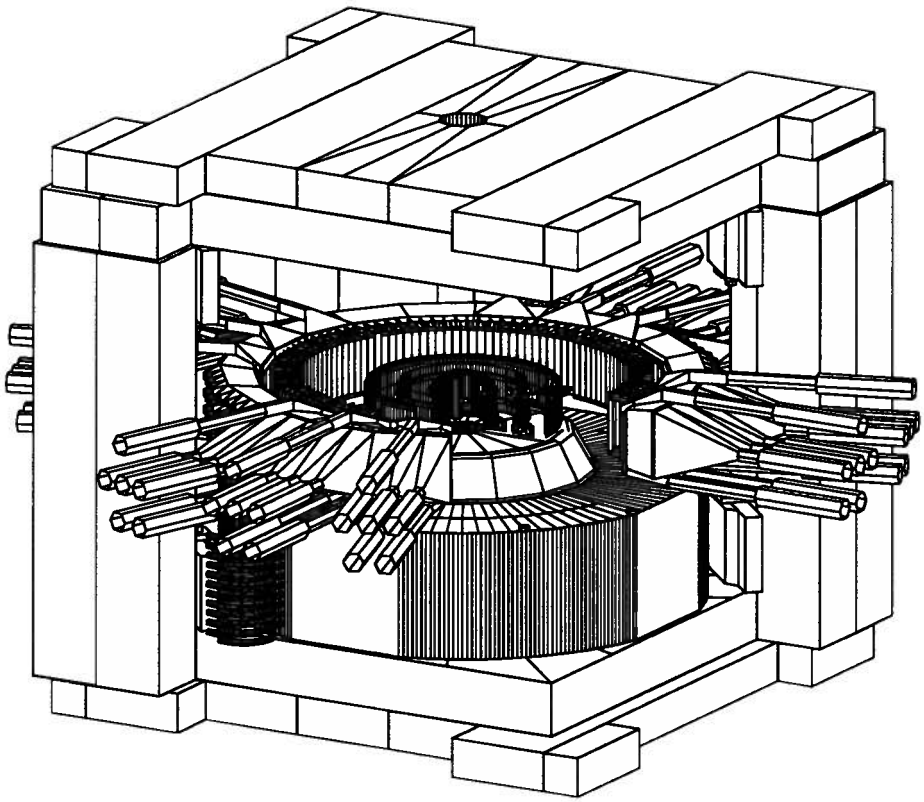

Figure 2.2: Figure showing the CHAOS spectrometer. The corner post and the top pole tip have been removed to allow for a better view. For the same reason, a quadrant of the detectors is cutaway.

case of the $(\pi, 2\pi)$ reaction a large source of background is elastic πp scattering. As a result the detector must have the ability to perform hardware rejection of these events. All of the criteria mentioned have put constraints on the design of CHAOS.

2.1 Monte Carlo

Extensive simulations using the CERN Monte Carlo program GEANT were done prior to construction of CHAOS. These studies indicated the best design for the various detectors in the spectrometer given the physics constraints. Simulations provided information on chamber radii for optimum momentum resolution. The resolution was also studied for different chamber materials. For example, figure 2.3 shows the momentum resolution as a function of the third wire chamber radius. GEANT simulations also aided in the design of the scintillator-Cerenkov counter arrays. Monte Carlo studies were done in order to study the interaction of the incoming pion beam with elements inside the spectrometer; pion decay inside CHAOS was also studied in detail. These two processes are of crucial importance since they present a source of background.

The first phase of simulations are now complete and the second phase has begun. This stage deals with the physics aspects. Simulations are required to obtain the effective solid angle for the spectrometer and assess the feasibility of future experiments given the design of CHAOS.

2.2 The Magnet & Polarized Target

The CHAOS physics program does not require 4π solid angle coverage, and the knowledge of the incident beam is crucial during reconstruction; thus a cylindrical geometry oriented transverse to the beam is ideal. In addition, large angular coverage and good momentum resolution at all angles rules out longitudinal magnetic field direction. Perhaps the most

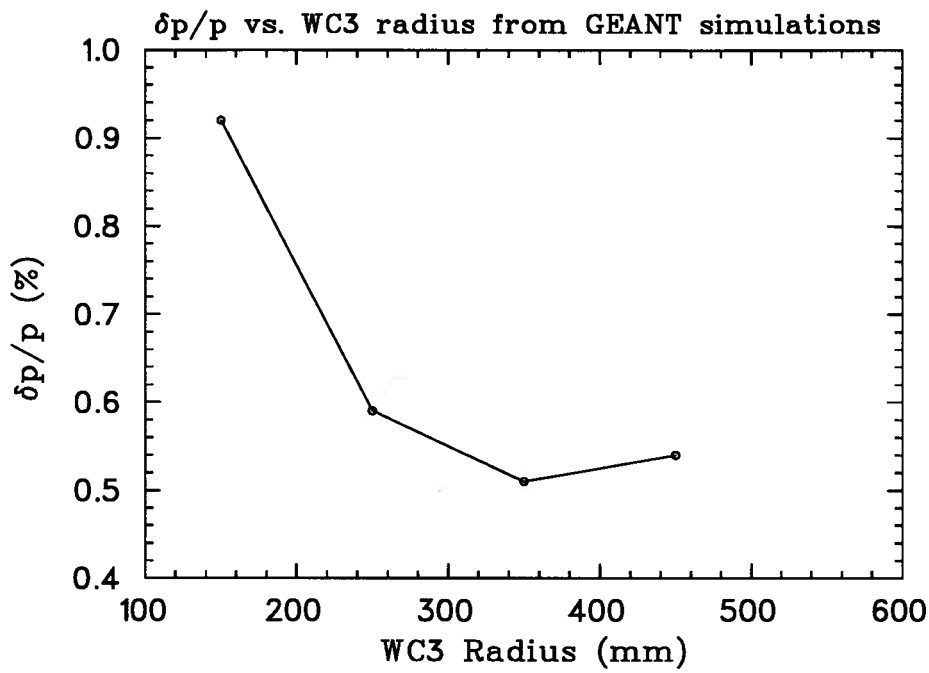

Figure 2.3: Results of GEANT simulations are shown. This simulations were done for detectors in helium surroundings.

important factor in using the current magnet for CHAOS was cost. The magnet was built by upgrading an existing one. The CHAOS dipole magnet is capable of producing fields up to 1.6 T, and the field map for 0.95 T central field setting is shown in 2.4. A bore hole along the symmetry axis accommodates the cryogenic or polarized target. The magnet must be capable of producing a uniform field up to and including the radius of the third wire chamber. This is important since in a uniform field the momentum of a charged particle can be obtained analytically using three points on its trajectory. Large amounts of iron are required in order to reduce the fringe field which would otherwise cause difficulties with the operation of the photomultiplier tubes in the vicinity. The magnet must be accessible and must have the ability to translate and rotate so that the

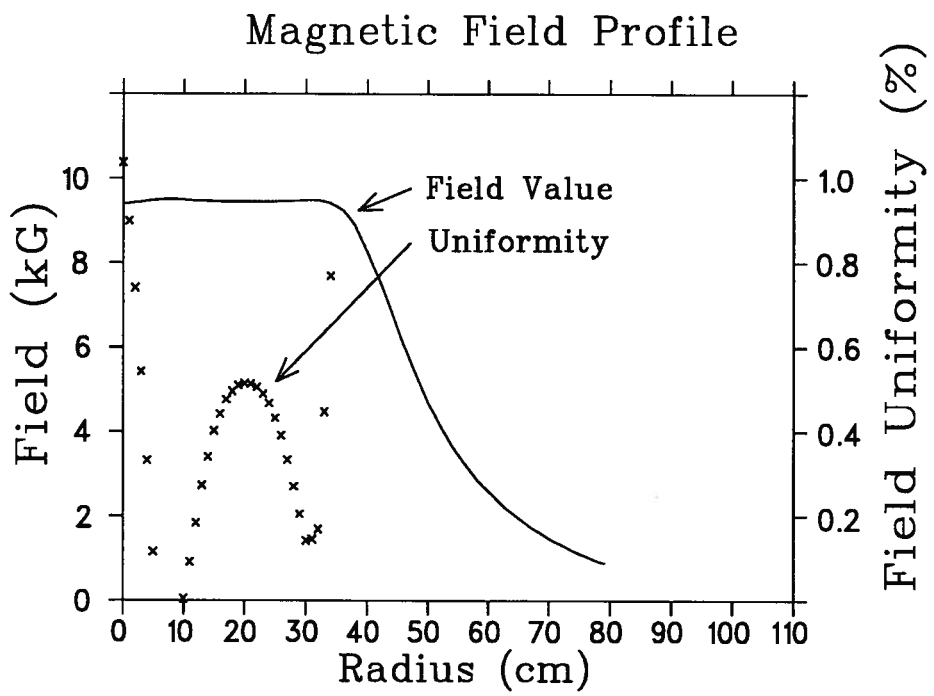

Figure 2.4: The CHAOS field map for 0.95 T central field setting is shown. The solid line shows the field value as a function of the distance from the center of the spectrometer, and the crosses denote the field uniformity.

incident beam hits the target located at the center.

A major limitation placed on the polarized target is that it must fit through the bore hole along the axis of the magnet. Since polarization requires an extremely uniform field, the target must be polarized outside of CHAOS and then lowered inside the spectrometer. The CHAOS field will then be used to operate it in frozen spin mode. The target is presently in the construction stage.

2.3 Tracking Detectors

The trajectory of the charged particles inside the spectrometer is measured with four independent multiwire chambers. The major constraint imposed on the design of the chambers stems from the need for good momentum resolution. This means that the chambers must deliver good spatial resolution. To reduce the contribution of multiple scattering to the momentum resolution, they must also be thin and have low mass. Thus, low density materials must be used in the construction, and obstructions such as supporting posts must be avoided. Small cross sections require that CHAOS be capable of operating at an incident beam flux of up to 5 MHz. This requires that at least two of the four chambers be able to operate at high rates. This is because two points on the incoming beam trajectory are needed for reconstruction purposes. As a result, the two inner chambers are high rate proportional chambers. In order to perform fast hardware rejection of unwanted events, at least three points are needed on the trajectory of an outgoing particle. Since only two points are required for the incident beam track, a drift chamber (deadened in the region of entrance and exit of the beam) is a suitable choice for the third CHAOS chamber. Note that this chamber must also be instrumented with a proportional chamber readout system to ensure the fast transfer of data between the chamber and the trigger electronics. Although a proportional chamber would also be a suitable candidate for the third chamber, the cost of instrumenting the device at such a large radius is far too high.

In principle, the information obtained from the three inner chambers is enough for track reconstruction. However, chamber inefficiencies may then cause the loss of many good tracks, since two points are not enough for track reconstruction. This is overcome by introduction of a vector drift chamber (jet chamber) as the outermost tracking detector in CHAOS. Since this is the last tracking device, multiple scattering associated with a

large volume is no longer a major concern. The large radius and good spatial resolution of this chamber help constrain particle trajectories and thus improve the momentum resolution. This chamber will provide a vector along the direction of the track, which is essential for sorting ambiguous tracks.

Three of the four chambers also provide information on the vertical coordinate of the track, which is useful in containing the events to the target region and providing a small out-of-plane correction for the measured momentum.

2.4 Particle Identification & Multiplicity

As mentioned before, large backgrounds are a major concern in nearly all CHAOS experiments and some of these backgrounds can be removed using coincidence detection; thus multiplicity information (ie: the number of tracks in a given event) is essential. There is also a need for particle identification, primarily pions, protons, and electrons. This is demonstrated in the following example. Recall that some of the reactions studied in the $(\pi, 2\pi)$ program have neutral pion final states. The π^0 will decay almost immediately after its creation and the photons produced can cause pair production in the target material. The electron positron pair imitates a two pion final state. Hence, it is crucial to be able to resolve pions from electrons. The multiplicity and particle identification information along with the track momentum can be used to perform offline rejection of unwanted events. This information is obtained by using the array of scintillators and lead glass counters. These counter telescopes are referred to as the Chaos Fast Trigger (CFT) counters.

2.5 Trigger & Readout Systems

As stated before it is of great importance to perform fast hardware rejections. This can be done in two stages; some of the unwanted events can be eliminated using only the multiplicity information from the CFT counters, where as the remainder must be eliminated using information obtained from the chambers. This requires the design of two levels of trigger for CHAOS. These will be referred to as the first and the second level trigger systems.

The readout system must be capable of fast data transfer between the detectors, the first and the second level triggers. For a given event, it must also be able to zero suppress channels which do not carry any information, since there are ≈ 4500 channels in total. A proportional chamber operating system (PCOS) is utilized for the first three chambers. The CFT counters are instrumented with both analog to digital converters (ADC's) and time to digital converters (TDC's). It is clear that all drift chambers must be equipped with TDC's; all of the chambers are also equipped with ADC's in order to obtain either vertical coordinate information or for use in resolving the left-right ambiguities in WC3.

Chapter 3

Wire Chambers 1 & 2

In this chapter, the two inner proportional chambers used in CHAOS are discussed and some recent commissioning results are presented. Before starting the discussion, it is appropriate to outline some basic concepts regarding the operation of multiwire proportional chambers (MWPC).

3.1 Basic Operating Principles

The first MWPC was built by Georges Charpak and his collaborators in 1967-68 [14]. This marked one of the most important achievements in experimental particle physics. Today, multiwire proportional chambers are used in virtually all particle physics experiments. A charged particle travelling in a gaseous medium will interact with the gas via electromagnetic interactions. The electromagnetic signature of the particle is exploited in gaseous particle detectors.

A charged particle traversing a gas will cause it to ionize, producing electrons and ions. Consider a thin metal wire (in the gas) surrounded by an outer conducting cylinder; a potential difference applied between these two conductors will result in an electric field. If the polarity of the two electrodes is chosen such that the wire is at a positive potential with respect to the outer cylinder, the electrons produced by the ionization will drift towards the anode wire, and the ions will drift towards the outer cylindrical cathode. Close to the wire (at distances on the order of several times the radius of the wire), the electric field will be strong enough to cause avalanche multiplication of electrons. As a

result a pulse is observed on the wire; at the same time, an induced pulse of opposite charge is produced on the surrounding cylinder. A multiwire proportional chamber has similar principles of operation but uses more than one wire. The wire spacing in these chambers is usually on the order of a few millimeters, which allows for operation at high rates.

3.2 Design & Construction

As mentioned before, low density materials must be used in the construction of CHAOS chambers. Various Monte Carlo studies using the simulation program GEANT were performed to obtain the momentum resolution for different chamber materials; these studies were also used to obtain the optimum chamber radii. In order to improve the momentum resolution it is necessary to obtain vertical as well as horizontal coordinate information; the two inner proportional chambers are designed to perform this task.

WC1 and WC2 are located at radii of 114.59 and 229.18 mm respectively, and each has a (half) gap of 2 mm. WC1 consists of 720 anode wires with a pitch (separation) of 1 mm, and WC2 also consists of 720 anode wires but has a pitch of 2 mm. This was done so that each chamber has an angular pitch of 0.5°. The chambers are each instrumented with 360 cathode strips inclined at 30 degrees with respect to the anodes.

Both chambers were built from two concentric cylinders of 1 mm thick rohacell held in place by G10 rings.[1] The inner cylinder consists of the anode wires and the inner cathode wall. Because of the small wire spacing, the anodes were directly soldered to cylindrical circuit boards which provide the high voltage and carry the signals to the preamplifier boards. The inner cathode wall was constructed by gluing a layer of 25 μm aluminized mylar, coated with graphite paint, on a 1 mm sheet of Rohacell. A layer of 12

[1]Rohacell is a low density material ($\rho = 50\ mg/cm^3$) similar to styrofoam.

μm kapton forms the other side of this wall. The anode wires are 12 μm diameter gold plated tungsten, and the wire tension of 10 grams is supported by the Rohacell frame.

The outer cylinder was also constructed from 1 mm thick Rohacell supported by G10 rings. In this case, the Rohacell was sandwiched between layers of 12 μm kapton and 25 μm Electro-Coated Nickel (ECN) foil, the latter one of which forms the cathode strips.[2] The strip pattern was etched on nickel plated kapton and glued onto the Rohacell. The cathode strips were connected to the readout circuit boards using gold plated spring clips. The inner cylinder was then placed inside the outer one, and the gap was sealed using a rubber tube. Two layers of 25μm double sided aluminized mylar were used to construct the flushing gas windows.

The anode wires are instrumented with 16 channel preamplifiers, LeCroy 2735 PC amplifier/discriminator cards, and the LeCroy Proportional Chamber Operating System (PCOS III). The cathode strips are connected to 8 channel preamplifiers, inverter/amplifier cards, and FASTBUS Analog to Digital Converters (ADC's). The inverter circuit was needed in order to provide the ADC's with a negative pulse. The gas used in both detectors is 80% CF4 and 20% isobutane. The performance of WC1 and WC2 along with some results are discussed in the next section.

3.3 Performance

In June 1993, the operation and performance of these two chambers were studied. Efficiencies as a function of voltage were studied to obtain the proper operating voltage. The efficiency of the chambers was calculated by analysing straight through beam events, and it is given by the following relation:

$$\epsilon = \frac{\sum_{i=2} N_i}{\sum_{i=0} N_i} \tag{3.23}$$

[2]The ECN foil is 25 μm kapton covered with 1200 $\AA$ copper and 300 $\AA$ nickel.

where N_i is the number of times i wires were activated. For a perfectly efficient chamber, two or more wires are activated in each event. Figure 3.5 shows the efficiency of each chamber as a function of the operating voltage. The WC1 voltage was chosen to be a conservative value of 2450 V, which resulted in lower chamber efficiency and smaller cathode strip pulse heights. WC2 was operated at 2050 volts, allowing for maximum efficiency. Rate studies were also performed at the nominal operating voltages. Figure 3.6 shows the efficiency as a function of incident beam rate.

The chamber efficiency will drop when the maximum operating rate is exceeded. This is due to the *space charge effect.* This phenomenon takes place when the number of ions produced around the wire becomes so large that it causes distortions in the electric field; consequently the chamber efficiency will decrease. Figure 3.7 shows the current drawn by each chamber as a function of the rate; the linear relation between the current and the rate indicates that discharge does not occur at high incident beam rates.

For a proportional counter, one can predict the optimum resolution the device is capable of providing; this quantity is predetermined by the wire spacing. The position of the hit in the chamber is quantized in terms of the wire closest to the track. In other words, no drift time information is used to obtain the coordinate of the hit. Let the wire spacing in a proportional chamber be l. Now consider a track passing within a distance of $l/2$ on either side of the wire (see figure 3.8); the position of this hit in the chamber is going to be given as the location of the nearest wire. This is governed with a uniform probability distribution given by

$$f(x) = \frac{1}{l} \tag{3.24}$$

Using the standard definition of the variance, the resolution of the chamber is given by

$$\sigma = \sqrt{\int_{-\frac{l}{2}}^{\frac{l}{2}} x^2 dx \frac{1}{l}} = \frac{l}{\sqrt{12}} \tag{3.25}$$

Thus a chamber with a pitch of 1 mm will have an optimum resolution of 288 μm. The

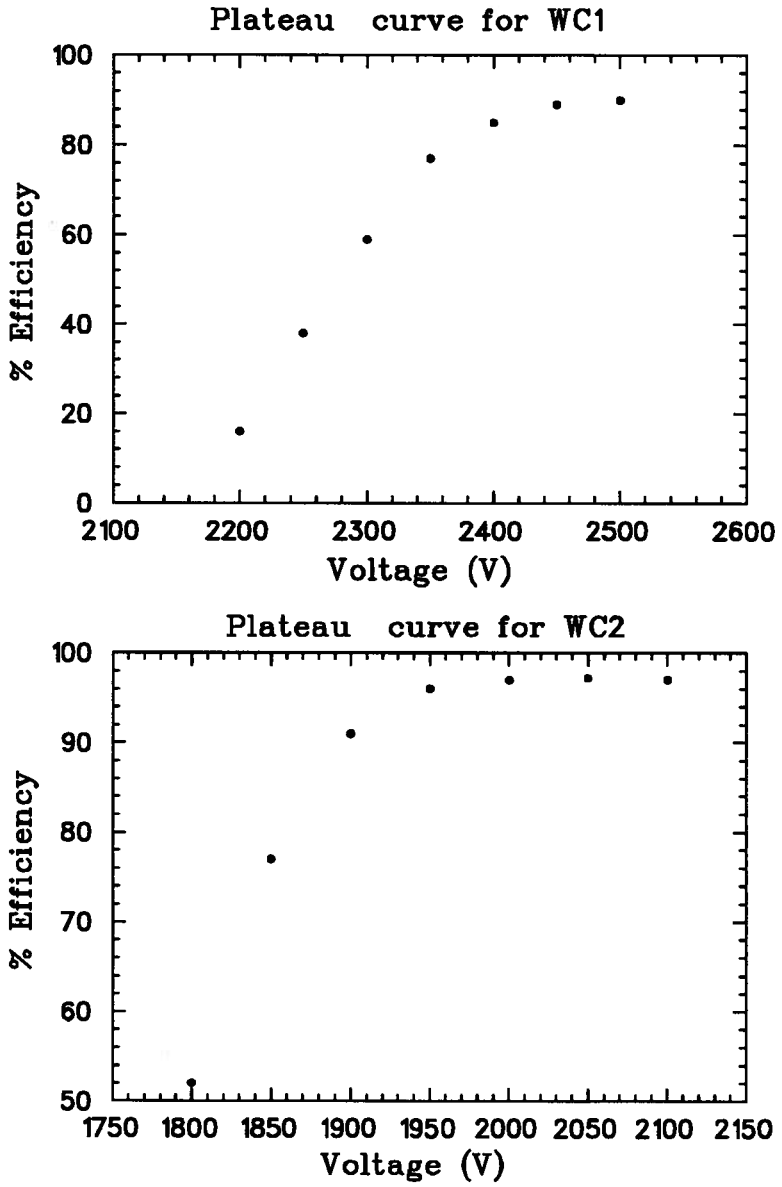

Figure 3.5: Plateau curves for WC1 and WC2 are shown. The data were acquired at a rate of $\leq$ 50 kHz, for 225 MeV/c π^-.

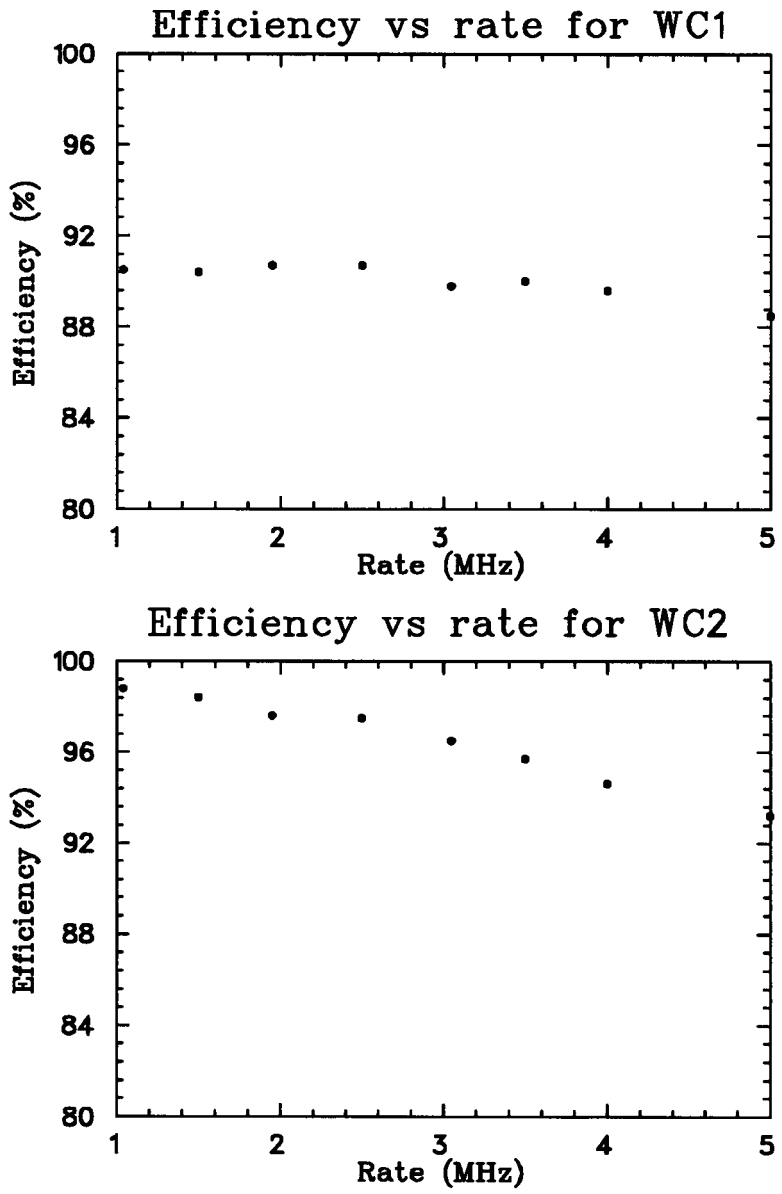

Figure 3.6: The efficiency of WC1 and WC2 as a function of the incident beam rate is shown for operating voltages of 2450 V for WC1 and 2050 V for WC2, acquired with 225 MeV/c π^-.

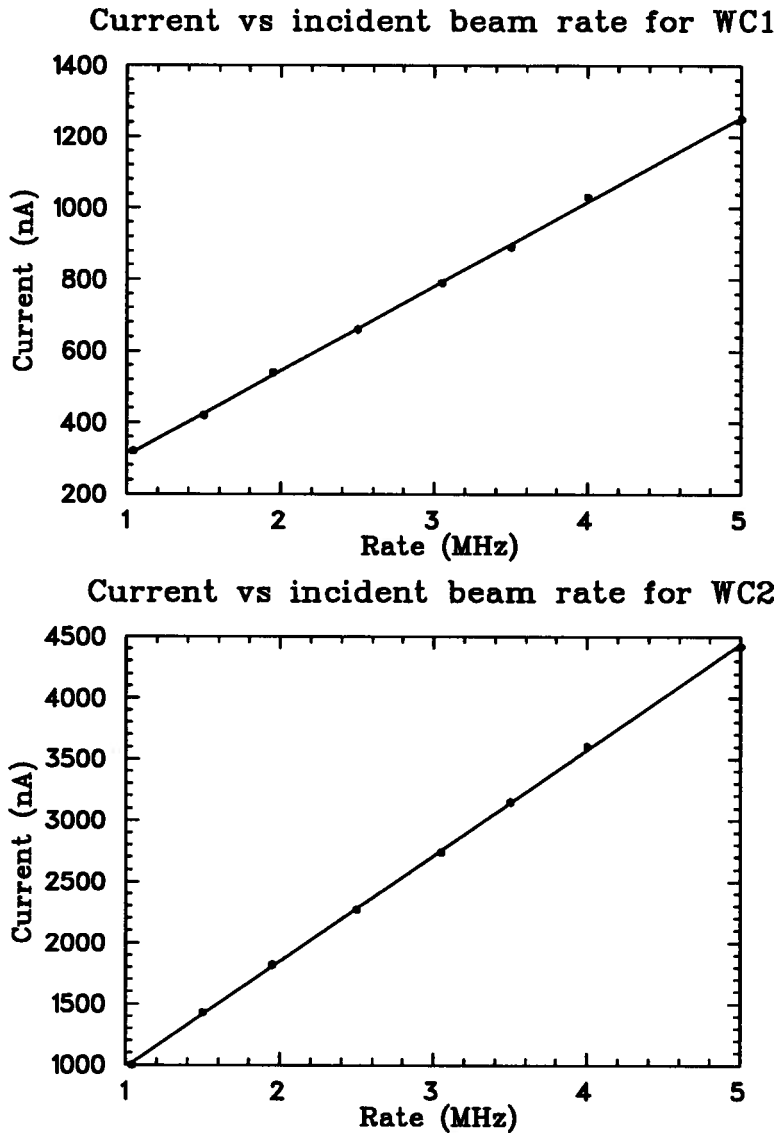

Figure 3.7: The current drawn by WC1 and WC2 versus beam rate is shown. The high voltage and beam conditions are the same as for figure 3.6. The solid curves are straight line fits.

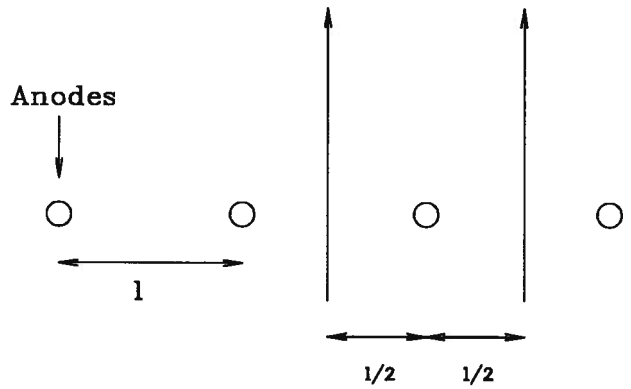

Figure 3.8: Figure showing tracks in a proportional counter.

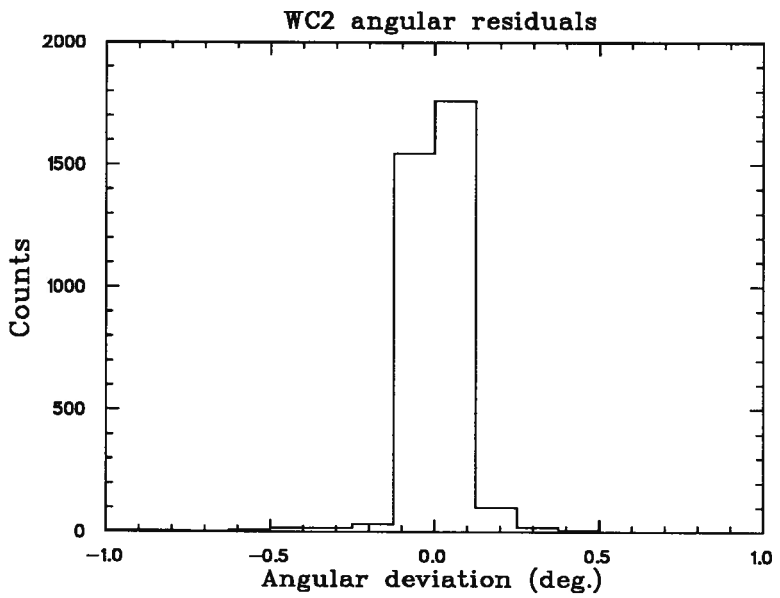

Figure 3.9: Figure showing angular residuals for WC2.

resolution of WC1 and WC2 is calculated by analysing straight tracks at zero magnetic field. All four chamber hits in WC1 and WC2 (two incoming and two outgoing) are fit to a straight line, and the intersection of the line with circles corresponding to the two chambers is obtained. The intersection points are the calculated positions of the hits. The angular deviation between the actual and calculated positions represents the chamber resolution. Figure 3.9 shows the angular resolution of WC2. For cases in which a cluster containing an even number of wires has been activated, PCOS will register the position of the hit to be half way between the two most central wires in the cluster. This is referred to as cluster mode operation, in which the effective angular and spatial pitch is half of the physical one. In figure 3.9, counts which correspond to angular deviations of more than $\pm 0.125°$ occur when only one wire fired, and deviations smaller than half of the angular pitch (0.25°) are due to cluster mode operation. Counts appearing at deviations greater than 0.25° constitute less than 2% of the total number of events considered and are due to pion decay. Both the singles and the cluster mode residuals are consistent with the angular spacing which is 0.5° for singles and 0.25° for cluster mode. In terms of spatial resolution the chamber provides 577 μm for singles and 289 μm for cluster mode operation.

In-plane position reconstruction is a very easy task using a proportional chamber. PCOS will provide a given wire number for each hit; since the radius of the wire plane is known one can associate an angular coordinate with each wire. From this point it is trivial to work out the position of the hit in the Cartesian coordinate system. An excellent test of the performance of the chambers would be to perform momentum calculations using only the information from the two inner chambers. This can be most easily accomplished by considering events for which the beam passes through the spectrometer without interacting, with nonzero CHAOS magnetic field. One can then use three out of the four hits in the proportional chambers to reconstruct the beam momentum. This is

possible since, given a uniform magnetic field, the trajectory of a charged particle in the field is a circle, which is completely defined by three points.

Let the coordinates of three points on a given circle be denoted by: (x_1, y_1), (x_2, y_2), (x_3, y_3). It is clear that the following equations hold:

$$(x_1 - a)^2 + (y_1 - b)^2 = R^2 \tag{3.26}$$

$$(x_2 - a)^2 + (y_2 - b)^2 = R^2 \tag{3.27}$$

$$(x_3 - a)^2 + (y_3 - b)^2 = R^2 \tag{3.28}$$

where a and b are the coordinates of the center and R is the radius of the circle. Solving the above three equations simultaneously, the center of the circle is given in terms of the following parameters:

$$R_i^2 = (x_i^2 + y_i^2) \quad (i = 1, 2, 3) \tag{3.29}$$

$$\Delta R_i^2 = (R_i^2 - R_{i+1}^2) \quad (i = 1, 2) \tag{3.30}$$

$$\Delta x_i = (x_i - x_{i+1}) \quad (i = 1, 2) \tag{3.31}$$

$$\Delta y_i = (y_i - y_{i+1}) \quad (i = 1, 2) \tag{3.32}$$

$$\tag{3.33}$$

The coordinate of the center is given by

$$a = \frac{\Delta y_1 \Delta R_2^2 - \Delta y_2 \Delta R_1^2}{2(\Delta y_1 \Delta x_2 - \Delta x_1 \Delta y_2)} \tag{3.34}$$

$$b = \frac{1}{\Delta y_1}\left[\frac{\Delta R_1^2}{2} - a\Delta x_1\right] \tag{3.35}$$

The radius of the circle, R, is then obtained by using the calculated values of a and b along with one of the original three equations. The momentum of a charged particle

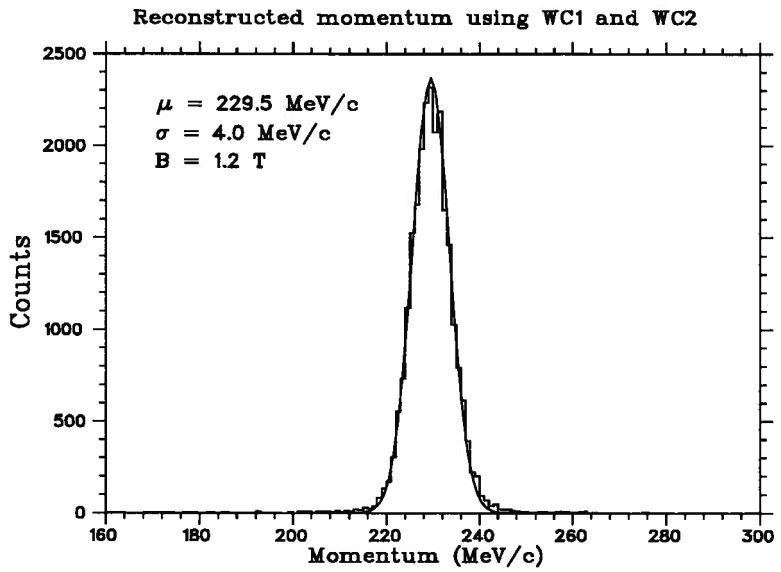

Figure 3.10: Figure showing calculated beam momentum using WC1 and WC2.

travelling in a uniform magnetic field is given by

$$P = qBR \tag{3.36}$$

where q is the charge and B is the magnitude of the field. With B in Tesla and R in mm, the momentum for a particle of unit charge in MeV/c is given by

$$P = 0.29979RB \tag{3.37}$$

Figure 3.10 shows the reconstructed momentum for a 230 MeV/c pion beam that exits the spectrometer without interacting. The agreement between the channel momentum and the reconstructed momentum is good. Using three out of the four hits recorded by these two chambers only, the momentum resolution is 1.8%.

The information obtained from WC1 and WC2 also allows one to reconstruct the incoming beam trajectory knowing its momentum and polarity along with the direction of the magnetic field. This is crucial for the reconstruction of the interaction vertex and

to the projection of the beam on the target. The procedure is discussed in the following paragraph.

Let the coordinates of the two incoming beam hits in WC1 and WC2 be denoted by (x_1, y_1) and (x_2, y_2). Furthermore, let P and q represent the beam momentum and polarity respectively. The beam momentum is known to an accuracy which depends on the slit settings used at the dispersed midplane focus of the channel. For all data acquired thus far with CHAOS, the slits were closed such that $\frac{\Delta P}{P} \leq 0.5\%$.

Given the field magnitude, the radius of curvature is obtained from equation 3.37. [3] Since the two hits lie on a circle, the following equations hold:

$$(x_1 - a)^2 + (y_1 - b)^2 = R^2 \tag{3.38}$$

$$(x_2 - a)^2 + (y_2 - b)^2 = R^2 \tag{3.39}$$

Again R is the radius of curvature and (a,b) is the center of the circle. Solving the above equations yields two possible solutions in terms of the following parameters:

$$\begin{aligned}
\Delta x &= x_2 - x_1 \\
\Delta y &= y_2 - y_1 \\
\alpha &= \frac{\Delta x^2 + \Delta y^2}{2\Delta y} \\
\beta &= \alpha^2 - R^2 \\
\gamma &= \frac{\Delta x}{\Delta y}
\end{aligned}$$

The solutions are given by

$$a = x_1 + \frac{\alpha\gamma \pm \sqrt{\alpha^2\gamma^2 - \beta(1+\gamma^2)}}{1+\gamma^2} \tag{3.40}$$

$$b = y_1 + \alpha + \gamma(x_1 - a) \tag{3.41}$$

[3] Uniform field assumption is once again used.

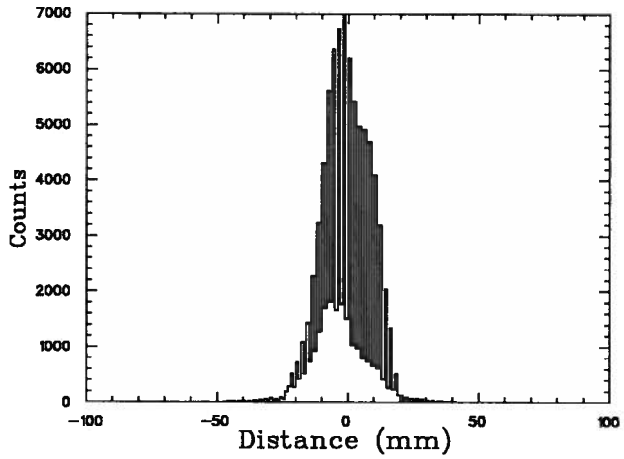

Figure 3.11: A typical target projection histogram in the x-y plane is shown.

Clearly there are two possible solutions; the correct one may be chosen knowing the beam polarity and the direction of the spectrometer magnetic field. Let ϵ denote the product of the field and the beam polarity. Rotating the solutions so that the angle of the hit in WC2 is zero (in the CHAOS coordinate system) results in one of the solutions having a positive center y coordinate and the other a negative one. In the case of the incoming beam, the correct solution is the one whose rotated center y coordinate has the same sign as ϵ [4]. The beam projection onto the target is defined as the intersection of this circle and a line of a given slope (usually chosen to be perpendicular to the incoming beam) through the origin, where the center of the target is situated.

The target projection is of crucial importance. In an analysing power measurement, the beam spot on the target must not change between the two target polarizations since it can introduce fictitious asymmetries. A typical target projection spectrum is shown in figure 3.11. In this graph the distance from the intersection point to the center of CHAOS is plotted, which corresponds to the horizontal profile of the incident beam on

[4]This is opposite for the outgoing beam.

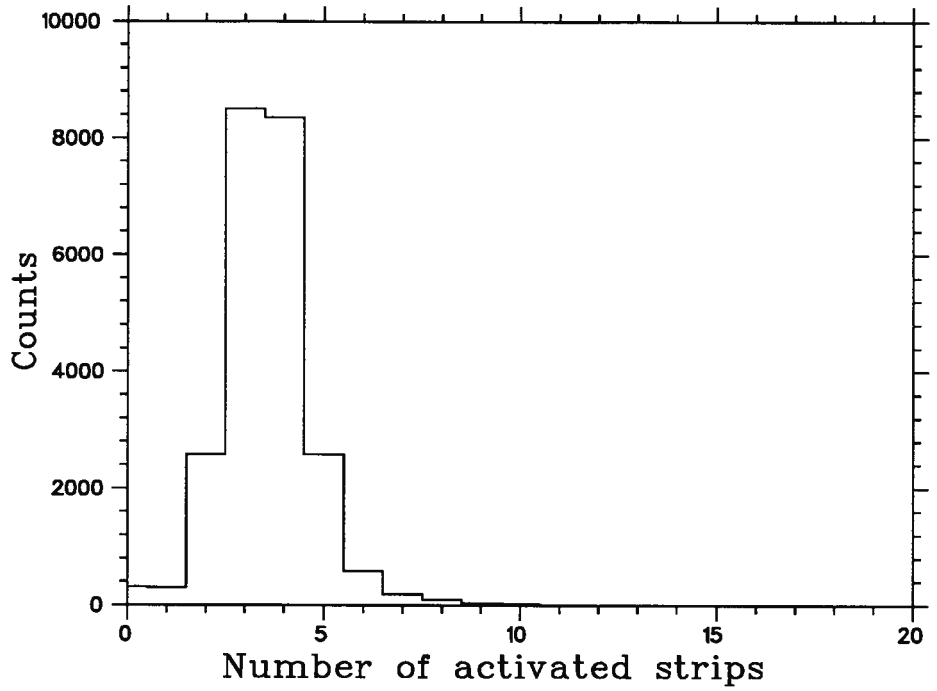

Figure 3.12: The number of activated cathode strips in WC2 for straight through beam is shown.

a planar target oriented perpendicular to the beam.

The vertical position of the hit is found by calculating the intersection of the charge centroid of the cathode strips with the activated anode wire. Consider a track in which n strips are associated with a given hit. The charge centroid is given by

$$\bar{N} = \frac{\sum_{i=1}^{n} q_i N_i}{\sum_{i=1}^{n} q_i} \tag{3.42}$$

Here, q_i and N_i are the ADC value and the strip number for the ith strip respectively; $\bar{N}$ represents the strip number corresponding to the charge centroid. Figure 3.12 shows a histogram of the number of activated strips per event in WC2 for straight through beam.

The vertical position of the track is obtained from the following equation:

$$z = \frac{\mid \theta(\bar{N}) - \theta_{hit} \mid R_c \pi}{180 \tan(30^\circ)} \tag{3.43}$$

Where $\theta(\bar{N})$ is defined as the horizontal angle strip $\bar{N}$ has at z=0, and θ_{hit} is the angle of the associated PCOS hit from the anodes. All angles are in degrees. In addition, R_c is the chamber radius. The vertical coordinate of the incoming beam track is used to obtain the vertical projection of the beam onto the target. This is calculated by performing a straight line fit on the z-coordinate versus the distance in the x-y plane of the hit from the line defined for the horizontal target projection. The intercept obtained from the fit is the vertical coordinate of the projection of the beam on the target. Figure 3.13 shows typical spectra for high ($\approx$ 1.8 MHz) and low ($\leq$ 50 kHz) beam rates. This graph seems to indicate that the beam profile changes with the rate; however, this is not the case. The broadening of the profile is due to the width of the ADC gate. Because of long drift times in WC4, the ADC gate width had to be set to 500 ns. At high beam rates, this allows for more than one incident pion to fall within the same ADC gate. As a result, the ADC value obtained from the WC1 and WC2 cathode strips corresponds to more than one incoming beam particle. This is not a problem for the other chambers since they are deadened at the entrance and exit of the beam. The wide gate causes an increase in the width of the spectrum, but the problem can be solved by providing a separate, shorter ADC gate for the WC1 and WC2 cathode strips.

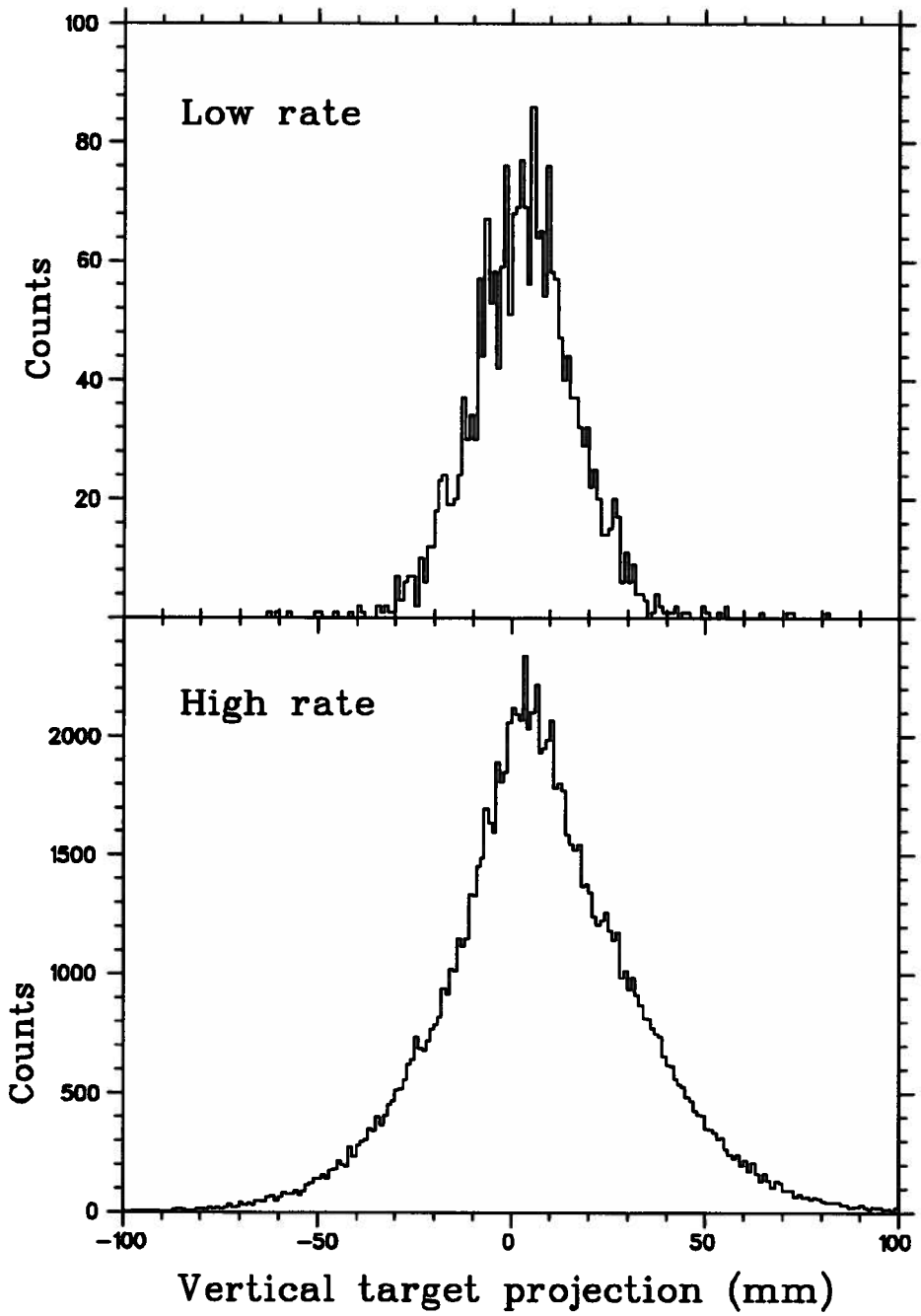

Figure 3.13: Vertical target projections for beam rates of $\leq$ 50 kHz and $\approx$ 1.8 MHz are shown.

Chapter 4

Wire Chamber 3

As stated previously, design considerations for CHAOS require the existence of a third tracking detector. This led to the design and construction of the inner CHAOS drift chamber, WC3, which is required to operate in a region of high magnetic field (ie: $B \geq 1$ T). Basic operating principles of drift chambers are discussed in the first section of this chapter. A brief description of the chamber and performance results are presented in the remaining.

4.1 Basic Operating Principles

The operation of drift chambers is similar to that of multiwire proportional chambers, described earlier. In this case, however, the drift time of the electrons from the ionization region to the anode wire is used to obtain position information. Electrons produced from the ionization drift towards the anode wire with an inverse velocity of approximately 20 ns/mm, where avalanche multiplication occurs. If the electrons are liberated by the charged particle at a time t_0, and a signal from the wire is received at a later time, t, the spatial coordinate of the track with respect to the wire is given by the following:

$$x = \int_{t_0}^{t} v dt \tag{4.44}$$

where v is the velocity of the electrons in the drift space. Clearly the most convenient case is that of a constant v, in which case, the space-time relation would be given by

$$x = (t - t_0)v \tag{4.45}$$

In the absence of a magnetic field, the linearity of the space-time relation depends mainly on the electric field uniformity in the drift region. In practice the time t_0 is determined by placing a scintillation counter in front of the chamber.

Multiwire drift chambers can not be constructed in the same way as proportional counters. In particular, adjacent anode wires are usually not used. This is because the space-time relation becomes nonlinear in the low electric field region between the two anodes. The problem is overcome by placing thick field shaping cathode wires between successive anodes.

Drift chambers are less expensive to build and instrument than multiwire proportional chambers; furthermore, they provide more accurate spatial information. However, some disadvantages exist. The spacing between the sense wires in a drift chamber is much larger than that of a MWPC. Typical drift times are on the order of hundreds of nanoseconds; hence a drift chamber is not capable of operating at high rates. In a drift chamber, the coordinate information is obtained solely from the drift time and the anode wire location. As such, a particle passing at the same distance on either side of an anode will result in identical drift times, making the location of the track ambiguous (see figure 4.14). This is referred to as the left-right ambiguity problem and can be resolved in various ways depending on the chamber geometry and environment.

4.2 Description of WC3

WC3 is a single plane cylindrical drift chamber located at a radius of 343.77 mm. It has a rectangular cell geometry consisting of alternating anodes and cathodes separated by 7.5 mm. The chamber also uses alternating high voltage and signal cathode strips

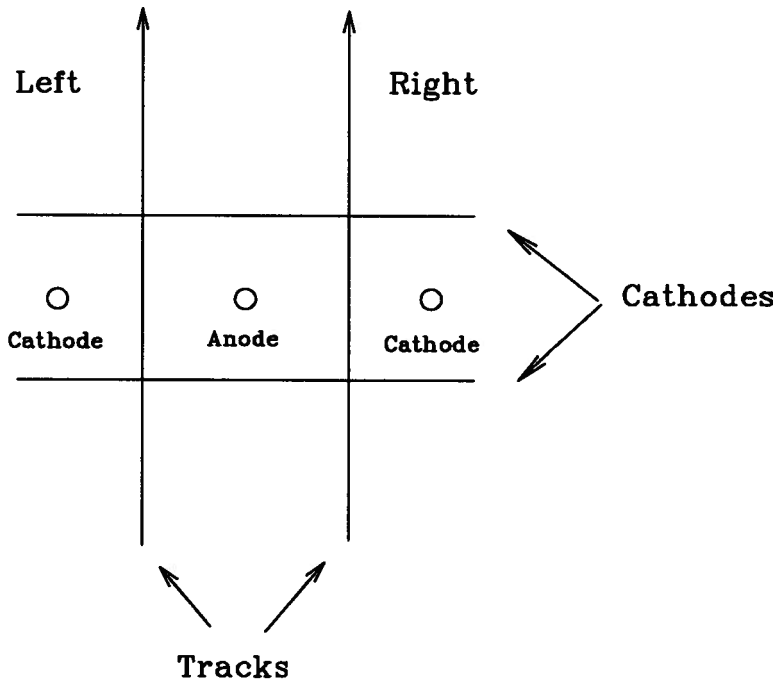

Figure 4.14: Figure showing the left-right ambiguity in a drift chamber. Drift times to the central anode are identical for both tracks.

to achieve a more uniform electric field and resolve the left right ambiguity problem (see figure 4.15). WC3 contains a total of 144 anodes (angular pitch of 2.5°) and 576 cathode signal strips. The half gap of the chamber is 3.75 mm and the vertical active area is 90 mm. The design of WC3 is otherwise similar to that of WC1 and WC2. Two concentric cylinders of 1 mm thick rohacell placed in G10 rings support the wire tension. The anode and cathode wires are strung at tensions of 80 and 120 grams, respectively; they are mounted using crimp pins on the G10 ring which forms the frame of the inner cylinder. Both the inner and the outer rohacell frames are sandwiched between layers of 12 μm kapton and 25 μm ECN foil. For each of the cylinders, the latter forms the

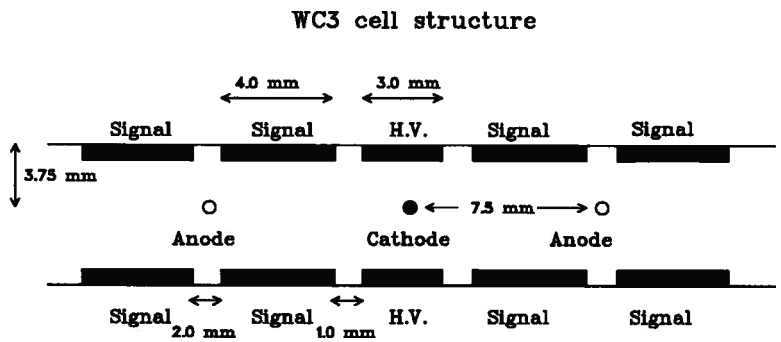

Figure 4.15: Figure showing the WC3 cell structure. Thickness of the strips and wires has been exaggerated in this figure for clarity.

cathode strips, and the former prevents gas leakage through the rohacell. In addition, two layers of 25 μm double sided aluminized mylar form the flushing gas windows. The cathode strip pattern was photo-chemically etched on 25 μm nickel plated kapton. The anode and the cathode wires are 50 μm and 100 μm gold plated tungsten, respectively.

Both the anodes and the readout strips are instrumented with 8-channel preamplifiers. As in the case of WC1 and WC2, the cathodes are also equipped with inverter-postamplifier electronics and the anodes with LeCroy 2735DC amplifier/discriminator cards. The anode signal is split and fed to the LeCroy 4290 drift chamber chamber system as well as PCOS III, which is needed in order to provide the second level trigger with the necessary information. Only the anode wire number and not the drift time information is used to form the second level trigger decision. The sections of the chamber located at the entrance and exit of the beam are deadened in groups of four adjacent cells by simply removing the anode bias to that group. This prevents damage caused by the large incident flux. In the absence of a magnetic field, the drift electron trajectories would be straight. Consequently, one would be able to employ a variety of techniques to

resolve the left-right ambiguity problem, for example, using groups of two anodes separated by a small distance. However, since operation in a high field region is required, this approach is not practical [16]. Because the drift electron trajectories curve in the presence of the field, the avalanche can occur in front of or behind the anode doublet. In such cases, left and right tracks are not resolved. This led the CHAOS group to develop a new method of resolving the left-right ambiguity [16]. It uses two pairs of readout strips on opposite sides of the anode to distinguish left from right. Figure 4.16 shows the drift electron trajectories as calculated by Garfield.[1] In this figure the difference in the pulse heights between the solid strips in a given cell is used to resolve the left-right ambiguity. In each case the upper right strip has a larger induced pulse height than the lower left one. Figure 4.17(a) shows the normalized difference between diagonally opposed strips numbered 2 and 3 as shown in figure 4.16. The normalized difference between any two strips, a and b, is defined as

$$\frac{P_a - P_b}{P_a + P_b} \tag{4.46}$$

where P_a and P_b are the ADC values for strips a and b, respectively. Note that centroids of the two peaks are not symmetric about zero. This is due to an offset resulting from different preamplifier, inverter and cathode strip gains, the latter of which is caused by imperfections in the positioning of the strips in the chamber. Graph 4.17(b) shows this difference as a function of the drift time.

Tracks passing to the left and to the right of the wire are well resolved. Since the TDC's were operated in common stop mode, increasing drift time is to the left in figure 4.17(b).

[1]Garfield is a drift chamber simulation program [15]. It calculates various quantities such as electric field and the drift electron trajectories for a given cell geometry. Figure from reference[16].

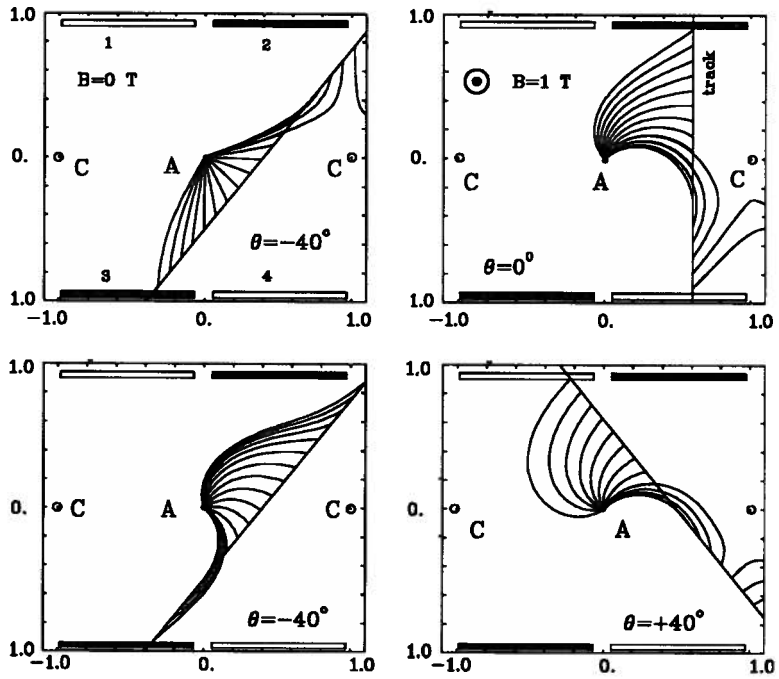

Figure 4.16: Drift electron trajectories for tracks with various angles of incidence, θ, are shown. The solid strips correspond to those used to resolve the left-right ambiguity. All dimensions shown are in cm. All cases are for B=1 T except the upper left figure which is at B=0. A and C denote the anode and cathode wires respectively. The axes represent the cell dimensions used in the simulation. For magnetic fields opposite in polarity to that shown, the unshaded strips provide the best left-right resolution.

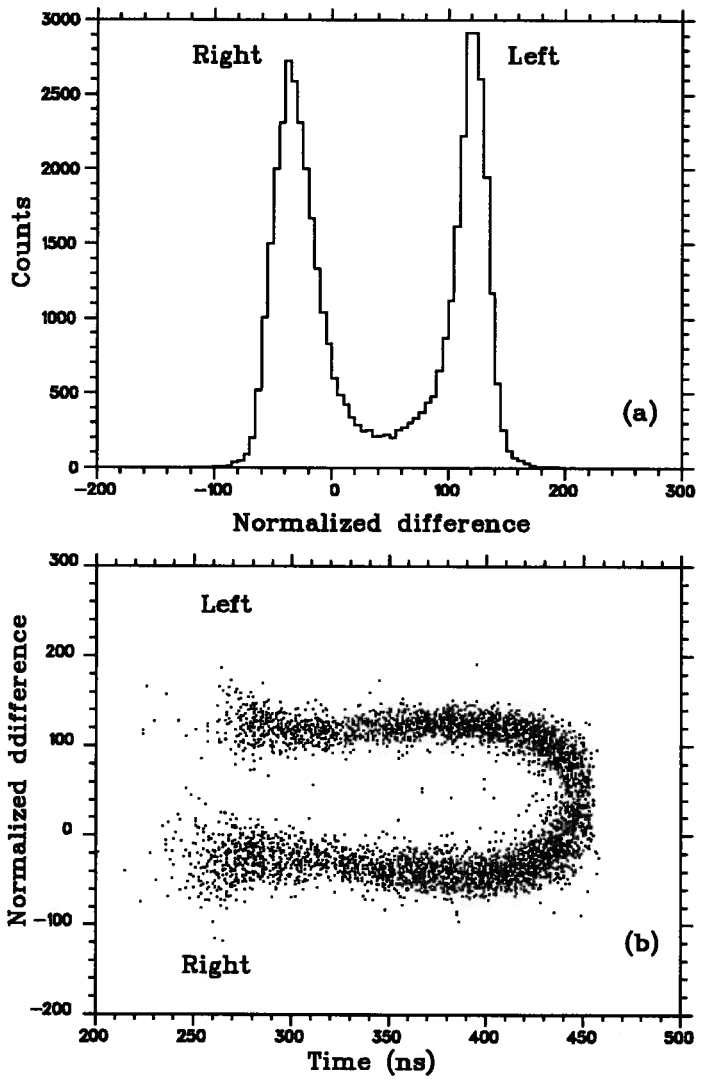

Figure 4.17: Figure showing the normalized difference between diagonally opposed strips (a). The difference as a function of the drift time is also presented (b). The normalized difference scale has been expanded by a factor of 500. Long drift times correspond to small TDC values. The data were acquired at a magnetic field setting of 1.2 T

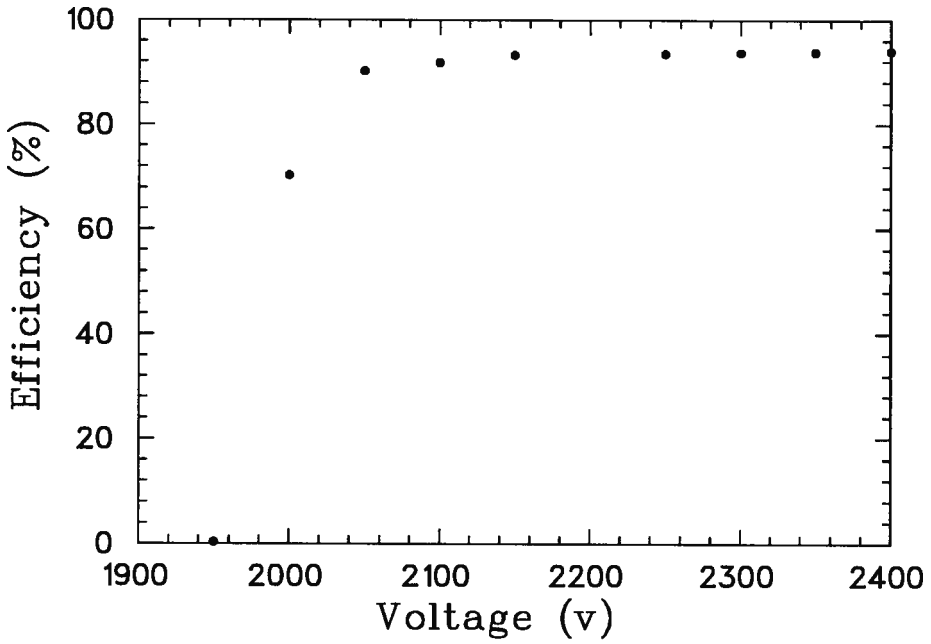

Figure 4.18: Plateau curve for the WC3 anode bias is shown.

4.3 Performance

The operating voltage for the chamber was determined by means of a plateau curve as shown in figure 4.18. This was obtained at a rate of $\leq$ 50 kHz. The operating voltages chosen for WC3 are an anode bias of 2250, a cathode strip bias of -600, and cathode wire bias of -300 volts. Chamber efficiency was computed using the same method as for WC1 and WC2. Typical drift time spectra for zero and nonzero magnetic field are shown in figure 4.19. The gas used in the chamber is a 50-50 mixture of argon and ethane; a small amount of ethanol bubbled into the gas at 0°C is used as a cleaning agent.

In the case of a uniformly distributed beam, a rough idea of the linearity of the space-time relation can be obtained from the shape of the drift time spectra. The vertical axes in drift time spectra represent the number of counts, N, in a time bin Δt ; hence the

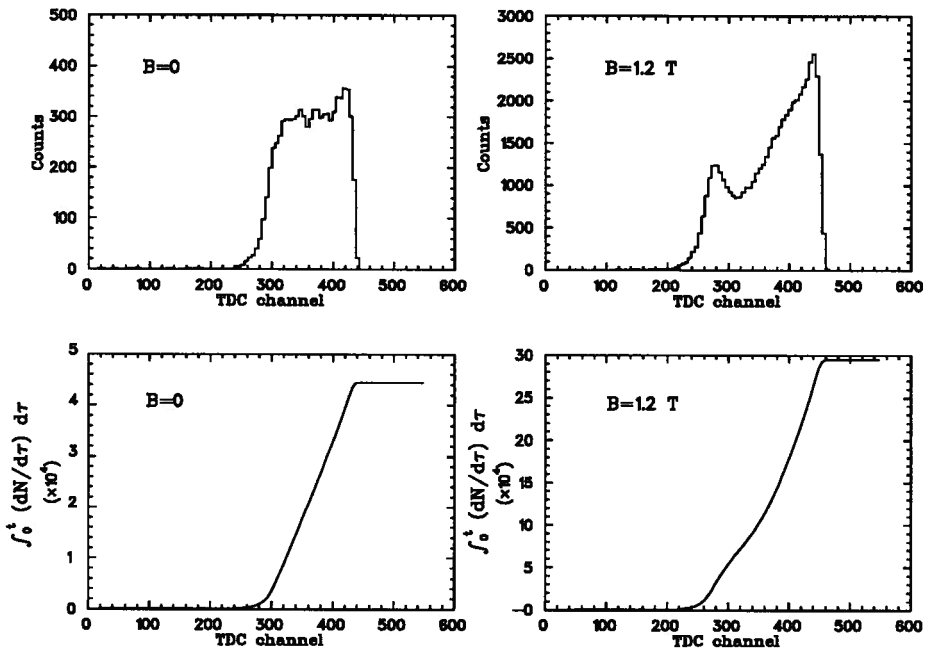

Figure 4.19: WC3 drift time spectra along with their integrals (proportional to the drift distance) for zero and nonzero field settings are shown. Increasing drift time corresponds to smaller TDC channel number (1 ns/channel).

counts represent $\frac{dN}{dt}$. Furthermore,

$$\frac{dN}{dt} = \frac{dN}{ds}\frac{ds}{dt} \tag{4.47}$$

where s and t are the drift distance and time respectively. Given a uniform beam distribution, $\frac{dN}{ds}$, a constant $\frac{dN}{dt}$ results in a linear time-distance relation.[2] For zero magnetic

[2]The time-distance relation determines the distance from the ionization point to the wire as a function of the drift time.

field setting, the drift spectrum is fairly flat, but this is not the case for nonzero magnetic field. This is because the drift electron trajectories curve in the field making the space-time relation nonlinear. Figure 4.19 shows the integral of the time spectrum for zero magnetic field; the linearity of the time-distance relation is evident. The integral of the spectrum for nonzero field suggests a nonlinear time-distance relation. In order to obtain the coordinate of the track, the angle of incidence of the track with respect to the chamber midplane is needed. The process of obtaining the time-distance relation, the incident beam angle, and the coordinate of the hit in the CHAOS coordinate system is discussed in section 7.1. WC3 resolution is discussed in chapter 7.

Chapter 5

Wire Chamber 4

The fourth and the outer most CHAOS chamber is a vector drift chamber, WC4, which is capable of providing both horizontal and vertical coordinate information. The design and construction of this chamber along with performance data are discussed in this chapter.

5.1 Description & Construction

WC4 contains fourteen concentric cylindrical planes of wires separated radially by 0.5 mm. Eight of the planes are anodes that provide horizontal spatial information, and two planes are resistive anode wires that are used to obtain vertical position data. The four remaining anode wire planes are field shaping ("guard") wires. The chamber consists of one hundred cells, each spanning an angular arc of 3.6°. Figure 5.20 shows the cell geometry. The first (innermost) resistive wire is located at a radius of 617.5 mm, and the radius of the first anode plane is 627.5 mm. To resolve the left-right ambiguity, the anodes in a given cell are alternately staggered by ± 0.25 mm in the direction perpendicular to the radial line bisecting the cell. A major concern in the design of this chamber was mechanical support. Several options were considered, one of which proposed the use of a "chamber box " that would provide support for WC4 as well as the three inner chambers. For repair purposes, this structure had to be breakable in the region between WC2 and WC3. However, it was realized that repairs would still be too difficult to perform, and the design was abandoned.

On each side of the cell there are nine cathode strips kept at a negative potential; these

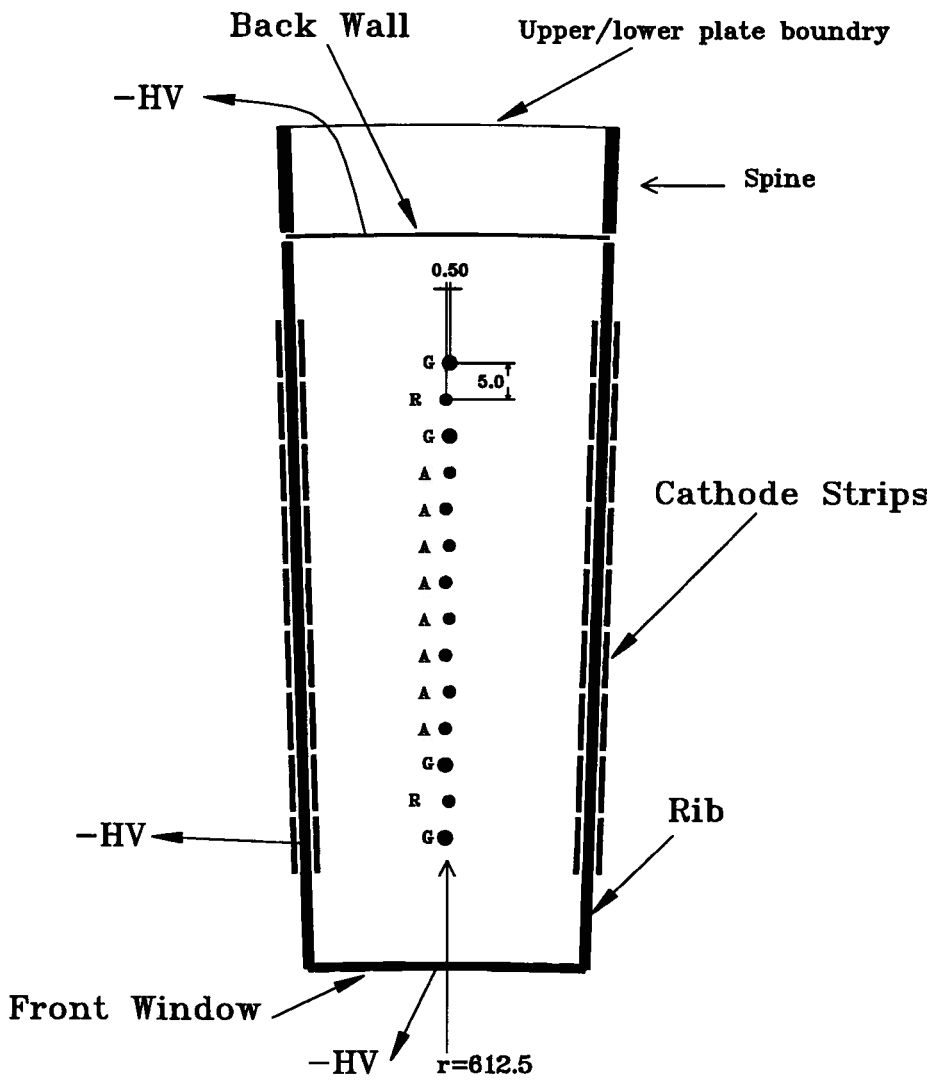

Figure 5.20: Diagram showing a single cell of WC4. The letters A, G, and R denote anode, guard and resistive wires, respectively. All dimension are in mm.

strips form the cell boundaries. Two cathode planes common to all cells and also kept at a negative potential form the front and the back walls of the cell. Due to its large radius, the chamber was constructed in eight separate sections. Four of the sections are each 36° wide, and the other four each span 54°. The wires are strung and crimped at both ends to plates of Ultem, a rigid insulating material. The wire tension is supported by rohacell-G10 ribs, which also provide the cell boundaries as well as the surfaces on which the cathode strips are glued. The ribs are constructed by placing 2 mm thick rohacell which was compressed to 1.6 mm in a C shaped G10 frame in which the open part of the C faces the front of the chamber. The cathode strip pattern is photochemically etched on 25 μm nickel plated kapton and glued on both sides of the rohacell. The shape of each cell is a trapezoid; hence, to obtain a uniform electric field, the voltage on the cathode strips at the narrow end of the cell must be less than that at the wide end. This was accomplished by means of a chain of 3.02 $M\Omega$ resistors which dropped the voltage by 55 V across successive strips, and then was grounded through a larger resistance.

The resistor chain circuit pattern is etched on the G10 frame, and gold plated spring clips are used to provide electrical contact between the high voltage circuit and the cathode strips. Various methods of achieving reliable electrical contact were studied. These included the use of conducting epoxy and low temperature solder paste. Neither of these two methods provided reliable contact. Conventional soldering was not an option, since high temperatures evaporated the metal from the kapton foil. The spring clips proved to be the best option since one end could be soldered onto the G10 frame, while the other end provided contact to the fragile surface through spring tension.

The inner (front) window of the chamber, which also forms one of the cell cathode planes, is constructed from 1 mm thick rohacell sandwiched between 25 μm kapton and 25 μm aluminized mylar. The outer window (back wall) of the chamber provides the other cell cathode plane and is constructed from 250 μm thick G10 with one copper-coated

side. The copper was nickel plated to protect against corrosion.

Both the anode and resistive wires are connected to 8-channel preamplifier cards. The anode signals are read into a 4290 TDC system and both ends of the resistive wires are instrumented with FASTBUS ADC's. As for WC3, cells located at the entrance or exit of the beam were deadened in groups of 2 ribs (3 cells) by removing the rib bias voltage via a high voltage distribution panel located on top of the spectrometer.

Extreme care was taken in the construction process. The rohacell ribs which form the frame of the chamber are quite fragile and had to be handled with care. Each of the eight sections was constructed by gluing the rohacell-G10 ribs into grooves that were machined into the top Ultem plate. The bottom plate was then glued to the other end of the ribs, which protruded through slots in the bottom plate so that the resistor chain and the high voltage connections were external. In each section, the end cells require a specially made rib. The cathode strips on the end ribs appear on one side only, and the thickness of these ribs is half that of others. The back cathode plane was also glued onto both the top and bottom plates. Thin G10 spines (1.6 mm) were glued on the outer side of the back plane behind each rib to provide extra mechanical support. The chamber was then strung and the front window was fastened to the Ultem plates by means of screws. The edges of the window were taped to the end ribs with the use of kapton tape. A thin rubber gasket placed between the window and the plates proved to be helpful in making the chamber gas tight; however, a layer of electronic grade silicon RTV was also required on the outer seams of the window. The anode and resistive wires are $20\mu m$ gold plated tungsten and 20 μm Stablohm800, respectively [17]. The guard wires are made of either 150 μm or 75 μm gold plated tungsten. The anode and resistive wire tensions are 50 and 10 grams respectively.

5.2 Charge Division

The method of charge division has been successfully used to obtain vertical coordinate information in drift chambers [18], [19]. The nominal resolution is 1% of the length of the wire. A brief description of the method is as follows. An amount of charge, Q, is injected at a distance D from the center of a wire of length L and resistance R (see figure 5.21).

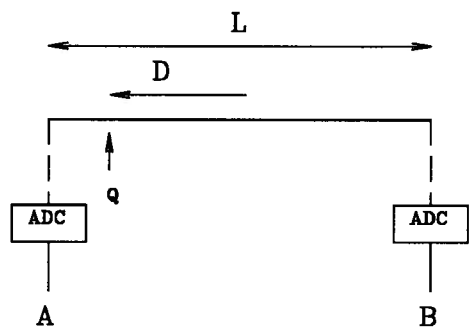

Figure 5.21: Figure illustrating the charge division method.

If the collected charge at the two ends of the wire is given by A and B, the distance D is given by

$$D = \frac{(A-B)L}{2(A+B)} \tag{5.48}$$

The above is just a naive application of Ohm's law and is valid if the integration time is much greater than the time constant of the wire [20]. This principle was used to obtain the vertical coordinate of the track in WC4. The choice of wire resistance is crucial in the charge division method. The resistance must be large enough such that thermal noise is kept low. However, if the wire is also used to obtain drift information, the time constant of the wire must be small. The smallest time constant is obtained when the

wire resistance is equal to the characteristic impedance of the wire, given by

$$R = \sqrt{\frac{L}{C}} \tag{5.49}$$

where L and C are the inductance and the capacitance per unit length of the wire. In WC4, the resistive wires were not used to obtain drift time information. Furthermore, the integration times are on the order of 500 ns. This is much greater than the time scale of charge division, which is a function of the length of the wire (order of a few ns). As a result, only noise considerations dictated the nominal wire resistance.

The preamplifiers used must have an input impedance which is much less than the resistance of the wire. The wires used in WC4 are $\approx$ 25 cm long and have a resistance of $\approx$ 1 KΩ. The input impedance of the preamplifier is $\approx$ 75 Ω. Various wire materials were examined in a prototype chamber, and Stablohm800 provided the best resolution and linearity.

5.3 Performance

The gas used in this chamber is a 50-50 mixture of argon and ethane; a small amount of ethanol bubbled into the gas at 0°C is used as a cleaning agent. Figure 5.22 shows the plateau curve for the chamber. Since this chamber has several wire planes, the efficiency of a single wire is calculated using the following method. Consider three wires in a single cell labelled 1, 2 and 3, where wire 2 is located between 1 and 3. The efficiency of 2 is given by

$$E_2 = \frac{1 \cdot 2 \cdot 3}{1 \cdot 3} \tag{5.50}$$

where $1 \cdot 2 \cdot 3$ represents the number of times all three wires fired and $1 \cdot 3$ is the number of times both 1 and 3 were activated. The efficiency of the anode wires was found to be independent of the front/back plane voltage. However, the resistive wires were sensitive

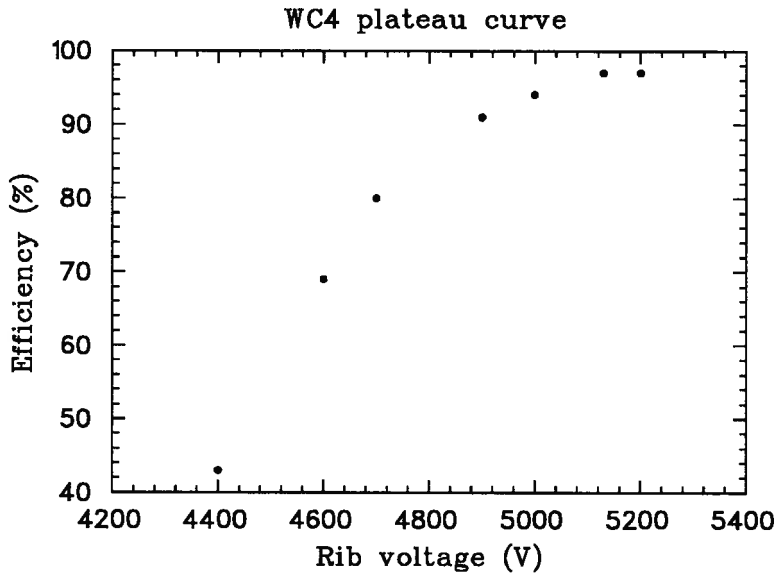

Figure 5.22: WC4 plateau curve is shown.

to this voltage. As a result the back plane setting was chosen to provide maximum resistive wire efficiency without causing the preamplifiers to saturate. The cathode strip (rib) and front/back plane operating voltages are −5200 V and −2300 V respectively.

Figure 5.23 shows typical drift time spectra and their integrals for zero and 0.5 T central field settings. The field at WC4 is approximately 20% of the central value. The total width of the spectrum is 400 ns. This corresponds to the average width of the cell which is 20 mm; hence a rough estimate of the time distance-relation is 0.05 $\frac{mm}{ns}$. The integrals of the drift spectra show the linearity of the time-distance relation for zero and nonzero field settings. This is because the chamber is located in a low magnetic field region.

The left-right ambiguity problem is resolved using anode wire staggering. Figure 5.24 shows the wire planes in a cell along with two sample tracks. The track passing on the left side has shorter drift times to the even numbered wires than to the odd numbered

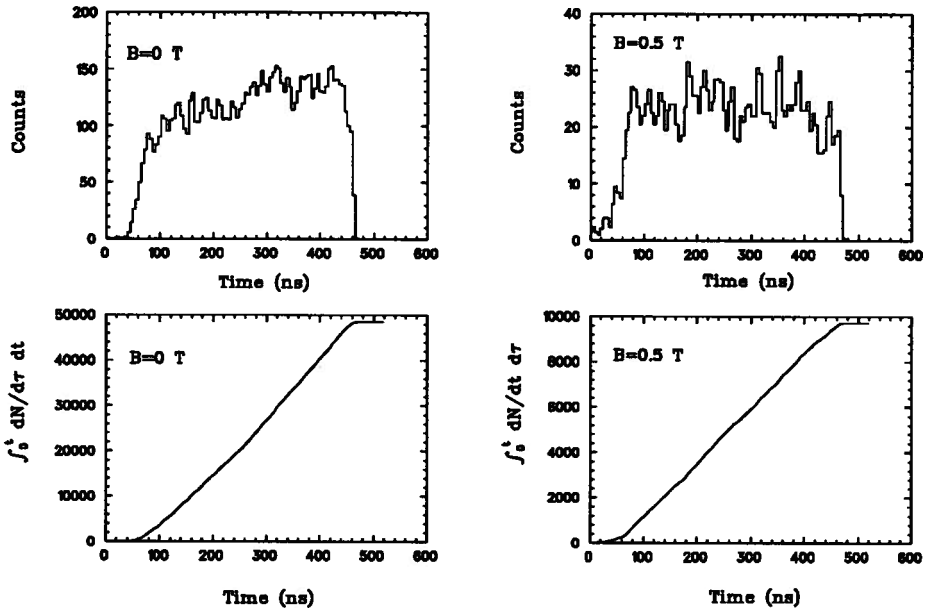

Figure 5.23: Graphs showing drift time spectra and their integrals for zero and 0.5 T. Once again, long drift times correspond to small TDC values.

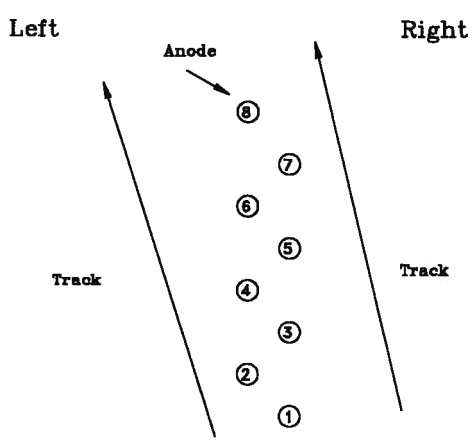

Figure 5.24: Illustration showing left and right tracks in a single cell of WC4.

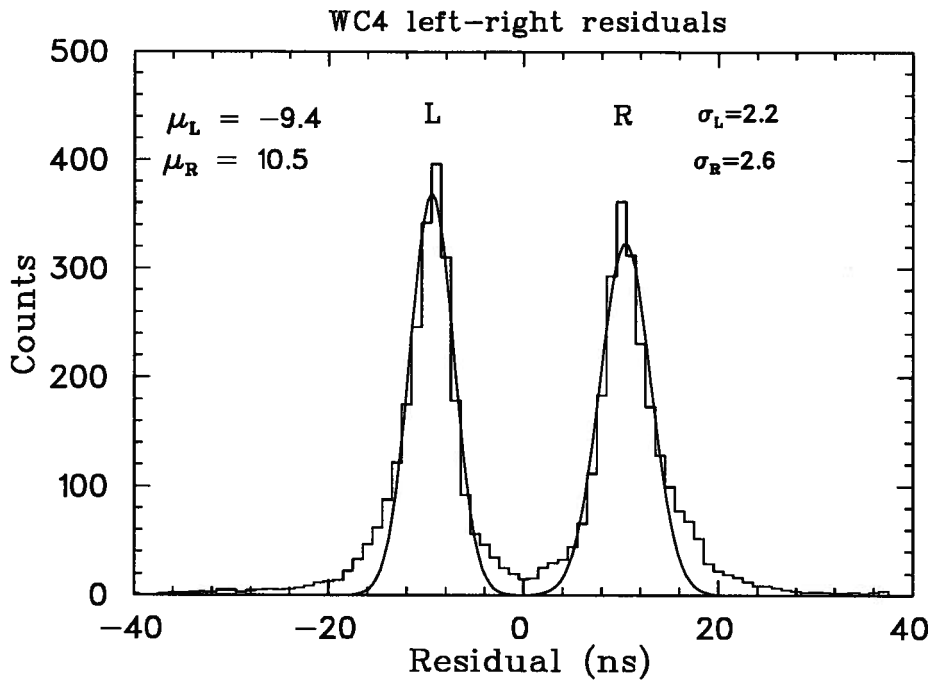

Figure 5.25: WC4 Left-right residual for a single wire along with the time centroids (μ) of each peak are shown. The solid curve is a gaussian fit to the data.

ones. The situation is reversed for the track on the right. The difference in the drift times between the odd and even wires is used to distinguish left from right.

The left-right residual for a given wire is defined by the following relation:

$$R_i = \frac{t_{i+1} + t_{i-1}}{2} - t_i \quad 2 \leq i \leq 7 \tag{5.51}$$

The sign of the residual depends on whether the track passed on the right or left side of the wire. Figure 5.25 shows a typical residual histogram; left and right tracks are well separated. Furthermore, the time separation between the centroids of the two peaks corresponds to a distance of 1.0 mm[1]. The time separation between the two peaks is ≈

[1]This is just twice the staggering

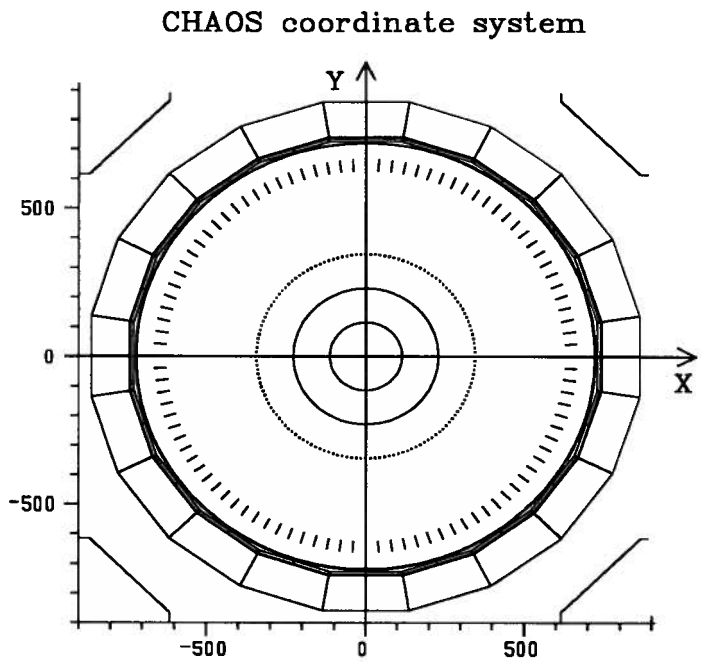

Figure 5.26: The CHAOS coordinate system is shown. The positive z-axis points out of the page, and the location of each of the anodes in each chamber is also shown.

20 ns. This confirms the 0.05 $\frac{mm}{ns}$ estimate for the time-distance relation obtained from the raw drift time spectrum.

The CHAOS coordinate system is shown in figure 5.26. The polar angle is measured counter clockwise with respect to the positive x-axis. The coordinate of each WC4 anode in the CHAOS coordinate system is given by the following equations:

$$x_w = R_w \cos(\alpha) \pm d_s \sin(180 - \alpha) \tag{5.52}$$

$$y_w = R_w \sin(\alpha) \pm d_s \cos(180 - \alpha) \tag{5.53}$$

where α is the polar angle of the center line of the cell, d_s is the perpendicular distance

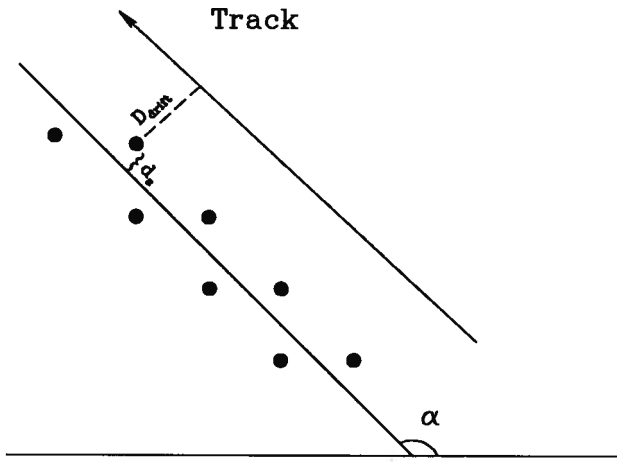

Figure 5.27: A sample track in WC4 is shown.

between the wire and the center line (250 μm), and R_w is the radius of the wire plane (see figure 5.27). The sign of the second term in the above set of equations depends on the wire staggering. The x-y coordinates of a track are given by

$$x_{track} = x_w \pm D_{drift} \sin(180 - \alpha) \tag{5.54}$$

$$y_{track} = y_w \pm D_{drift} \cos(180 - \alpha) \tag{5.55}$$

where D_{drift} is the drift distance. The sign of the second term depends on whether the track passed on the left or the right side of the sense wire. The above equation is valid if one assumes that the drift lines are perpendicular to the row of anodes. This is a good assumption, except very close to the wire where the field becomes nonuniform. Thus, to obtain better resolution the angle of incidence of the track and the actual shape of the drift lines must be considered.

The vertical coordinate is obtained using the method of charge division. Figure 5.28 shows a typical resistive wire ADC spectrum. Assuming that the preamp gains are the

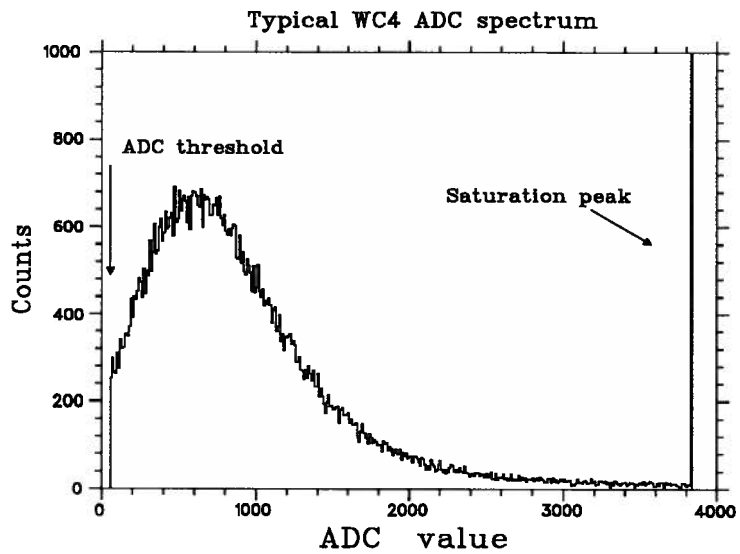

Figure 5.28: Typical ADC spectrum from one end of a resistive wire is shown.

same for both ends of the wire, the vertical coordinate of the hit is given by

$$z = \frac{t-b}{2(t+b)}l + z_0 \tag{5.56}$$

where t is the ADC value for the top of the wire, b is the ADC value for the bottom of the wire, l is its electrical length, and z_0 is an offset. The constants in the above equation were obtained from calibration data and are discussed in chapter 7.

5.4 Induced Pulse Problem

When a negative pulse is produced in a given anode wire, at the same time a positive pulse is induced on the neighbouring anodes, resulting in a distortion of their signals. This effect is illustrated in figure 5.29.

The induced signal substantially degrades the chamber resolution; it delays the direct

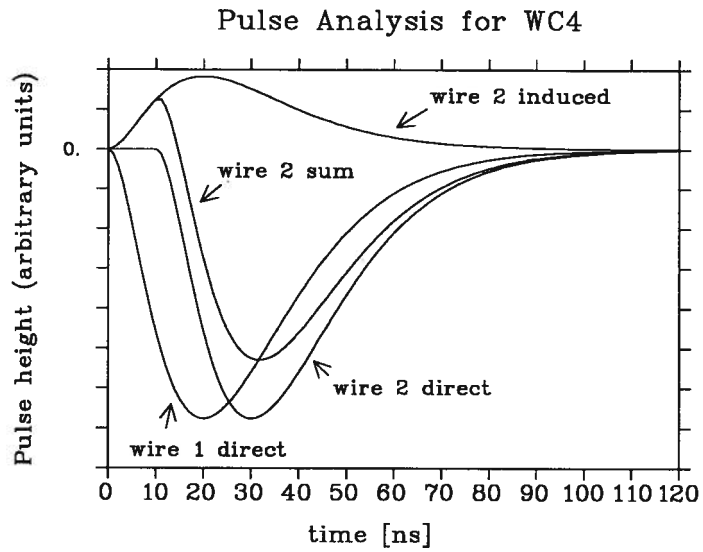

Figure 5.29: Illustration of the induced pulse effect. Pulse heights and widths are just estimates and do not represent actual values.

signal and causes the measured drift time to be shorter than the physical one (see figure 5.29). A series of tests were performed in which the tracks which passed only on the left half of the cell were recorded. This was achieved by requiring a signal from a thin (1 mm wide) scintillating fiber mounted vertically and positioned in front of the chamber. In this case the drift time to the even wires is longer than to the odd wires (see figure 5.24). As a result, the pulse induced by the odd wires on their even neighbours will be present before the drift electrons arrive at the anode. This does not cause any distortion in the even wire signals; however, the induced pulse from the even wires will distort the signal from the odd wires. In such a case, the resolution of the odd wires is much worse than the even ones as shown in figure 5.30.

The resistive wires are less susceptible to the induced pulse problem because a guard wire is located between each resistive wire and its closest anode.

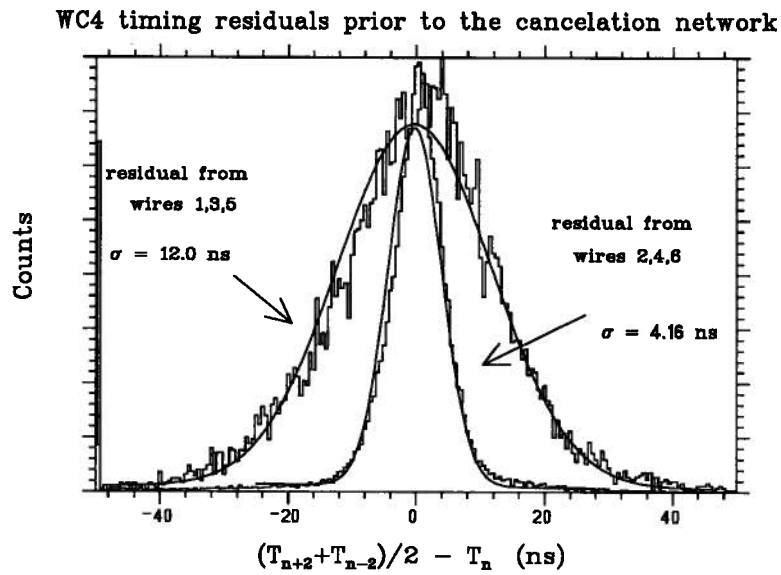

Figure 5.30: WC4 residuals prior to the implementation of the cancelation network are shown for events passing on the left of a cell.

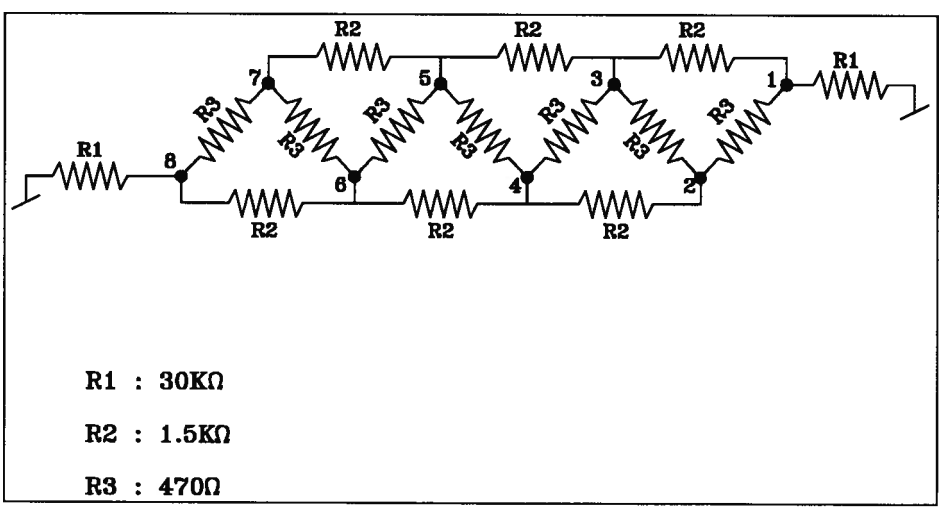

Figure 5.31: Schematic diagram of the cancelation network is shown.

A resistor network shown in figure 5.31 is used to minimize this problem. The basic idea is to take a fraction of the signal from each anode and distribute it to its nearest neighbours. This negative signal will help compensate for the positive induced pulse. The values of the resistors in the cancellation network were varied while observing the induced pulse height on an oscilloscope, using a γ source so that only one wire fired at a time. The values were chosen to minimize the induced pulse amplitude without distorting the original signal. Figure 5.32 shows the residuals calculated after the implementation of the cancellation network. In this case again only tracks passing on the left were chosen. It is clear that the odd wire residuals have improved dramatically. The induced pulse problem could have been entirely avoided if thick wires kept at ground were placed between successive anode planes. These wires would not cause an avalanche and would absorb the induced pulse.

The difference in the widths of the peaks shown in figures 5.32 and 5.25 is due to the following. In the former, only tracks passing on one half of the cell, roughly parallel to the row of anodes were considered; hence, the drift time to all of the even wires is identical, and the same is true for the odd wires. Consequently the induced pulse problem is enhanced. In figure 5.25, tracks having different angles with respect to the row of anodes were analysed, causing the induced pulse problem to be less pronounced. The intrinsic resolution of a given wire is 135 μm, which is obtained by dividing the average of the standard deviations of the peaks in figure 5.32 by $\sqrt{3}$.[2]

[2]The factor of $\sqrt{3}$ is needed since 3 wires are used to calculated the histogrammed quantities in 5.25. The estimate of 0.05 mm/ns was used.

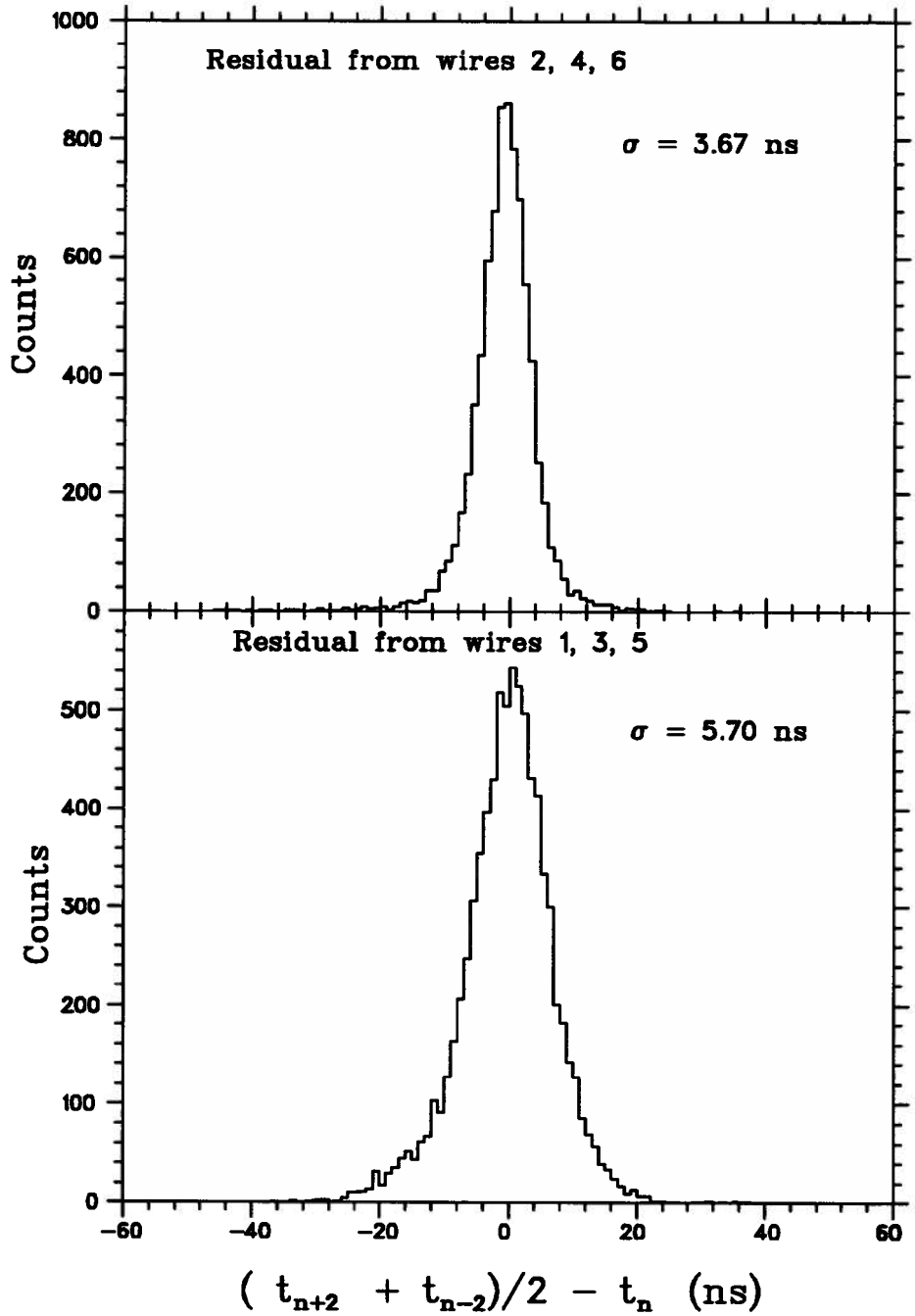

Figure 5.32: Spectra of WC4 residuals after installation of the cancelation network. Again, only tracks passing on the left of the cell were considered.

Chapter 6

CFT Counters, Trigger Systems and Readout Electronics

6.1 CFT Counters

The outer most layer of detectors in the spectrometer are the CHAOS Fast Trigger (CFT) counters. Each of these counter telescopes consists of three layers. The first layer (ΔE_1) is a plastic scintillator 3.5 mm thick with an area of 25×25 cm^2, and the second layer (ΔE_2) is made up of two adjacent plastic scintillators, each of which is 13 mm thick with a cross sectional area of 13×25 cm^2. The third layer (C) consists of 3 adjacent lead glass Cerenkov counters each 12 cm thick with an area of 9.5×25 cm^2. There are 20 such counters (blocks) each of which covers 18°. The information from these blocks is used to make the fast (first level) trigger decision based on event multiplicity; hence the name CHAOS Fast Trigger counters. Furthermore, the particle identification data obtained are crucial in the analysis stage. Both ΔE_1 and ΔE_2 are equipped with TDC's and ADC's, and the Cerenkov counters are instrumented with ADC's. Blocks positioned at the entrance and exit of the beam are removed.

The CFT counters are required to identify pions, protons, and electrons over the range of momenta encountered in CHAOS experiments. Particle identification is based on pulse heights, which are proportional to the energy deposited by different particles in each layer. The energy lost by a heavy (with a mass much greater than that of the electron) charged particle in a thin counter of thickness Δx is given by the Bethe-Block

relation. In natural units, this is written as

$$\Delta E = \frac{4\pi N z^2 e^4 Z\rho}{m\beta^2 A}\left\{\ln\left(\frac{2m\beta^2}{I(1-\beta^2)}\right) - \beta^2\right\}\Delta x \tag{6.57}$$

where β and z are the velocity and charge of the particle, m is the electron mass, N is Avagadro's number and Z, A and ρ are the atomic number, atomic mass and density of the counter material, respectively. In addition, I represents the medium's effective ionization potential. For a given material, the energy loss depends only on the velocity and charge of the particle. As a result, pions and electrons will deposit roughly the same amount of energy if the pion velocity is similar to that of the electron. This occurs when the pion kinetic energy is comparable to its mass. Consequently, ΔE_1 and ΔE_2 can distinguish pions from electrons over a limited range of lower pion momenta. The protons on the other hand are much heavier than both pions and the electrons; thus, ΔE_1 and ΔE_2 are capable of separating protons from pions and electrons over the entire momentum range encountered in CHAOS experiments. In practice, particle identification in CHAOS is accomplished by selecting the appropriate particle group in scatter plots of pulse height versus momentum.

The third layer (C) is used to separate pions from electrons at higher momenta. A charged particle traversing a medium at a speed higher than light in the medium emits Cerenkov radiation. The velocity of light in a material with index of refraction, n, is given by c/n, where c is the speed of light in vacuum. Electrons resulting from π^0 decay inside the spectrometer are highly relativistic and thus emit Cerenkov radiation in lead glass ($n \approx 1.7$). The pions on the other hand, will radiate only if their momentum is greater than 100 MeV/c. Furthermore, due to their small mass, electrons emit bremsstrahlung radiation in the presence of the electric field produced by the lead nuclei in the glass. The bremsstrahlung photons will then produce electron-positron pairs which contribute to the Cerenkov light produced by the initial electron. The above process produces a

shower of electrons that result in creation of a large number of Cerenkov photons. The pions on the other hand are more massive and do not lose energy in the presence of the field. As a result, the pulse height of the signals produced by electrons is much greater than those produced by pions.

The CFT counters were calibrated with pions, protons, and electrons over a wide range of energies. In order to apply the same cut to all of the pulse height spectra for each of the layers, it is important that all phototubes in a given layer have similar gains. Each of the tubes was tested and those with similar gains were installed in the same layer. Further adjustment of the gain was possible by changing the phototube high voltage. However, the gain of each tube must still be monitored in order to account for the fluctuations caused by factors such as changes in temperature. This can be done in several ways. One is to recalibrate the system with particles of known momenta at regular intervals during the course of an experiment. However, this option is not practical since it requires disruption of the experiment and loss of valuable time. The other is to supply all of the tubes with exactly the same amount of light for calibration, but it is difficult to ensure that the amount of light directed to each of the tubes is the same. Consequently, a new monitoring system was designed which operates in the following manner. A Xenon flasher system is used to produce flashes of light at precise time intervals. The light from the original spark is directed through a long helical acrylic cylinder. The helix is covered with reflective material, and a series of optical fibers are inserted over the circular region at the end opposite the spark. Although the light intensity is not uniform over this region, the ratio of the intensities between the various points is a constant that depends on the geometry of the cylinder. In other words, the relative distribution of light to the different fibers is constant and shows no memory of the spark. Hence, if one of the fibers is sent to a reference tube of constant gain and the remaining are each sent to a CFT tube, the ratio of each pulse height with respect to that of the reference can be

monitored to look for changes in gain. The gain of the reference tube is surveyed using a scintillating material that is connected to it and imbedded with a ^{207}Bi source which produces 1.06 MeV electrons [21]. Both source and flasher events are recorded at regular intervals during an experiment.

6.2 First Level Trigger

The CHAOS first level trigger (1LT) decision is based on multiplicity information provided by the CFT counters. The trigger is a fully programmable system that is flexible and allows for quick changes to its configuration. The timing of the trigger decision is crucial because it provides the gate for all the readout electronics. Some of the readout systems require the gate to arrive a short period of time before the data; thus, a long 1LT decision time necessitates long delays for these signals. This is costly and increases the dead time of the detector. The first level trigger is capable of making a decision in 100 ns. The trigger electronics are based on Emitter Coupled Logic (ECL).

A diagram depicting the first level trigger circuit is shown in figure 6.33. The signals from each CFT block are fed into a programmable discriminator which accepts signals above a set threshold and produces an ECL signal. This particular discriminator also has an analog output, which is delayed and sent to Fast Encoding and Readout ADC's (FERA). The ECL output is then sent to a delay/fanout unit to compensate for different cable travel times. The signals from the delay unit are then directed to a programmable lookup unit (PLU), which outputs different logical combinations of its input. Some of these signals are used for scalers while others are fed into a programmable majority logic unit (MALU), which makes the multiplicity decision. The output of the MALU will open the LAM gate which is a look-at-me signal produced if the first level trigger accepts the event and the data acquisition computer is not busy. A positive decision from the 1LT

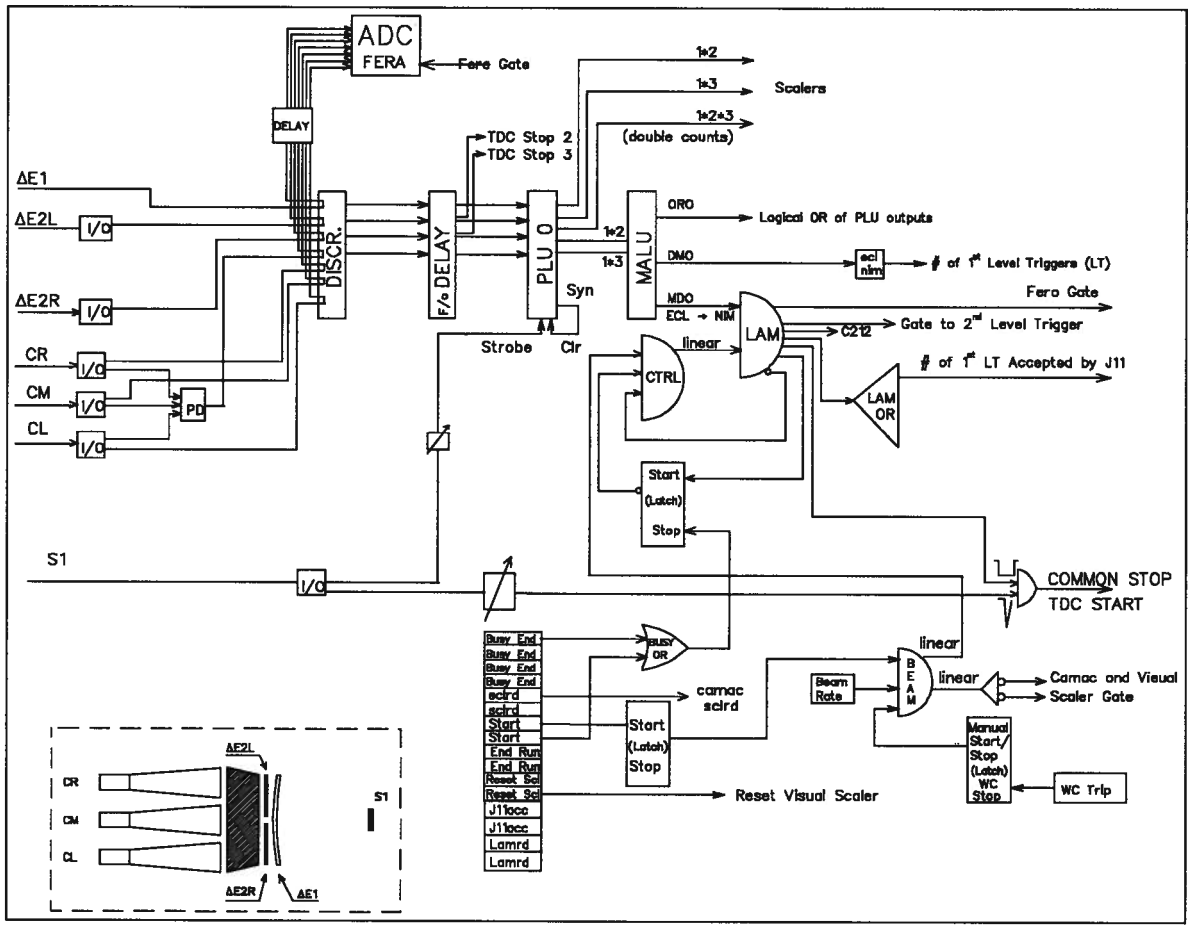

Figure 6.33: Schematic diagram showing the first level trigger. For simplicity, only one of the CFT counters is shown.

initiates the digitization of all chamber data and enables the second level trigger.

Timing of the common start or stop signals for all the TDC's is provided by the S1 counter, which is a plastic scintillator placed in the beam upstream of CHAOS. The stop signal for the CFT blocks is taken after the delay unit and directed through long cables which further delay the signal for the length of time it takes the 1LT to make a decision.

The rest of the circuitry shown in figure 6.33 forms the "BUSY" circuit, which ensures that a single event is processed in each cycle of the trigger. To avoid pileup of events, the LAM gate must be blocked as soon as possible. It remains blocked until the system receives either a computer "BUSY END" indicating that the event has been recorded or a REJECT from the second level trigger.

6.3 Second Level Trigger

The second level trigger (2LT) is one of the most important parts of CHAOS. It enables experimenters to perform a fast hardware rejection of unwanted events which would otherwise be recorded. The system has the ability to make a decision based on physical quantities such as track momentum, polarity and interaction vertex. The 2LT is also based on ECL logic and is fully programmable.[1]

The second level trigger uses the hit information from WC1, WC2 and WC3 to make its decision. It works on the premise that the momentum of a given track is invariant under rotations of the three chamber coordinates. The hit information is obtained from the ECL port of the PCOS III system, and is directed to two Memory Lookup Units (MLU's) A and A′. These modules convert the PCOS information into angles in the CHAOS coordinate system and direct the data for each chamber into the proper data stack. From this point on, three nested DO loops are executed by the hardware. Consider

[1]For a detailed description of this system refer to [22].

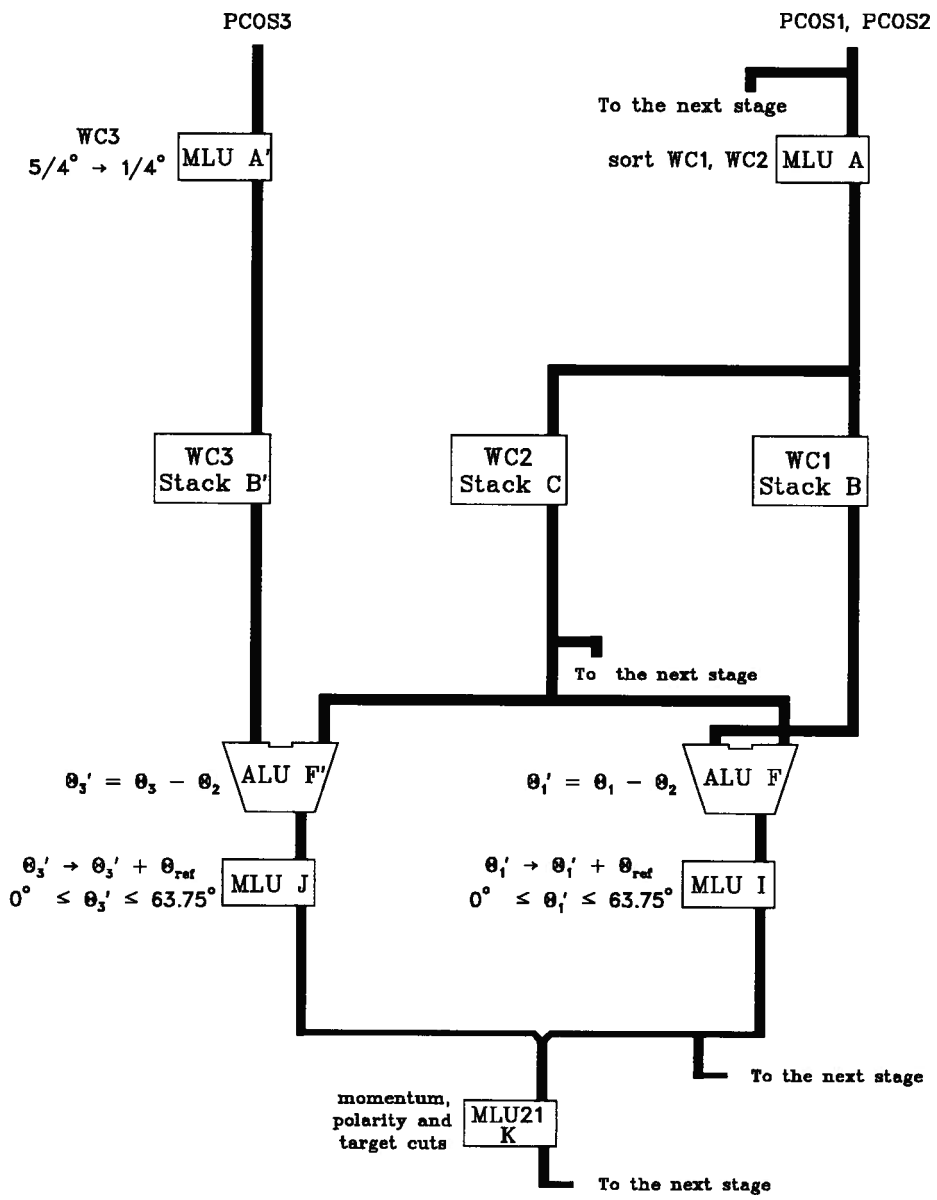

Figure 6.34: Block diagram of the second level trigger. Control signals are not shown.

the case where there are I hits in WC1, J hits in WC2 and K hits in WC3. The first WC2 hit is taken from the data stack and rotated to a predefined angle $\theta_{ref} = 32°$ in the CHAOS system. Thus, the angle of the hit in WC2 is now a known constant. However, to keep the track momentum unchanged the hits from the other two chambers must be rotated by the same amount (ie: $\theta_2 - \theta_{ref}$). This is done by two Arithmetic Logic Units (ALU's) F and F′ along with MLU's I and J. Furthermore, MLU's I and J decide whether the hits are within a 64° window about θ_2. If so, an acceptable track has been found and the data are then passed to MLU21K. This unit calculates the track momentum, polarity, and the distance of closest approach to the center of CHAOS. It will then accept or reject the event based on these calculations. In the latter case, the next set of hits are examined. The process is repeated until either an acceptable track has been found or all I×J×K possibilities have been exhausted. The above forms the first stage of the CHAOS second level trigger.

There are two optional parts of the trigger not shown in figure 6.34. One makes a scattering angle versus momentum cut on single tracks; it is designed to help separate πp elastic scattering events from background reactions involving helium and carbon in the CHAOS target. The other section is a specialized $(\pi, 2\pi)$ trigger which helps separate interesting events from the extensive πp background. It forces the 2LT to find two tracks that pass the first section, calculates the momentum sum and applies an upper sum cut. In addition, it can compare the polarities of the tracks.

6.4 Readout Electronics

The CHAOS readout electronics consist of 1696 ADC, 944 TDC and 1584 PCOS channels. Each of these systems is discussed in the following sections.

6.4.1 PCOS & 4290 TDC System

The three inner chambers are equipped with a LeCroy PCOS III system that is based on ECL logic. It consists of a set of model 2731A 32 channel latches, three 2738 PCOS controllers and two 4299 databus interfaces. In order to allow for cluster mode operation, there are two latch addresses corresponding to each chamber wire. Hence, 1440 channels are allocated for each of WC1 and WC2. In addition, 288 channels are set aside for WC3.

The signals from the preamplifiers are directed to LeCroy 2735PC cards, which output an ECL signal if the analog input is above a certain threshold. This level is separately programmable through the latch modules. The output of the 2735PC cards is sent to the 2731A units and sets the corresponding latches. After the system receives a gate from the first level trigger, it reads the latches and outputs the address of the wire(s) that fired. If two or more adjacent wires were activated, it will group them into a cluster whose width is given by the number of wires that fired. In such cases, the output address corresponds to the average address of the activated channels. If a particle activates the first and the last wire in the chamber, the system will output two clusters of width one. Fast transfer of data to the second level trigger is made possible by the ECL ports of the 2738 PCOS controller. Data transfer is possible up to a rate of 10 MHz. The 4299 databus interface buffer is used to readout the data through CAMAC. This occurs if and only if the second level trigger has accepted the event. Otherwise the module is cleared.

Wire chambers 3 and 4 are instrumented with the LeCroy 4290 Drift Chamber system. This consists of 2735DC preamplifier/discriminator cards, 4291B time digitizer modules, 4298 TDC controllers and a 4299 databus interface module. Each 4291B TDC has 32 front panel differential ECL inputs which accept chamber signals from the 2735DC cards. Unlike the PCOS III system, the threshold for the 2735DC cards is controlled manually.

Normally, the 2735DC cards are mounted directly on the chamber, but lack of space

inside the spectrometer does not allow for this. The chamber signals had to be brought to crates containing the 2735DC cards via coaxial cables; the resulting attenuation required the use of 8-channel preamplifiers, which resulted in the over-amplification of both the signal and noise. As such, the thresholds on the 2735DC's were often set near maximum. In WC3 the maximum threshold values were not sufficient to filter out the noise. Hence, a 17 KΩ resistor to ground was connected to each input channel of the 2735DC cards. This had the effect of attenuating the input such that the noise was below the maximum threshold.

Each 4298 controls up to 23 time digitizer modules and rejects zero or full scale TDC values. The system can operate in either COMMON STOP or COMMON START mode. CHAOS operates in the former mode. This is so that the chamber signals need not be delayed. The common stop is provided by a scintillator located at the entrance of the beam into CHAOS. The TDC's have an adjustable range between 500 ns and 2 μs, and the conversion time for 9 bit accuracy is 35 μs. The 512 ns range chosen for CHAOS results in 1 ns time resolution and is near the longest drift times in WC4 ($\approx$ 400 ns)

The TDC controller is capable of producing accurate time marks. This feature allows for a stop signal to be produced at a precise interval of time after the start, which is useful for calibration purposes. If all the preamplifiers are fired at the same time by an external pulse distribution system and a COMMON STOP signal is produced at a precise interval of time later, all the TDC values should be the same. However, this is not the case because the wires carrying the signals from the preamps to the TDC's have different lengths. In the above scenario the system is capable of correcting for this if operated in AUTOTRIM mode.

6.4.2 FASTBUS

The LeCroy FASTBUS ADC system is used to digitize the signals from the chamber cathode strips and resistive wires. Although the faster FERA system could also be used, the cost of such a system is much greater than FASTBUS. The FASTBUS system consists of a single 1821 segment manager, nineteen 96 channel 1882F ADC's, one 1810 Calibration And Trigger module (CAT), one 1821/ECL auxiliary card, a single 1691A-PC interface card, two 4302 memory modules, and one 2891A FASTBUS port. Apart from the 4302's, 1691A, and 2891A, all other modules are located in a Struck FASTBUS crate. The system is capable of pedestal subtraction, threshold comparison, and zero suppression. This is required in order to eliminate the readout of unwanted information.

The 1821 segment manager is a processor that controls all the ADC's and the CAT. It configures the pedestal system and reads the ADC's after the digitization process is complete. The pedestal system can be configured in one of the following ways.

- No pedestal subtraction
- Pedestal subtraction only
- Pedestal subtraction and suppression of negative values to zero
- Pedestal subtraction and suppression of negative values out of the memory

This is done through writing the proper code in Register 3 of the 1821. CHAOS uses the last of the above options. Another useful feature of the segment manager is the threshold register which allows one to set a common (to all ADC channels) threshold that is added to the pedestal value in each channel. The ADC data are readout only if they are greater than the sum of the pedestal and threshold in the corresponding channel. This feature is used in CHAOS since the width of the pedestal distribution

for each channel is not negligible. The source and the destination of the digitized data are also configured through Register 3. The data can either be piped from the pedestal system to the segment manager memory or it can be sent to an auxiliary card located at the rear of the unit. The latter option is more practical since it allows for faster readout of data. The 32 bit data words from the auxiliary card are stored in two 4302 modules. Each 32 bit data word contains 16 bits of address and 16 bits of data. Since the 4302 modules used to receive the FASTBUS data are 16 bit units, one was used to receive the data and the other the address.

Instruction words can be downloaded into the processor's memory either through CAMAC or through SONIC, which is a low level language developed by LeCroy. The SONIC code is compiled and downloaded using the LeCroy Interactive FASTBUS Toolkit program (LIFT) running on a PC which uses the 1691A-PC card to communicate with the 1821. A SONIC program is used to configure the ADC's and read out the data. Two inputs and a single output located on the front panel of the 1821 are used in the readout sequence. For diagnosis and configuration purposes, a control program was developed which runs on a VAX system and allows for communications via CAMAC using the 2891A FASTBUS port. In practice, LIFT is used to download the instruction words required for the readout procedure into the 1821 memory. The pedestal system and threshold register are configured with the VAX system.

The 1882F's are 96 channel ADC's. The gate to the ADC can be provided either through the front panel or through the back plane using the 1810 CAT. The front or back panel options are configured via the Control Status Register (CSR) of the 1882F through the segment manager at powerup. The 1882F requires the gate to arrive at least 40 ns before the signal, thus all of the ADC signals had to be delayed for this period of time plus the 100 ns required to make the 1LT decision. The conversion time for this module in 256 μs.

The 1810 CAT sends the gate and the clear to all the ADC's through the back panel. The unit can also be used to inject specified amounts of charge into the ADC's. This allows for the calibration of the ADC's and location of faulty modules. A useful feature of the 1810 is the Measure Pause Interval (MPI). When this signal is held true, it prevents ADC's from commencing the digitization process. It can either be programmed into the 1810 or input externally through the front panel. As soon as the gate is received by the CAT, it will start the MPI and set the BUSY output on its front panel to true. During the MPI a clear signal will return the ADC's to acquisition mode and set BUSY to false. If the clear signal is sent within the MPI, the ADC's require 500 ns to clear; otherwise 5 μs is needed. Hence, the MPI is set to the maximum second level trigger decision time.

To calculate the ADC pedestals, a gate of the same width as the one generated by the first level trigger is sent to the modules. The ADC's are then read out and recorded with the VAX system. The above process is repeated a number of times and for each channel, the pedestal is set to the average of the recorded ADC values. Note that the above is done when no beam is present in the area and all preamps are powered. Pedestals are calculated at regular intervals during the course of an experiment.

Readout Procedure

The flow chart for the SONIC code used to readout the ADC data is shown in figure 6.36, and the schematic diagram of the handshaking circuit is illustrated in figure 6.35. At powerup, the Control Status Registers of the ADC's and CAT are configured so that the ADC gate is sent via the back plane through the 1810. The input (IN1) on the front panel of the 1821 is examined until it is set to true by the MPI output of the 1810. The processor will wait the length of the MPI plus the period of time required for possible clearing. It will then examine the BUSY output of the CAT via the front panel input (IN2). If BUSY is false the system is returned to acquisition mode, otherwise it will

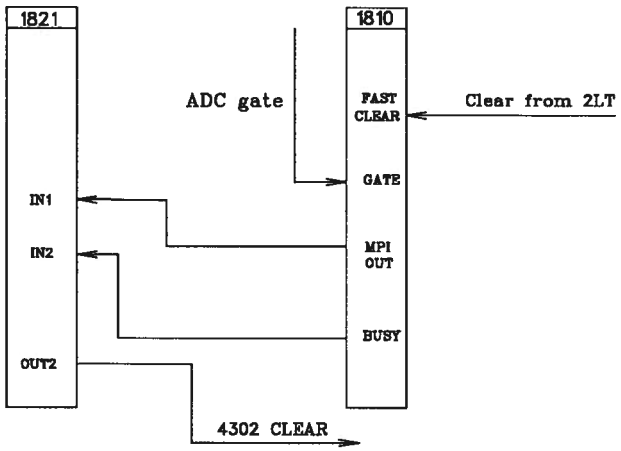

Figure 6.35: Schematic diagram of the FASTBUS handshaking circuit.

wait for data conversion. The 1821 will then clear the 4302 memory via the front panel output (OUT1) and read the ADC's. At this point, the data are sent to the 4302's, and the system is returned to acquisition mode.

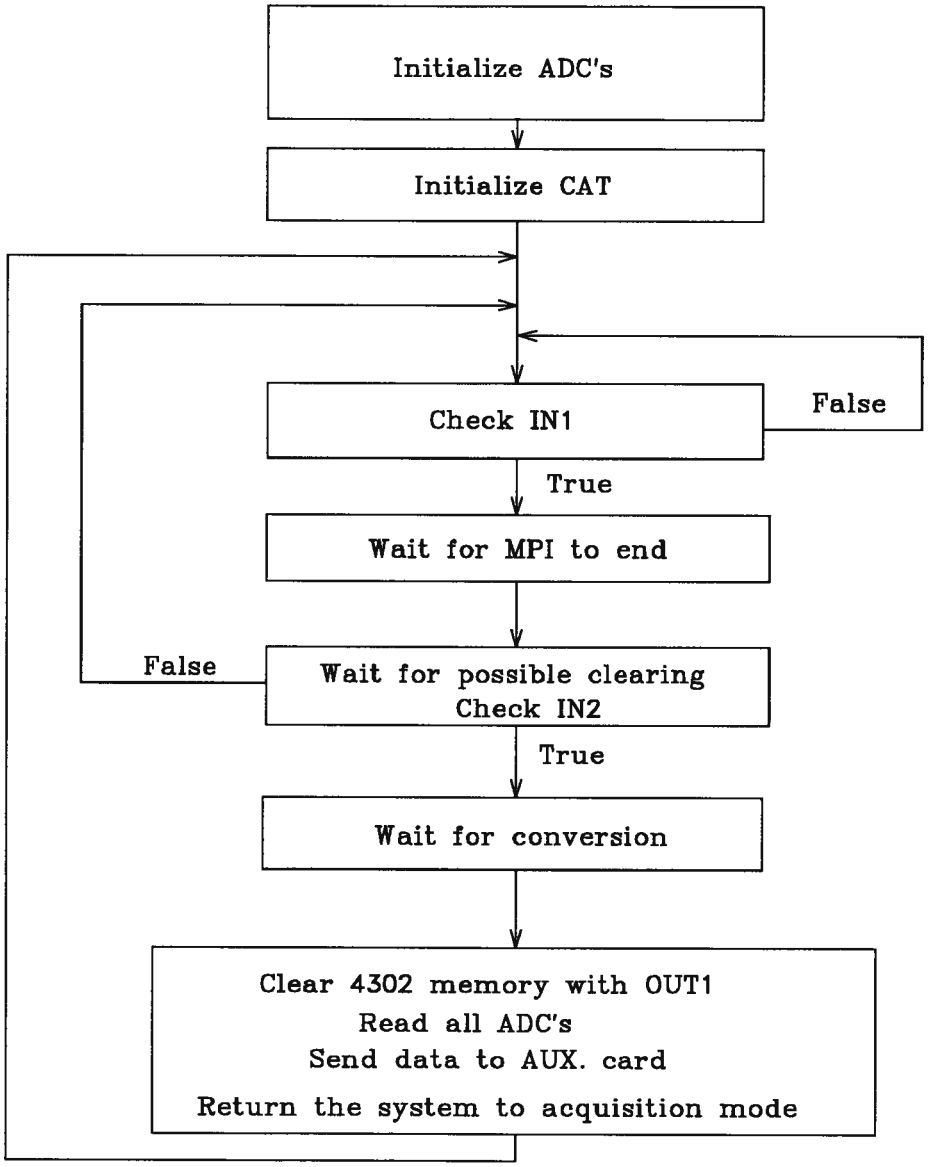

Figure 6.36: Flow chart of the FASTBUS readout algorithm.

Chapter 7

Chamber Calibration

In order to determine the position of every hit for a given track two things must be known. These are, the chamber positions and time distance relations. This chapter deals with the procedures used for determination of these parameters. CHAOS chamber calibrations are divided into two parts. One is the in-plane calibration, and the other is the vertical coordinate calibration. The software and techniques for the former were developed by Gertjan Hofman [23].

7.1 In-plane Calibration

This task consists of calculating offsets and time-distance relations for the various chambers. Offsets are required in order to accurately determine the position of each chamber in the CHAOS coordinate system. Although great care was taken in installing the chambers, a more accurate knowledge of chamber positions is needed. The calibration of the two inner chambers requires determinations of position offsets only. WC3 and WC4 are however drift chambers; for these detectors, offsets as well as time-distance relations must be determined. Furthermore, space-time (x(t)) relations are needed for various magnetic field settings. In the calibration procedure, the x(t) relation for each chamber is a lookup table that associates a distance with a given drift time. WC3 calibration is more difficult than WC4, because it is located in a region of high magnetic field and has a single wire plane. As a result, the x(t) relations are nonlinear and internal consistency checks can not be performed. WC4 on the other hand, is in a region of low field and has eight planes

of wires.

The chamber positions, rotation offsets and zero field x(t) relations are determined by analysing straight tracks (B = 0) in which all 22 chamber hits (11 for beam in and 11 for beam out) are present. The position and zero magnetic field x(t) determination procedure can be summarized as follows.

- The positions of the hits in WC1, WC2, and WC4 are calculated using the initial guesses for the offsets and x(t) relations.

- The position of the track in WC3 is determined. In polar coordinates, this is given by

$$R = 347.55\ mm$$
$$\theta = \theta_w \pm \phi(\gamma, t_{drift}) \tag{7.58}$$

  where R is radius of the chamber and θ_w is the angle of the activated wire in the CHAOS coordinate system. In addition, $\phi(\gamma, t_{drift})$ is the angular distance of the hit from the wire. This is a function of the drift time, t_{drift}, and the incident angle of the track with respect to the cell, γ (see figure 7.37). The sign of $\phi(\gamma, t_{drift})$ depends on whether the track passed on the right or the left of the sense wire. The value of γ is calculated through an iterative procedure. Initially, γ is set to zero for both the incoming and the outgoing hits and a linear regression is performed on all of the hits from WC1, WC2, WC3, and WC4. Using the slope of the fitted line a new value of γ is obtained. Next, the WC3 track position is updated and another fit is performed. The above procedure is repeated until the change is γ is negligible.

- A straight line is fit to the 22 sets of coordinates.

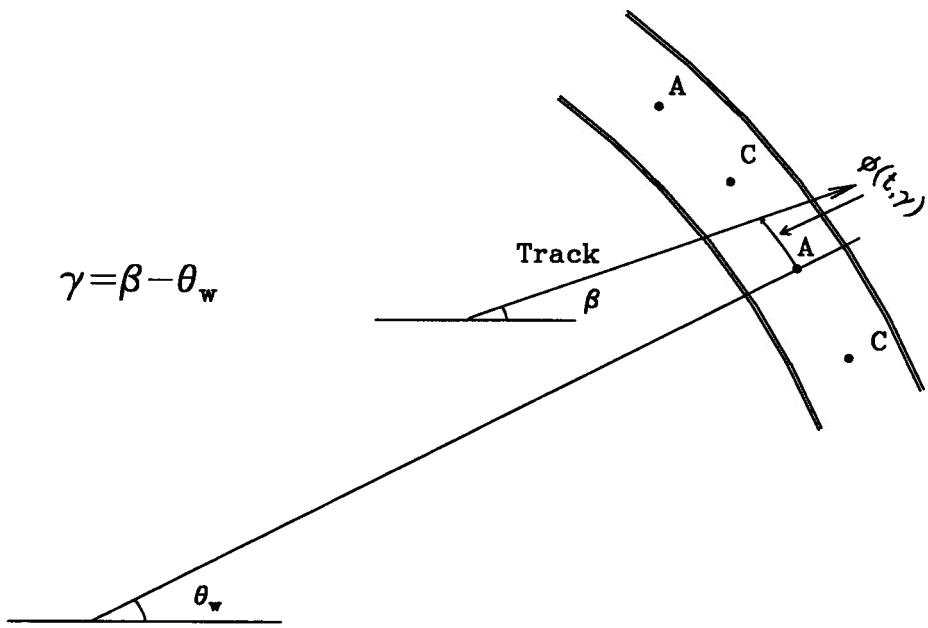

Figure 7.37: Illustration of the incident track angle γ in WC3. A and C denote anode and cathode wires respectively. Chamber cell is not drawn to scale.

- The slope and the intercept of the line are transformed to a reference frame in which all the chambers are centered at (0,0).
- Residuals representing corrections to the x(t) relations and offsets are calculated using the following equations:

$$x(t)_{new} - x(t)_{old} = \mid \phi_{cross} - \phi_{chamber} \mid \times side \tag{7.59}$$

$$\delta x_{new} - \delta x_{old} = \sin(\theta_w) \times (\phi_{chamber} - \phi_{cross}) \times \frac{\pi}{180} R_{chamber} \tag{7.60}$$

$$\delta y_{new} - \delta y_{old} = \cos(\theta_w) \times (\phi_{chamber} - \phi_{cross}) \times \frac{\pi}{180} R_{chamber} \tag{7.61}$$

$$\delta\theta_{new} - \delta\theta_{old} = (\phi_{chamber} - \phi_{cross}) \tag{7.62}$$

where ϕ_{cross} is the angle of intersection of the line and the anode plane of each

chamber in the transformed frame, and $\phi_{chamber}$ is the polar angle of the original hit in the CHAOS system. δx_{new} and δx_{old} represent the improved and the initial estimates of the x offsets respectively, similarly for δy_{new} and δy_{old}. In addition, θ_w is the polar angle of the wire in the transformed frame, *side* is the left-right flag ($\pm$ 1), and $R_{chamber}$ is the chamber radius. The initial estimates and the improved values of the rotational offsets are denoted by $\delta\theta_{old}$ and $\delta\theta_{new}$, respectively. For WC4, the equivalent of ϕ_{cross} is obtained by calculating the intersection of the fitted line with the electron drift trajectories which are assumed to be perpendicular to the radial vector passing through the activated anode.

- A large number of tracks are analyzed and the above residuals are summed and averaged over the contributing tracks. This yields corrections to the offsets and the space-time relations. In order to determine the position offsets accurately, it was necessary to acquire data (straight tracks) at 0 and 90° in the CHAOS coordinate system.

- Improved values of offsets are obtained and new x(t) look up tables are created. In the case of WC3, the x(t) relation is a 2 dimensional lookup table that associates a drift distance with a given value of drift time and γ, at a given magnetic field setting. In this table, the angle of incidence is specified to the nearest degree and the drift time to the nearest ns.

- The entire cycle is repeated with the same tracks.

Several important points need to be stressed. First, once the residuals are added all fictitious corrections will sum to zero. As an example, consider the case where a chamber has no translational offsets and only a rotational offset is present (see figure 7.38). Furthermore, assume that the x(t) relation is known. In this case, the X and Y

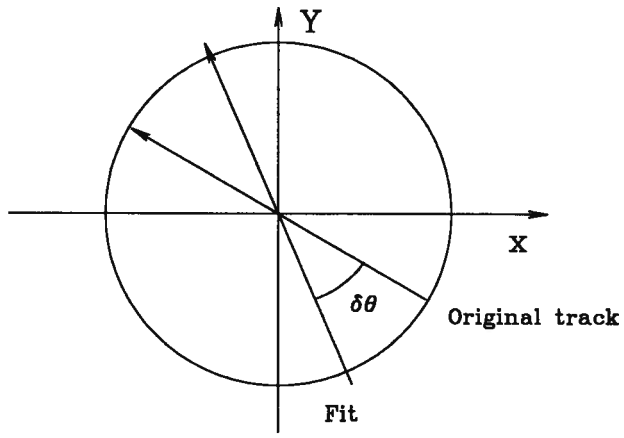

Figure 7.38: Illustration of rotation offsets is shown. The offset has been exaggerated for clarity.

residuals for the incoming and the outgoing hits are equal but have opposite signs. As such, they add up to zero. Similarly, corrections to the x(t) relation vanish, because, given a large number of tracks, as many pass to the left as right. Second, in the case of WC1 and WC2 no x(t) relation is needed; only position and rotation offset corrections are calculated. Figure 7.39 shows the X and Y residuals for WC3 before and after the calibration procedure.

7.2 Magnetic Field Corrections

Once chamber positions are known, WC3 x(t) relations for the various magnetic field values must be determined. Tracks with different momenta are analyzed to obtain a wide range of incident angles. Using the Quintic Spline method outlined in section 8.1, an analytical form for the trajectory of the particle in the magnetic field is obtained [1].

[1]The analytic form is presented in section 8.1

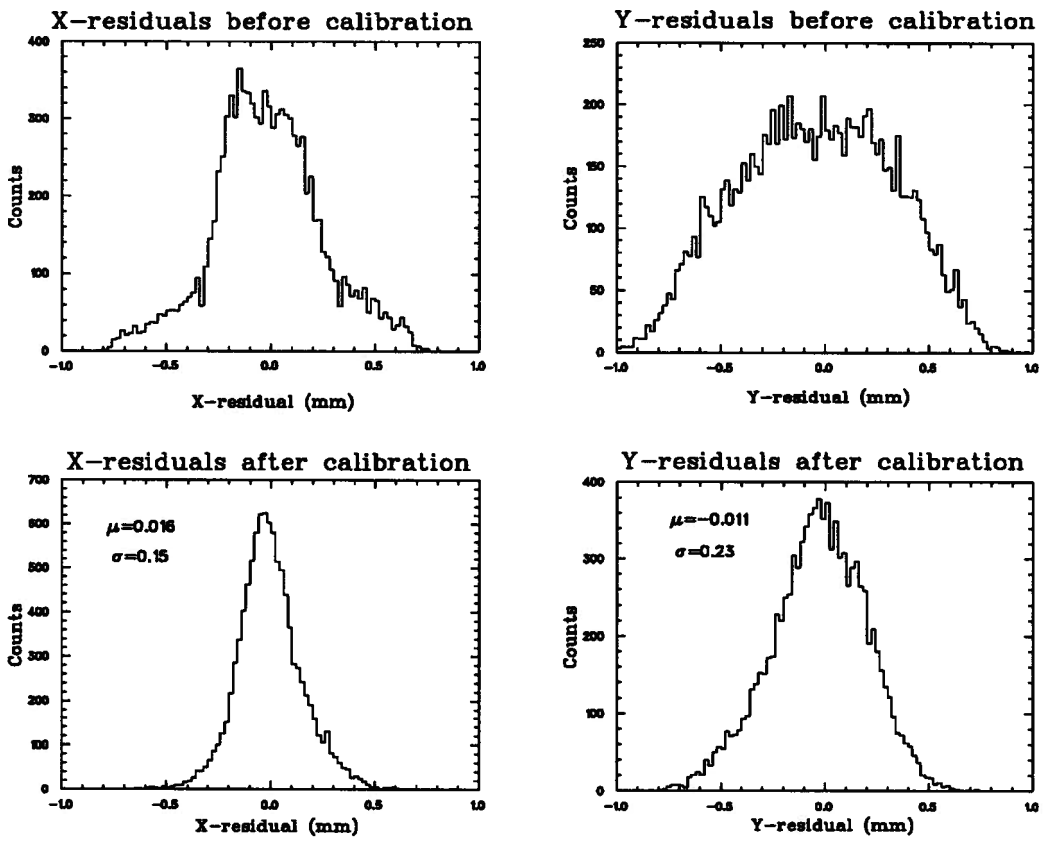

Figure 7.39: X and Y residuals prior to and after the calibration along with position centriods (μ) and standard deviations (σ) for WC3 with B=0 are shown.

The trajectory is calculated based on an initial estimate of the time-distance relation [2]. The tangent to the trajectory at its intersection with the anode plane of WC3 provides a new value of γ and results in a new position for the hit. The Quintic Spline method is applied once again and the polar angle of the intersection of the track and the chamber in the CHAOS system, ϕ_{fit}, is found by simultaneously solving the system of equations formed by the circle describing the WC3 anode plane and the analytic form of the track.

[2]Initial estimate of γ is zero.

The angular distance corresponding to a given drift time and incident angle, γ, is given by

$$\phi(t,\gamma) = \mid \phi_{fit} - \theta_w \mid \tag{7.63}$$

where θ_w is the angle of the sense wire with respect to the CHAOS coordinate system. The procedure outlined above is repeated for a large number of tracks, illuminating a large number of cells. In practice, the actual data recorded in the acquisition phase of a given experiment can be and in fact are the best data to use in this procedure. Consequently, WC3 can be considered a "self calibrating" chamber. The values of $\phi(t,\gamma)$ for constant angles of incidence are summed and averaged over the contributing tracks. A third order polynomial fit is performed on the drift distance versus drift time at each value of γ, which is then used to create a new x(t) lookup table, and the same tracks are reanalysed using the improved x(t) relations. The above procedure is repeated until the change in the x(t) relation is negligible. Figure 7.40 shows time-distance (angular) residuals before and after calibration. The standard deviation of the time distance residual distribution is the effective chamber resolution. To date, magnetic field corrections are not applied to WC4 time-distance relations where B is only $\sim$ 20% of the central value. This will be implemented in the near future.

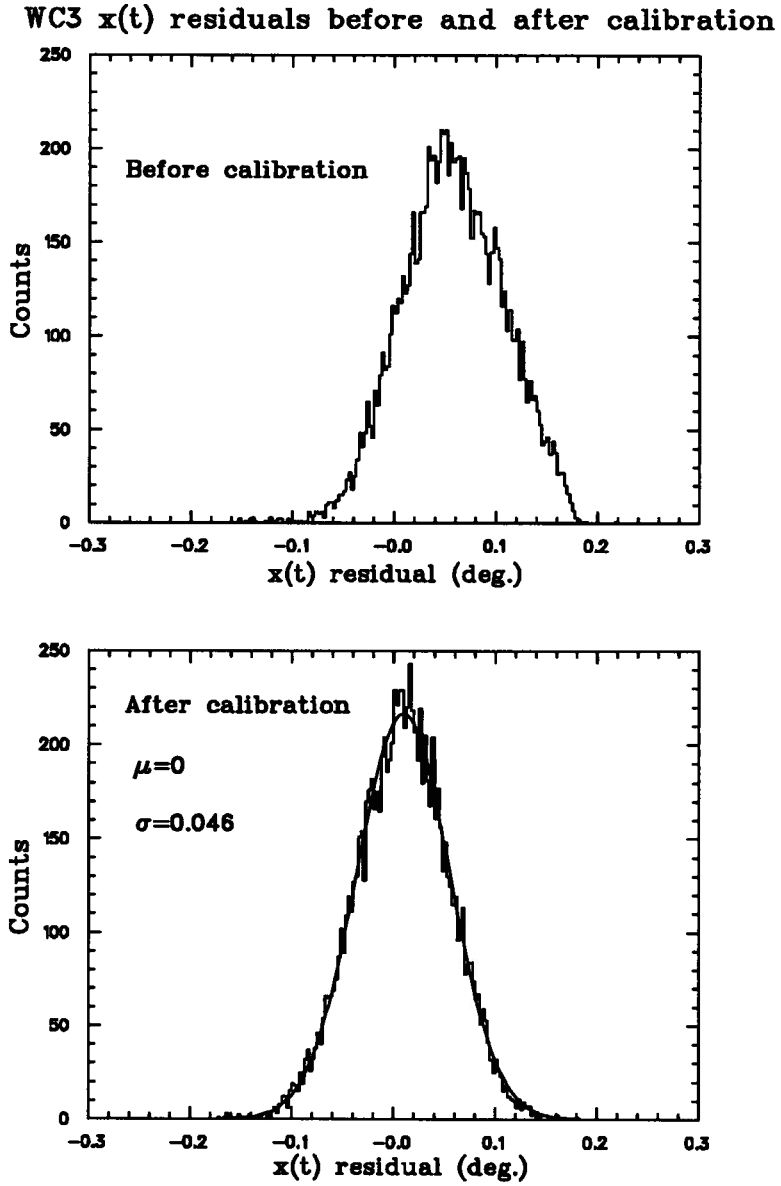

Figure 7.40: WC3 x(t) residuals prior and after calibration for magnetic field setting of 1.2 T.

7.3 Vertical Calibration

The vertical position of a track, z, is determined from the hits in WC1, WC2, and WC4. The vertical position in chamber four is given by

$$z = \frac{t-b}{t+b} \times \frac{l}{2} + z_o \tag{7.64}$$

where t and b are the adc values for the top and the bottom of the resistive wire. In addition, l is the electrical length and z_0 is the vertical offset. The vertical position in chambers one and two are corrected by means of an offset.

$$z_1 = z_c^1 + z_0^1 \tag{7.65}$$

$$z_2 = z_c^2 + z_0^2 \tag{7.66}$$

Here, z_1 and z_2 are the corrected z-positions in WC1 and WC2 respectively; similarly, z_c^1 and z_c^2 are the original z positions obtained from the chambers. Last, z_0^1 is the WC1 vertical offset and z_0^2 represents the vertical offset in WC2.

The electrical lengths for the inner and outer resistive wires were obtained by direct measurement. A single section of the chamber was placed on an Y-Z table and positioned in the beam. A thin scintillating fiber ($1 \times 1\ mm^2$) mounted horizontally was placed in coincidence with two other large scintillator paddles to provide the trigger. The chamber was moved vertically by precise amounts while keeping the fiber fixed. The ratio of the difference to the sum of the adc values at ends of the wire was recorded for a large number of tracks. Figure 7.41 shows the position of the chamber relative to an arbitrary fixed point in space as a function of this ratio. This graph shows a linear relation between the ratio and chamber displacement; the electrical length is just twice the slope of this line. The electrical lengths for the inner and the outer wires were found to be 237.6 mm and 248.8 mm respectively. In the above process two cells (4 resistive wires) were tested and

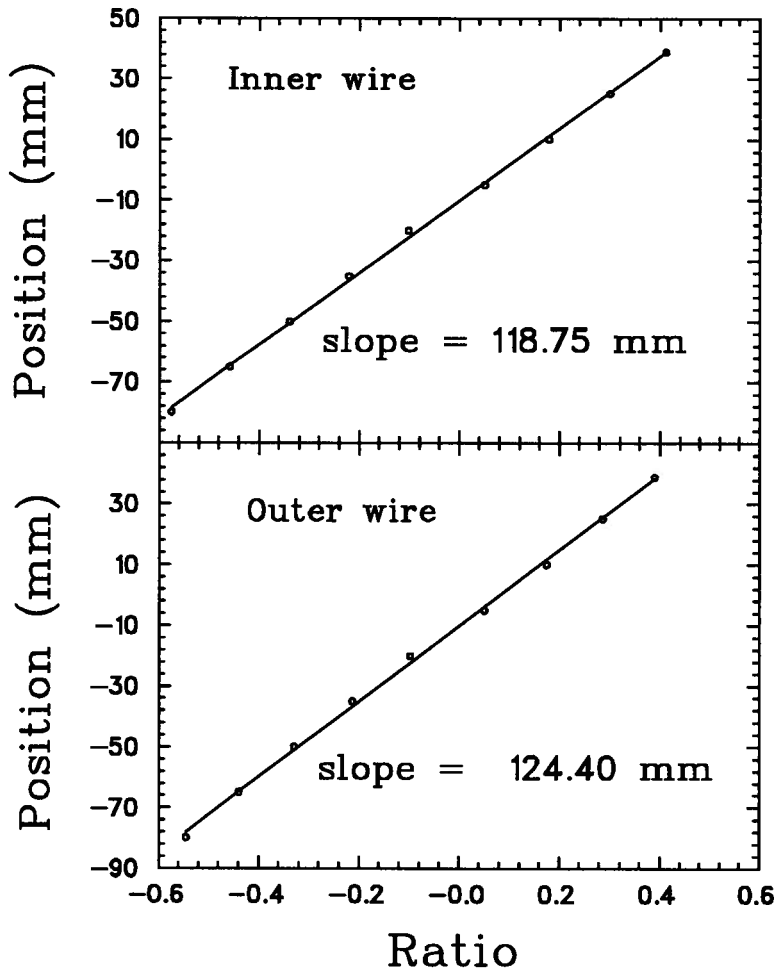

Figure 7.41: Graph of ratio versus displacement for the inner and the outer resistive wires. The solid lines are straight line fits to the data. The slopes shown are half of the electrical lengths.

the results were internally consistent. In each case, the inner and the outer wire were found to have different electrical lengths; the reason for this is not clear. The lengths obtained from each cell were the same to better than 0.5 mm. The electrical lengths are close to the physical length of the wires which is 250 mm and were assumed to be the same for all other sections of the chamber. Once the electrical lengths are determined, the offsets for the three chambers can be determined by analysing tracks from a scattering run with zero magnetic field setting. The calibration algorithm is outlined below.

- The interaction vertex in the X-Y plane is calculated using the anode information from all four chambers.

- All z offsets are initially set to zero and z-positions are calculated for each chamber.

- The distance between the interaction vertex and the hit in WC1 (d_1) and WC2 (d_2) in the X-Y plane is obtained. Similarly, the distance from the vertex to each activated resistive wire (d_i^4) is calculated.

$$d_1 = \sqrt{(x_1 - x_v)^2 + (y_1 - y_v)^2} \tag{7.67}$$

$$d_2 = \sqrt{(x_2 - x_v)^2 + (y_2 - y_v)^2} \tag{7.68}$$

$$d_i^4 = \sqrt{(x_i^4 - x_v)^2 + (y_i^4 - y_v)^2} \quad (i = 1, 2) \tag{7.69}$$

  where (x_v, y_v) denotes the interaction vertex point, and (x_1, y_1), (x_2, y_2) represent the position of the hit in WC1 and WC2, respectively. In addition, (x_i^4, y_i^4) is the location of the ith activated resistive wire in the CHAOS coordinate system.

- A straight line fit is performed on z versus the distance from the vertex for those tracks in which all 4 possible vertical coordinates are present.

- Residuals for WC1, WC2 and each hit wire in WC4 are calculated. These are given by

$$\delta z_1 = z^1_{fit} - z^1_{ch} \tag{7.70}$$

$$\delta z_2 = z^2_{fit} - z^2_{ch} \tag{7.71}$$

$$\delta z^i_4 = z^4_{fit} - z^4_{ch,i} \tag{7.72}$$

  Where δz_1, z^1_{ch}, δz_2, and z^2_{ch} are the residuals and the original z-position for chambers one and two respectively. Similarly, δz^i_4 represents the residual for the ith wire in chamber four and $z^4_{ch,i}$ is the vertical position of the hit as seen by the ith wire in the chamber. In addition z^1_{fit}, z^2_{fit}, and z^4_{fit} are the z coordinates calculated from the fit.

- A large number of tracks, distributed over all cells, are analysed.

- The residuals are then summed and averaged over the tracks that contributed to them, and new offsets are obtained.

- The improved offsets ares stored and a new set of z-positions calculated.

- The entire cycle is then repeated for the same tracks until corrections are negligible.

In order to eliminate stray hits such as those produced by electromagnetic noise and particle decay, tracks with large residuals were not considered. The residuals before and after the calibration procedure are shown in figures 7.42 and 7.43. In these figures, WC4 residual represents the corrections for all of the hit wires. The standard deviations of the distributions in figure 7.43 represent the effective vertical resolution of each chamber. The vertical resolutions obtained for WC2 and WC4 are reasonable; WC4 resolution is better than 1% of the electrical length. It is expected that WC1 resolution will be improved by increasing the chamber operating voltage.

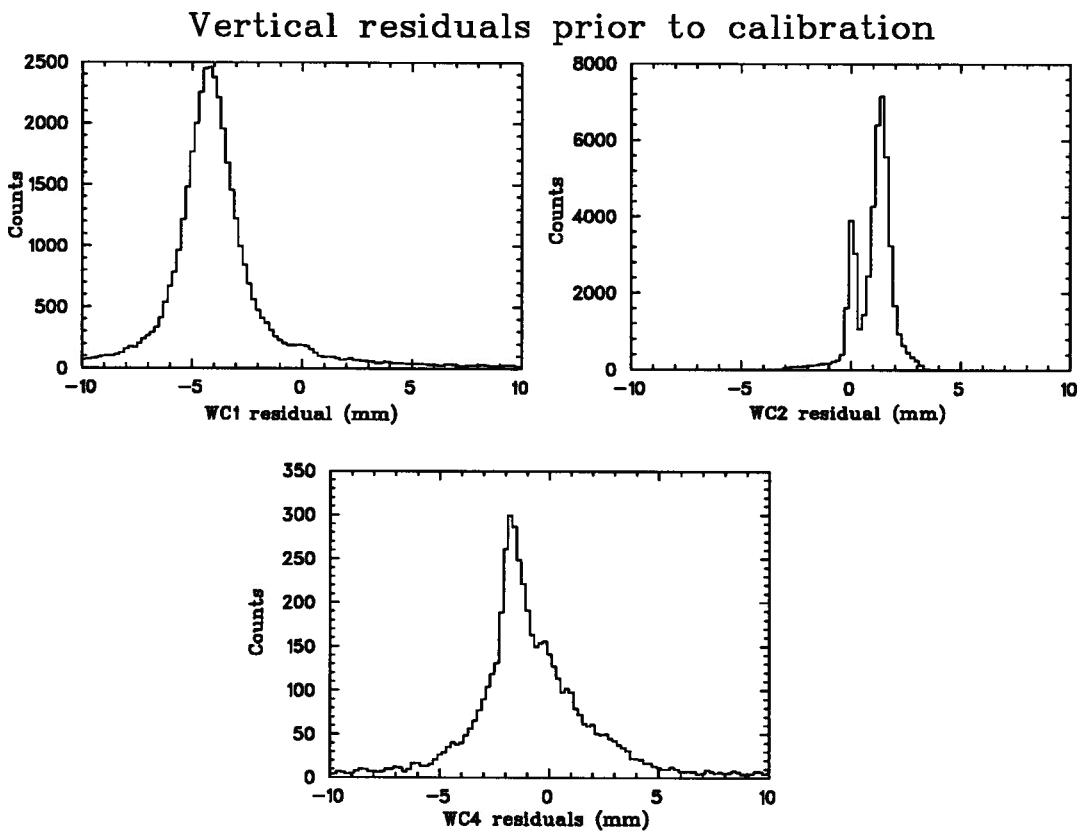

Figure 7.42: Z coordinate residuals for WC1, WC2, and WC4 before the calibration process are shown (ie: with all offsets set to zero).

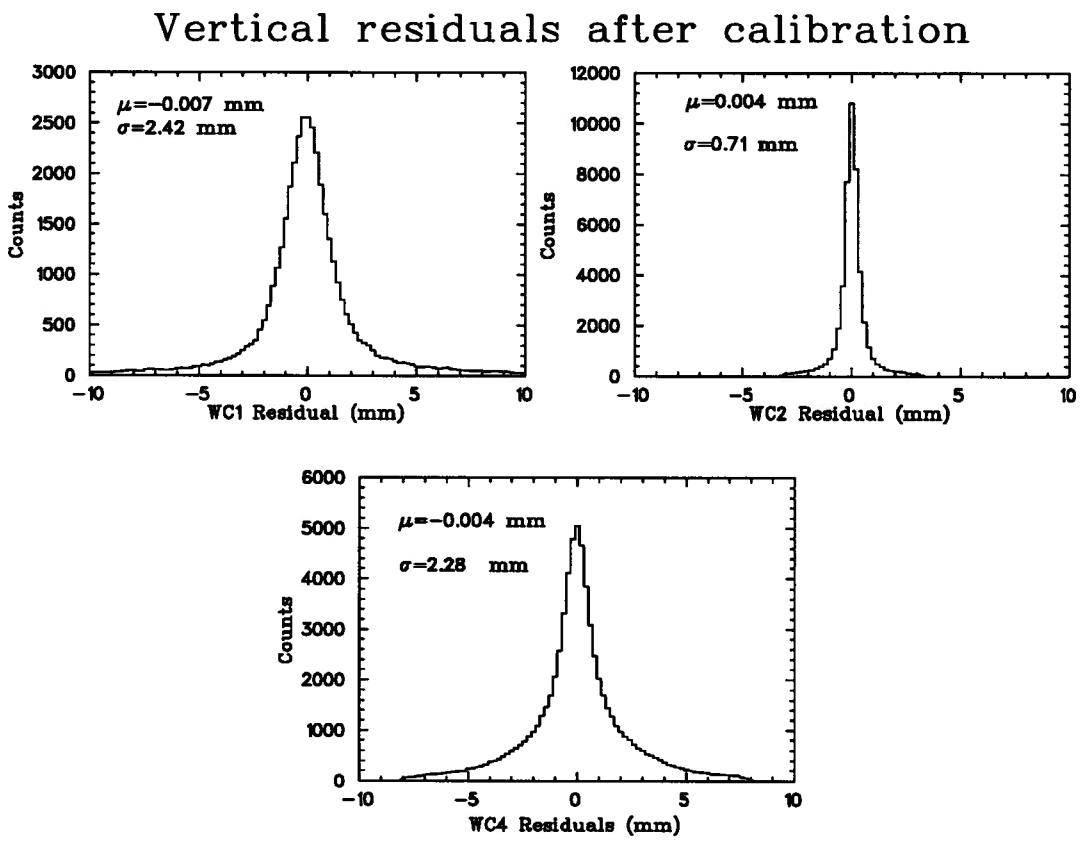

Figure 7.43: Z coordinate residuals for WC1, WC2, and WC4 after the calibration process. The standard deviations (σ) show the effective z resolution of each chamber.

Chapter 8

Reconstruction

8.1 Momentum Reconstruction

To date, the momentum reconstruction algorithm is implemented in two dimensions only. The momentum calculation technique employs the Quintic Spline method developed by Wind [24]. The software for this part was developed by Roman Tacik [25].

The equations of motion in natural units for a charged particle with momentum $\vec{P}$, moving in a magnetic field $\vec{B}$ are given by[1]

$$\frac{d\vec{P}}{dt} = q\vec{v} \times \vec{B} \tag{8.73}$$

where q and $\vec{v}$ are the charge and velocity of the particle, respectively.

Given that the field points along the z direction, the above reduces to

$$\frac{d^2x}{dt^2} = \frac{qB}{\gamma m}\frac{dy}{dt} \tag{8.74}$$

$$\frac{d^2y}{dt^2} = \frac{-qB}{\gamma m}\frac{dx}{dt} \tag{8.75}$$

Here, B is the magnitude of the field at a point (x,y) and m is the mass of the particle. In addition, γ (in natural units) is defined by equation 8.76,

$$\gamma = \frac{1}{\sqrt{1-v^2}} \tag{8.76}$$

where v is the magnitude of the velocity.[2] The first and second time derivatives can be

[1] The field is not uniform but is rather a function of x and y.

[2] γ is constant since the energy of the particle does not change with time.

eliminated by successive application of the chain rule:

$$\frac{dy}{dx} = \frac{\frac{dy}{dt}}{\frac{dx}{dt}} \tag{8.77}$$

$$\frac{d^2y}{dx^2} = \frac{\frac{d^2y}{dt^2}\frac{dx}{dt} - \frac{d^2x}{dt^2}\frac{dy}{dt}}{(\frac{dx}{dt})^3} \tag{8.78}$$

Using the equations of motion the above expression can be written as

$$\frac{d^2y}{dx^2} = \frac{-qB}{\gamma m}\left(\frac{(\frac{dx}{dt})^2 + (\frac{dy}{dt})^2}{(\frac{dx}{dt})^3}\right) \tag{8.79}$$

Using relation 8.77, the above reduces to

$$\frac{d^2y}{dx^2} = \frac{-qB}{\gamma m\frac{dx}{dt}}\left(1 + (\frac{dy}{dx})^2\right) \tag{8.80}$$

Now, the momentum P is defined as

$$\begin{aligned} P &= \gamma m\sqrt{(\frac{dx}{dt})^2 + (\frac{dy}{dt})^2} \\ &= \gamma m\frac{dx}{dt}\sqrt{\left(1 + (\frac{\frac{dy}{dt}}{\frac{dx}{dt}})^2\right)} \end{aligned} \tag{8.81}$$

Employing the results of 8.77, the momentum is given by the following:

$$P = \gamma m\frac{dx}{dt}\sqrt{1 + (\frac{dy}{dx})^2} \tag{8.82}$$

Combining the results of 8.80 and 8.82 yields

$$P\frac{d^2y}{dx^2} = -qB\left(1 + (\frac{dy}{dx})^2\right)^{\frac{3}{2}} \tag{8.83}$$

Equation 8.83 establishes a simple relation between the analytic form of the particle's trajectory and its momentum. From basic calculus, it is clear that

$$y = a + bx + \frac{1}{P}\int_0^x d\alpha \int_0^\alpha (P\frac{d^2y}{d\tau^2})d\tau \tag{8.84}$$

where a and b are integration constants. Hence, if the double integral is known, the momentum is obtained by fitting the coordinates of the track to equation 8.84.

The momentum calculation algorithm is summarized in the following.

- The hits in WC1, WC2, and WC3 are used to obtain the 3 coefficients of the circle passing through them.
- From the equation of the circle two pseudo hits are generated. One is between WC1 and WC2 and the other lies between WC2 and WC3.
- A straight line fit is performed on the hits in WC4.
- A cubic spline is used to generate pseudo hits between WC3 and WC4.
- The analytic forms of the circle, spline and straight line are differentiated to obtain $\frac{dy}{dx}$ at all track and pseudo hit coordinates.
- Given the polarity of the track (from the direction of curvature) and the magnetic field strength at each point, equation 8.83 provides the corresponding value of $P\frac{d^2y}{dx^2}$.
- A cubic spline fit is applied to the values of $P\frac{d^2y}{dx^2}$.
- The polynomial obtained from the cubic spline fit (above) is analytically integrated twice and the value of the integral at each chamber hit is recorded. The double integral yields a fifth order polynomial, hence the name Quintic Spline.
- Once the double integral is known, an analytic form for the track in terms of a fifth order polynomial is given by equation 8.84. A least square minimization between the values of y obtained from 8.84 and the chamber hits yields the constants a, b and $\frac{1}{P}$. The pseudo hits are not used in the minimization.
- $\frac{dy}{dx}$ is recalculated from the equation for the track, and the cycle is repeated once more to obtain a stable value of P.

8.2 The Interaction Vertex and Scattering Angle

Once the track momentum has been found the interaction vertex can be calculated. The vertex is defined to be the intersection of the incoming and scattered particle track. The horizontal and vertical coordinates of the vertex are computed separately.

Consider the interaction vertex in the x-y plane. Assuming a uniform magnetic field in the region of the target, the trajectory of the incoming beam is circular in that region and is obtained analytically using the two hits in WC1 and WC2, the known beam momentum and polarity along with the field direction and strength (as discussed in section 3.3). The trajectory of the scattered particle is traced back (starting from the chamber hit closest to the center of CHAOS), by solving the equations of motion based on the assumption that the field is constant over small intervals (ie: 0.5 mm). The vertex is then determined by calculating the intersection of the scattered track and incoming beam trajectory.

The equations of motion for a charged particle in a magnetic field are given by equation 8.73. In the region of the target, $\vec{B}$ has no components in the x-y plane. Solving the above system of equations given that the magnitude of $\vec{B}$ is constant over a small interval s, results in

$$P_x(t) = P_{y0}\sin(\omega) + P_{x0}\cos(\omega) \tag{8.85}$$

$$P_y(t) = P_{y0}\cos(\omega) - P_{x0}\sin(\omega) \tag{8.86}$$

$$\omega = \frac{qBt}{\gamma m} \tag{8.87}$$

$$= \frac{qBtv}{\gamma mv} = \frac{qBs}{P} \tag{8.88}$$

where P_{x0} and P_{y0} are the x and y components of the momentum at the starting point. q, P, and v are the charge and magnitude of the momentum and velocity of the outgoing particle, respectively. In addition, B is the magnetic field strength at the starting point, which is obtained using the CHAOS magnetic field map. Integrating equations 8.85 and

8.86 with respect to time gives [3]

$$x = \frac{P_{y0}}{qB}[1-\cos(\omega)] + \frac{P_{x0}}{qB}\sin(\omega) + x_0 \tag{8.89}$$

$$y = \frac{P_{y0}}{qB}\sin(\omega) - \frac{P_{x0}}{qB}[1-\cos(\omega)] + y_0 \tag{8.90}$$

$$\omega = \frac{qbs}{P} \tag{8.91}$$

where (x, y) is the position of the particle calculated by taking a single step s from the initial point (x_0, y_0).

The above procedure determines the scattered particle trajectory in the region of the target. The following quantity is computed at each point on the traceback:

$$d(x,y) = (x-a)^2 + (y-b)^2 - R^2 \tag{8.92}$$

In the above, (a, b) and R are the center coordinates and radius of the circle that defines the incoming beam track. The intersection of the two tracks occurs when d vanishes. Due to roundoff errors and the finite size of the step, d is often small but nonzero. As such, the vertex is the average of the points between which the sign of d changes.

Once the horizontal vertex coordinates have been found, the vertical coordinate of the interaction point is obtained in the following manner. A straight line fit is performed on the z-coordinate versus the distance (in the x-y plane) from the interaction vertex to the hits in WC1, WC2 and the activated resistive wires in WC4. The vertical coordinate of the vertex is the y-intercept of the fit line.

The scattering angle is defined as follows:

$$\theta_s = \cos^{-1}(\hat{k}_{in} \bullet \hat{k}_{out}) \tag{8.93}$$

where $\hat{k}_{in}$ is the unit vector pointing along the tangent to the incoming beam track at the vertex. Similarly, the unit vector, $\hat{k}_{out}$, points along the tangent to the scattered track at the interaction point.

[3] v is a constant.

8.3 Results

The results presented in this section are primarily concerned with π^+p reaction data acquired at an incident pion energy of 280 MeV with 0.5 T field, a singles trigger and a liquid hydrogen target.

Figure 8.44 shows the track momenta as a function of the sum of the pulse heights in ΔE_1 and ΔE_2. Pions and protons are well separated. The proton pulse heights display a strong dependence on the momentum. This is to be expected since protons with lower momenta produce a larger pulse height; however, at some point the proton momentum becomes too small causing the particles to stop in the scintillator. As a result, a smaller signal is produced. The pions, on the other hand, have a much smaller mass and hence are minimum ionizing; thus, very little correlation between the pion pulse height and momentum is seen. Placing a box cut on this scatter plot separates pions from protons.

A diagram of the liquid hydrogen target is shown in figure 8.45; the radius of the target cell is 25.5 mm. Figure 8.46 shows the interaction vertex in the x-y plane. The reconstructed vertex is consistent with the physical dimensions of the target vessel; the non-circular shape in Y is due to the fact that the beam envelope is smaller than the target. The vertex resolution is obtained by calculating the difference between the vertices for the pion and proton tracks in a given event. Figure 8.47 shows these values for x and y dimensions; both peaks are centered very close to zero. As expected, the resolution along the direction of the beam (in this case along the x-axis) is worse than that perpendicular to the beam direction. This is because the πp cross section is peaked at forward angles; hence often either the pion or the proton tracks emerge at small angles with respect to the incident beam. Due to the small angle, these tracks have a large overlap region with the incident beam trajectory which causes a broadening of the peak along the beam direction (for a given spatial resolution, it is much harder to intersect two nearly parallel

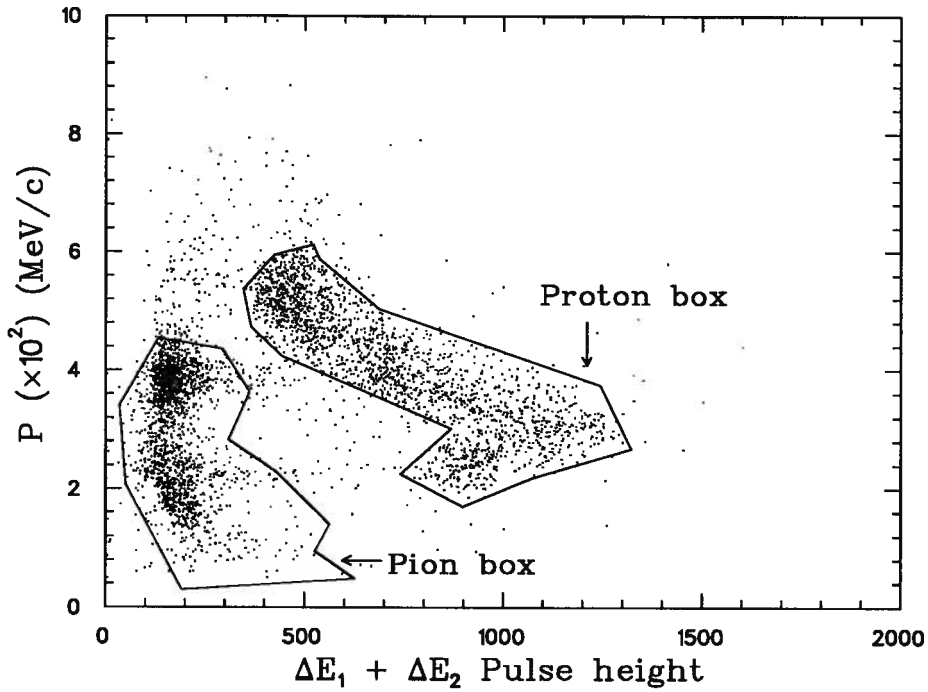

Figure 8.44: Scatter plot showing track momenta as a function of sum of pulse heights in ΔE_1 and ΔE_2. The polygons are used to identify pions and protons.

lines than two perpendicular lines). The resolution for a single track is obtained by dividing each of the standard deviations in figure 8.47 by $\sqrt{2}$. The vertex resolution for a single track along the direction of the beam is 1.54 mm and perpendicular to the beam direction is 0.30 mm. The above technique could not be used to obtain the vertical vertex resolution, because at the current WC1 operating voltage, the cathode strips are highly inefficient. In order to obtain vertical resolution of the vertex, data were acquired with a "picket fence" target which consists of three horizontally mounted thin (2mm diameter) rods (see figure 8.48). Figure 8.49 shows the vertical profile of the picket fence target. Althoughnot many counts are present, the three peaks corresponding to the rods

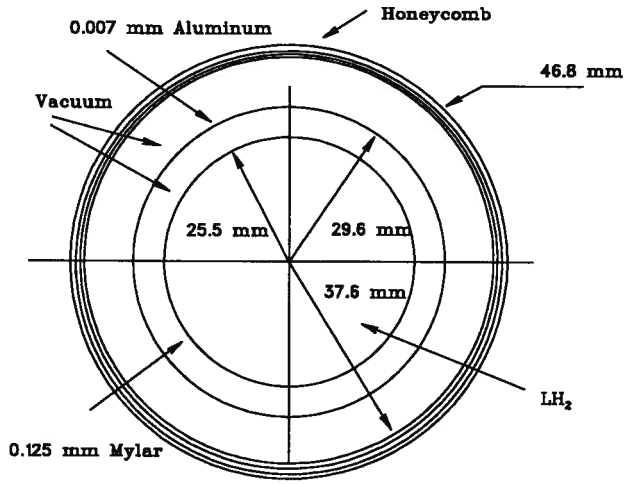

Figure 8.45: Illustration of the target vessel in the X-Y plane.

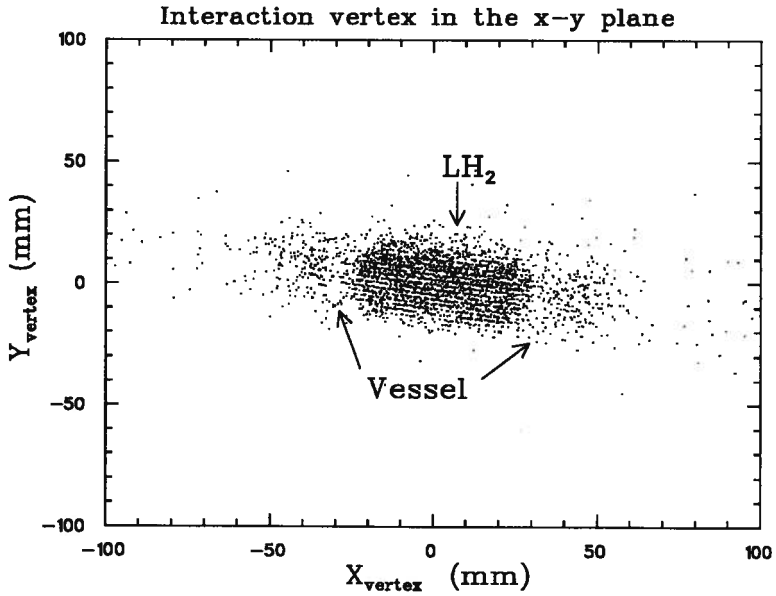

Figure 8.46: Reconstructed interaction vertex in the X-Y plane.

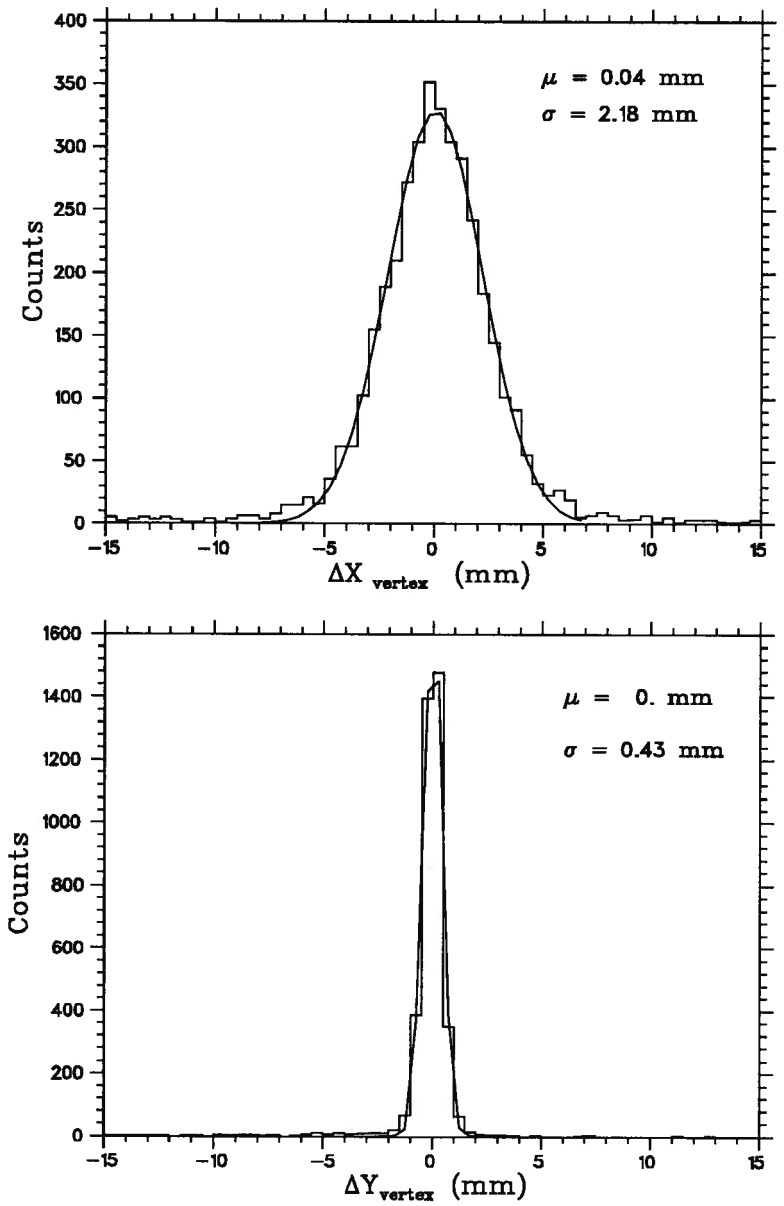

Figure 8.47: The difference between pion and proton vertices in the X-Y plane are shown. The solid lines represent gaussian fits to the data. The vertex resolution per track is obtained by dividing the standard deviations shown above by $\sqrt{2}$.

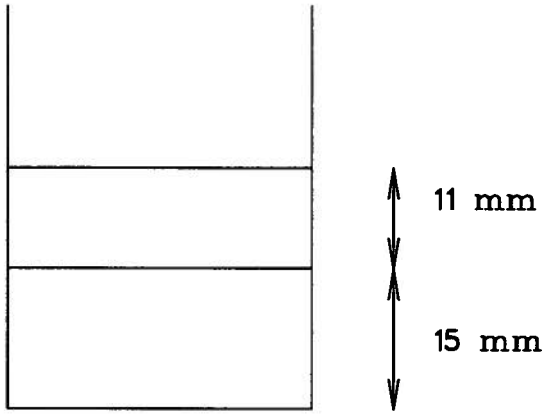

Figure 8.48: Illustration of the vertical picket fence target.

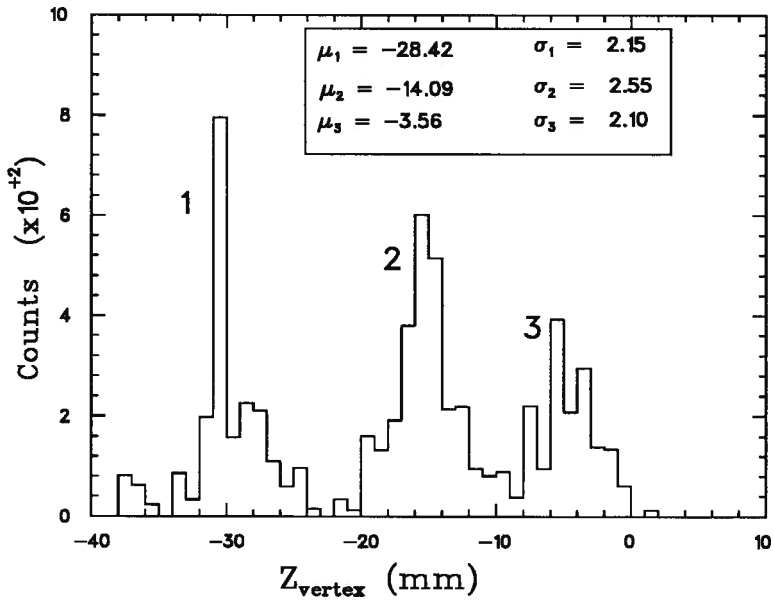

Figure 8.49: Vertical vertex reconstruction for the picket fence target. The three peaks correspond to the three (2 mm diameter) rods.

are seen and the separation between them is consistent with the physical dimensions of the target; for each peak, the mean (μ) and standard deviation (σ) correspond to the statistical ones and were not obtained via a gaussian fit to the data. Using the average of the standard deviations shown in 8.49, the vertical resolution is 2.26 mm. However, the resolution and efficiency will be improved by increasing the WC1 operating voltage. In addition to being inefficient, the WC1 cathode strip signal to noise ratio is too small at the present voltage. Furthermore, the resolution of the vertical coordinate in WC1 and WC2 is related to the efficiency, because the technique used to obtain the z-coordinate of the track relies on having two or more strips fire for optimum resolution.

Figure 8.50 shows a plot of scattering angle versus momentum for elastically scattered pions and coincident recoil protons at 280 MeV pion incident energy. A large fraction of the background due to the target vessel has been removed by placing a cut on the location of the interaction vertex. The solid line shows the kinematic predictions, which are consistently high because the magnitude of the central field is not correct. The field value obtained from the NMR probe situated on the pole tip does not reflect the central value at which the field map was constructed. The disagreement between the data and the kinematics is on the order of 5%. Increasing the field by this factor results in figure 8.51, in which scattering angle versus momentum correlations for both the pions and protons are consistent with the kinematic predictions. All of the data points shown correspond to events in which the scattered pion and the recoil proton were both detected. This is the reason for the limited kinematic range shown in figure 8.51. Both extreme forward and back angle scattered pions pass through the regions of the beam entrance and exit, where the CFT trigger blocks have been removed. Furthermore, the recoil protons corresponding to forward scattered pions have low momenta; consequently they too will not arrive at the CFT. Similarly, forward scattered protons exit through the region of CHAOS where the blocks have been removed. The plots in figure 8.51 demonstrate that

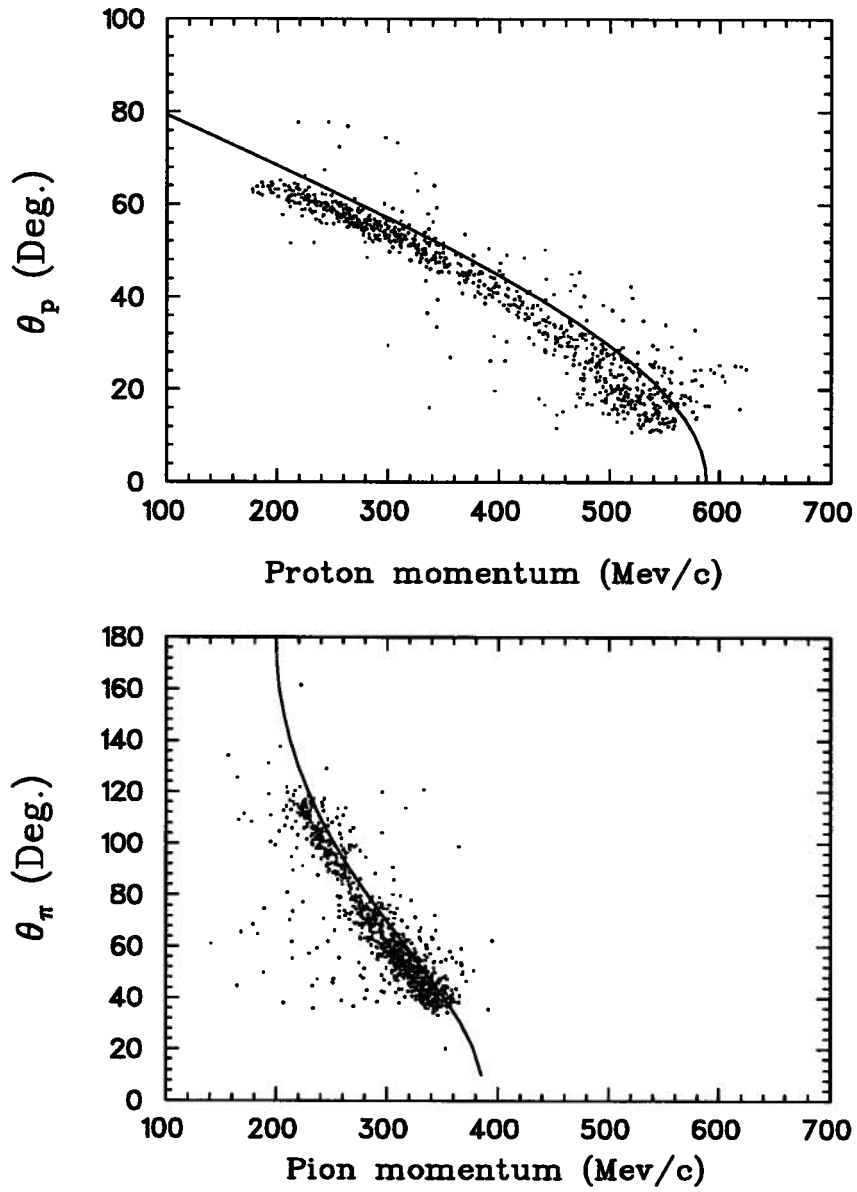

Figure 8.50: Scattering angle versus momentum correlation for pions and protons at 280 MeV pion incident energy prior to scaling the magnetic field are shown. The solid lines represent kinematic predictions.

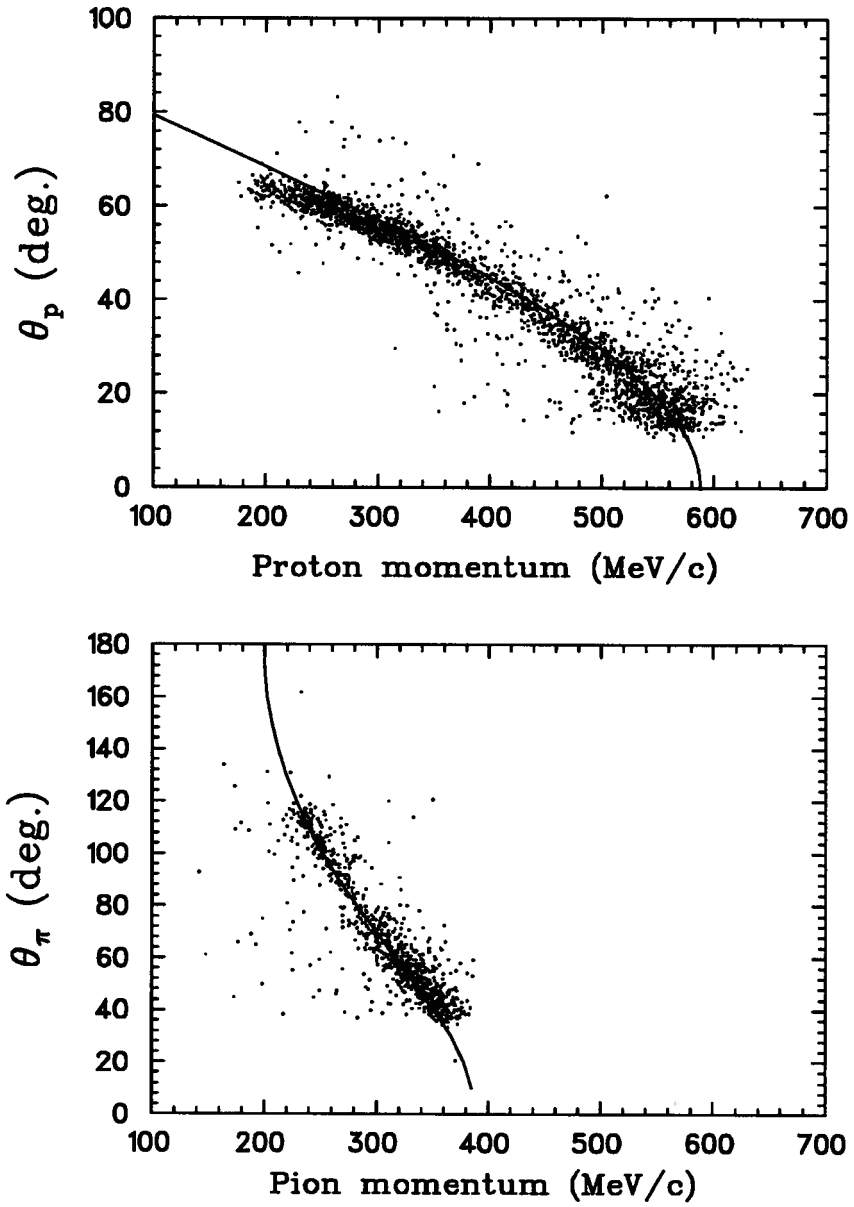

Figure 8.51: Scattering angle versus momentum correlation for pions and protons after scaling the magnetic field (by +5%) are shown. All other features are the same as those for figure 8.50.

the CHAOS detector is working as expected. Figure 8.52 shows the pion scattering angle as a function of the proton scattering angle. The solid line represents the kinematic predictions, and there is good agreement between the data and kinematics.

The scattering angle resolution is determined by calculating the difference between the predicted and calculated scattering angle of the proton at a given pion angle, as shown in figure 8.53. The scattering angle resolution for a single track is obtained by dividing the standard deviation of the distribution in figure 8.53 by $\sqrt{2}$. The calculated scattering angle resolution for a single track is $0.51°$.

Figure 8.54 shows the missing mass histogram for πp scattering; once again, a cut is placed on the location of the vertex. For the data presented in figure 8.54, the recoil proton and the scattered pion were not required simultaneously. The missing mass, Δm, is defined as

$$\Delta m = E_{in} + m_p - E_{out} \tag{8.94}$$

where m_p is the proton mass and E_{in} is the total energy of the incident pion beam. In addition, E_{out} represents the total energy of the outgoing particle(s). The missing mass should be zero for events where both the pion and proton tracks were correctly identified and reconstructed. A nonzero missing mass is expected if either the pion or proton were not detected.

Figure 8.55 shows the missing mass spectra plotted against the sum of the pulse heights in ΔE_1 and ΔE_2. It is clear that region 1 in figure 8.54 corresponds to those events in which the pion was not detected. The region starts at an energy greater than the rest mass of the pion because the scattered pion kinetic energy is nonzero. Furthermore, the width of this interval does not violate kinematical constraints which limit the range of pion kinetic energy. The pions will not be detected if scattered at extreme forward or back angles, where the CFT blocks are removed and WC4 is deadened. Chamber

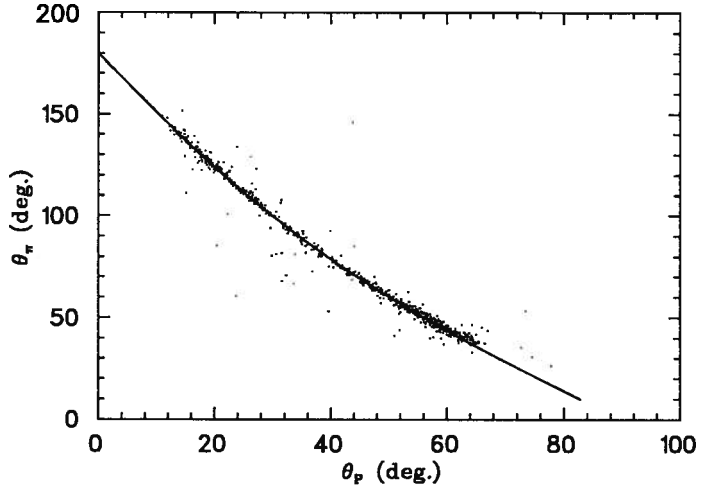

Figure 8.52: Pion versus proton scattering angle at 280 MeV incident pion energy. The solid line represents kinematic predictions.

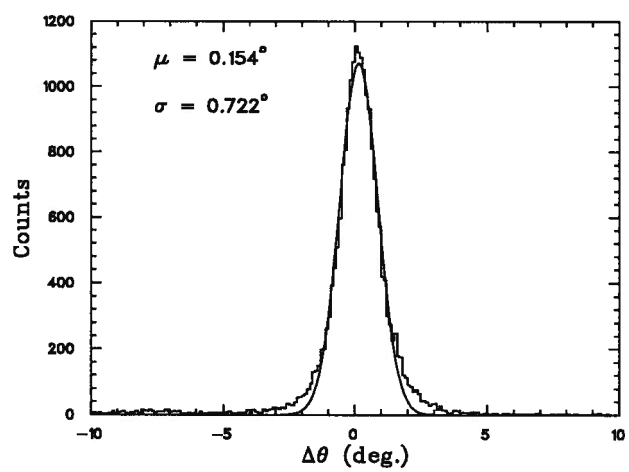

Figure 8.53: Histogram showing the scattering angle resolution. The scattering angle resolution per track is obtained by dividing the standard deviation shown above by $\sqrt{2}$.

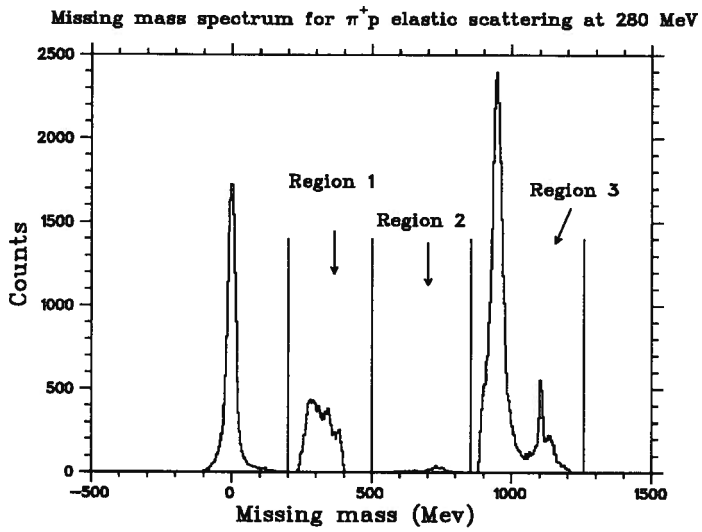

Figure 8.54: Missing mass spectrum for π^+p elastic scattering at 280 MeV.

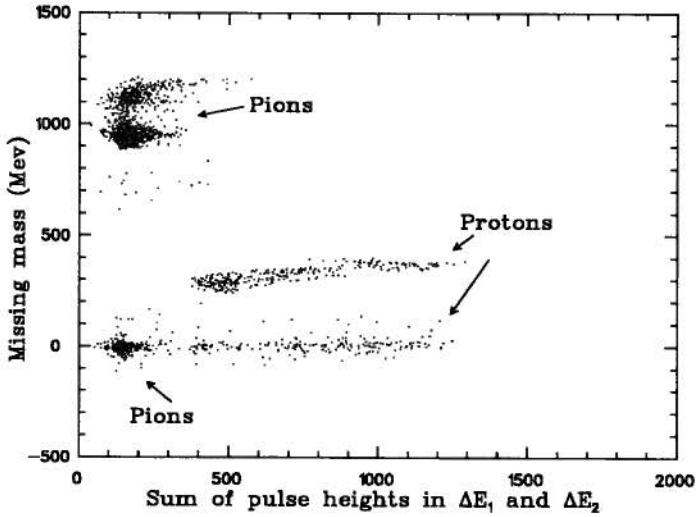

Figure 8.55: Missing mass spectrum versus sum of pulse heights in ΔE_1 and ΔE_2.

inefficiency, pion decay and reconstruction inefficiency also contribute to pion loss.

Region 3 of the missing mass histogram is caused by those events in which the recoil proton was not detected. The large peak in region 3 corresponds to the recoil protons which did not have enough kinetic energy to arrive at one of the CFT blocks. This occurs when the pion is scattered at forward angles. For example, consider a pion with 300 MeV incident energy that is scattered at an angle of 30°; the corresponding proton angle is 70°. At this angle, the proton energy is under 20 MeV and it will not arrive at any of the CFT blocks. Figure 8.56 shows a plot of pion scattering angle versus region 3 of the missing mass spectrum, and evidently the large peak corresponds to small pion scattering angles. The centroid of this peak is located at $\sim$ 947 MeV, which is near the proton rest mass. The smaller peak in region 3 corresponds to events in which the pion is scattered at back angles causing the proton to exit through a missing block section at forward angles. The data points appearing between the extreme forward and back angles correspond to those events in which the recoil protons were missed due to chamber and reconstruction inefficiencies. The counts that appear in region 3 between $\sim$ 1100 and 1300 MeV are muons from pion decay upstream of the target, and the momentum of these tracks is about 185 MeV/c. The CFT counters are not capable of separating pions and muons; hence these particles were identified as pions. Several tests were done in an attempt to gain an understanding of these events, and various processes were ruled out. The momentum versus scattering angle correlation for these points is not consistent for either π^+p protons or pions (see figure 8.51). In addition, the momentum of these tracks is too low to be due to pion scattering from heavier nuclei in the target vessel, which was not removed by the vertex cut. Figure 8.58 shows the vertical coordinate of the interaction vertex for these decay events as well as πp scattered pions. The peaks appearing in the vertex histogram of the decay events correspond to two copper disks that provide support for the 0.125 mm mylar window (see figure 8.57). These peaks are

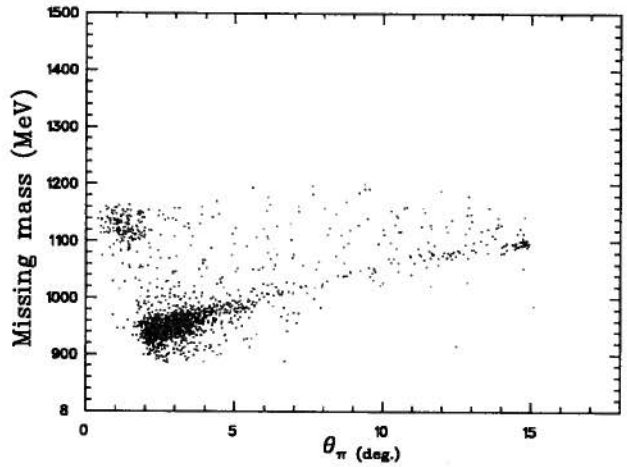

Figure 8.56: Region 3 of the missing mass histogram versus pion scattering angle.

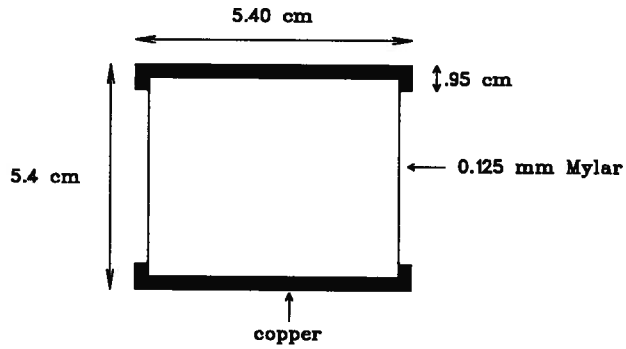

Figure 8.57: Diagram showing the copper support disks around the target cell.

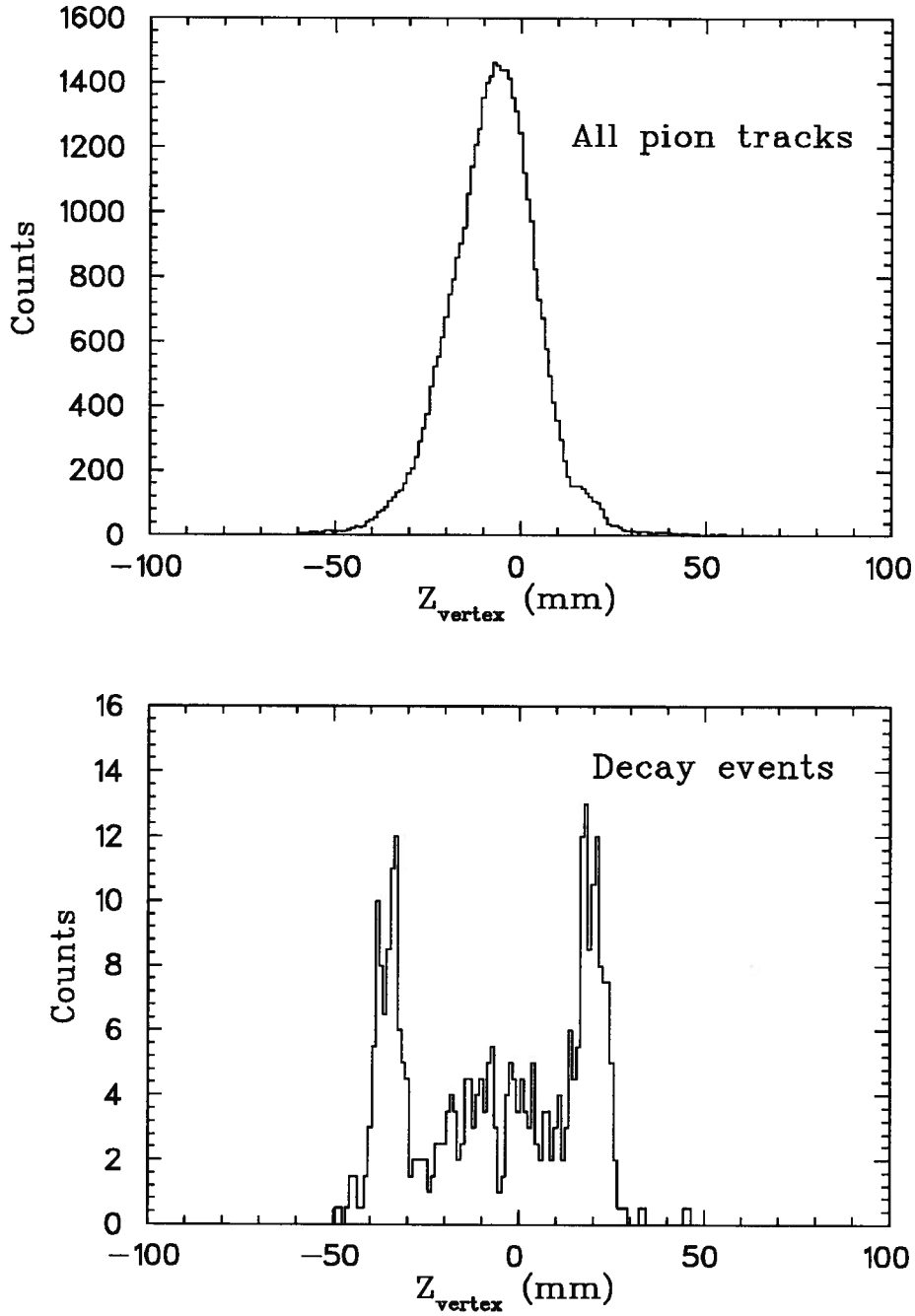

Figure 8.58: The vertical vertex for πp scattered pions (top) and decay events (bottom) are shown.

caused by those events in which the incident pion decays upstream of the target and the resulting muon passes through the copper disk. The kinetic energy of a 185 MeV/c muon is 107 MeV, and the energy lost by a muon resulting from the decay of 396 MeV/c pions in copper is less than 66 MeV [4]. The above suggests that the incident muon energy is less than 173 MeV, which is consistent with the kinematics describing pion decay at 396 MeV/c. Consequently, it seems reasonable to attribute these counts to those incident pions that decay before the target into muons whose trajectories pass through the disks.

Region 2 corresponds to misidentified particles. Figure 8.59 shows region 2 of the missing mass spectrum on a magnified scale; the momentum spectrum corresponding to these events is also shown. The spectrum shows two peaks which are centered around 200 and 360 MeV/c. All of the counts in the momentum histogram were identified as pions (see figure 8.55). Calculating the missing mass based on this assumption yields a value of 728 MeV, which is consistent with the centroid of the peak in region 2. Now consider the case in which one of the tracks (with momentum 200 MeV/c) was a proton but was identified as a pion. If the proton mass and the second pion track (one with momentum 360 MeV/c) are used in the calculation, the missing mass obtained is less than 15 MeV. Hence, particle misidentification seems to be a plausible explanation for these events. The number of misidentified tracks is less than 1% of the total number of counts in the missing mass histogram. At this stage of the analysis the gain stabilization of the CFT's is still not optimized; however, this will be implemented in the near future.

The histogram of the scattering angle is interesting because the number of counts in each angular bin is proportional to the differential cross section at that scattering angle. The constant of proportionality, k, is given by

$$\frac{1}{d\Omega \epsilon_d \epsilon N_p N_\pi} \tag{8.95}$$

[4]This is roughly constant over the entire range of allowed momentum.

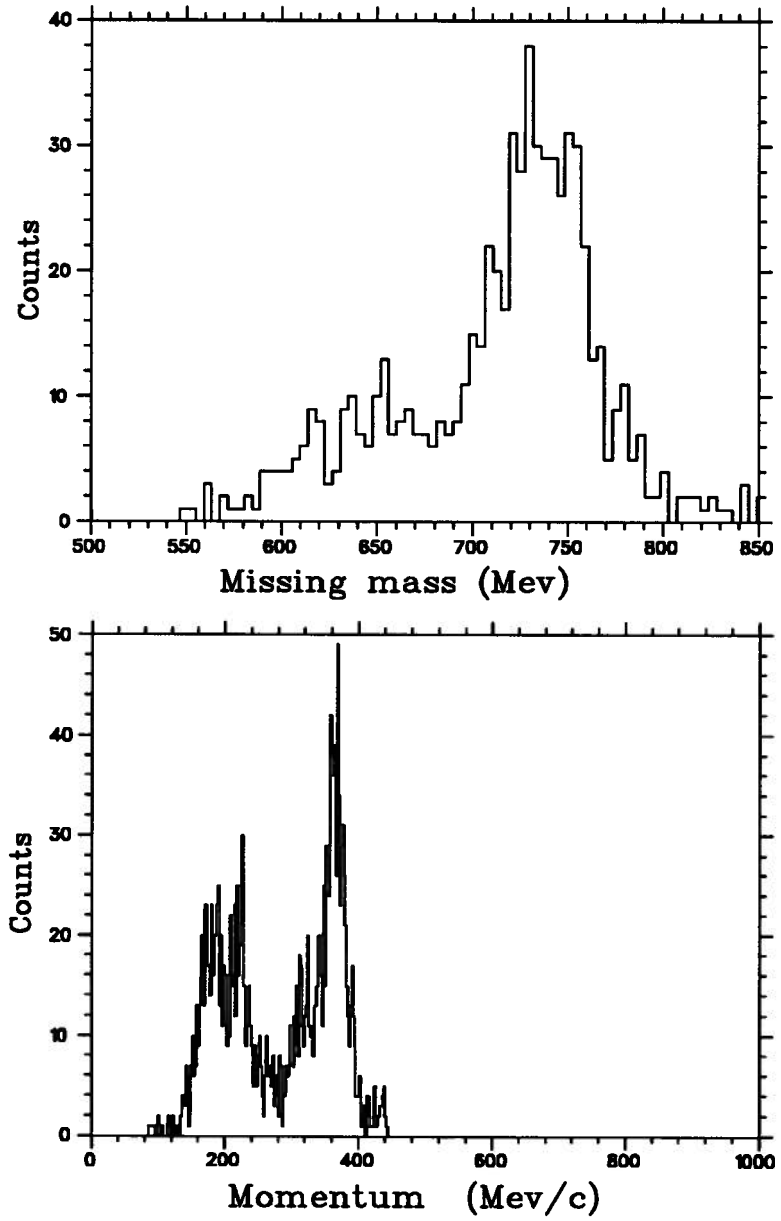

Figure 8.59: Region 2 of the missing mass spectrum on a magnified scale along with the corresponding momentum distribution are shown.

where $d\Omega$ is the solid angle; ϵ and ϵ_d are the computer and detection efficiencies respectively [5]. In addition, N_p is the number of target protons per unit area and N_π is the total number of incident pions. The accurate determination of some of these factors, such as the solid angle, is beyond the scope of this thesis; however, a rough estimate of k can be made. Figure 8.60 shows the π^+p cross sections at 280 MeV obtained from the SM92 phase shifts plotted on top of the scattering angle histogram, in which the counts obtained with CHAOS were scaled by a factor of 2.08×10^{-2} mb/sr.[6] The scaling factor was chosen so that the phase shift curve and the scattering angle distribution were in good visual agreement. The data shown in figure 8.60 were acquired with a singles trigger, and the recoil proton detection was not required in the software. The shape of the distribution is consistent with the cross section curve. The absence of counts at the extreme forward angles (near 0° and 360°) is caused by those events in which the pion is scattered into the beam exit where the CFT block was removed. The lack of counts around 180° is due to the missing block and the deadened sections of WC3 and WC4 at the beam entrance. The disagreement around 320° and 40° is due to faulty wires in WC3. Figure 8.61 shows a plot of the pion track angle in WC3 versus scattering angle; the faulty wires are clearly visible, and the projection of the dead wire regions onto the scattering angle axis explains the dips in the scattering angle distribution. The effect of dead wires in WC3 on the scattering distribution is a complex one that depends on the track momentum, the distribution of the beam over the target, and the number of tracks emerging from the target. If an outgoing track traverses a dead cell of WC3 and a second track is not present, the event will be rejected by the second level trigger. Near 300° the distribution is higher than the SM92 phase shift results. This effect is caused by

[5]The detection efficiency accounts for pion loss due to decay, reconstruction, and chamber inefficiencies.

[6]To separate the two halves of the detector, the scattering angle has been plotted between 0 and 360°.

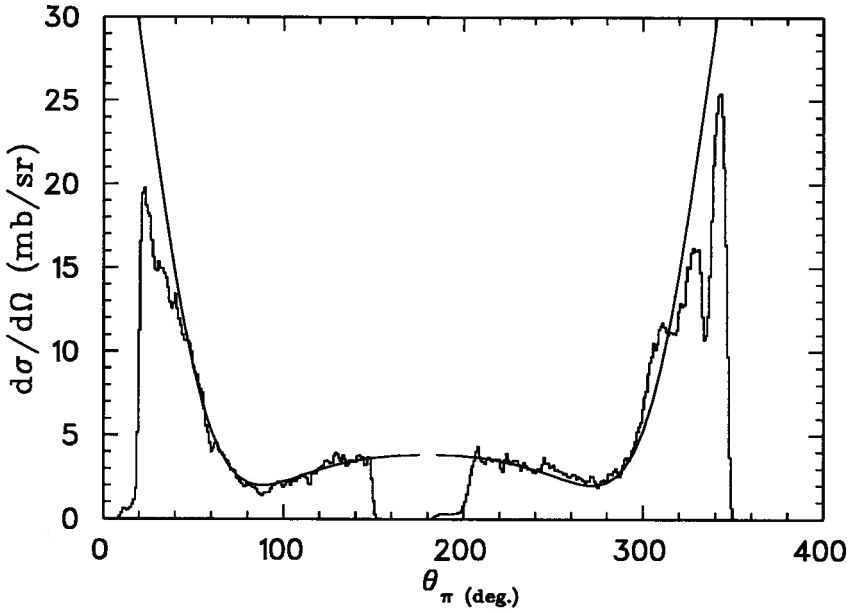

Figure 8.60: Cross sections for π^+p elastic scattering at 280 MeV incident pion energy. The solid line represents the SM92 phase shift results.

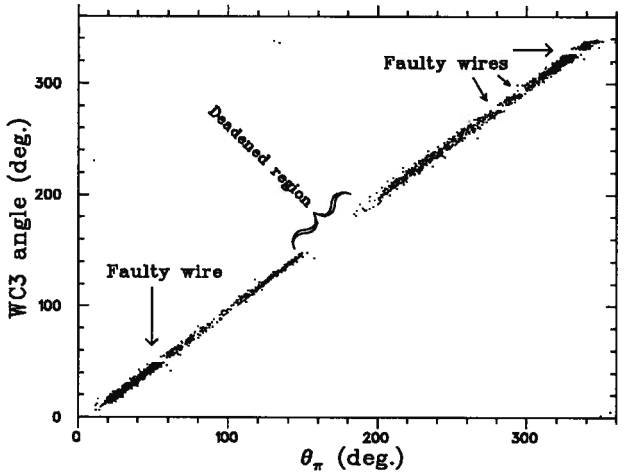

Figure 8.61: Track angle in WC3 versus pion scattering angle.

a defective CFT block which resulted in some of the proton tracks being misidentified as pions. Using separate particle identification cuts for this particular block minimized but did not eliminate the problem. Implementation of the CFT gain stabilization in software in the analysis package will virtually eliminate particle misidentification.

Now consider making a rough estimate of the constant k. The solid angle for a one degree polar angle bin is given by

$$d\Omega = \int_0^{\frac{\pi}{180}} d\theta \int_{\frac{83\pi}{180}}^{\frac{97\pi}{180}} \sin(\phi) d\phi = 0.00425 \ sr \tag{8.96}$$

The above equation is the expression for the solid angle given that the azimuthal angular acceptance of CHAOS is 14 degrees, as estimated from the width of the vertical position distribution in WC4 for $\pi^+ p$ events (fringe field effects were ignored). The combined efficiency of the chambers and reconstruction along with scattered pion loss due to decay is obtained by considering a region in the proton scattering angle distribution for which the pion should have been detected. For this angular region, any counts appearing in the missing mass spectrum which correspond to missing pions are due to chamber inefficiency, reconstruction inefficiency or scattered pion decay. This method determines that the combined efficiency is 73%. The combined chamber efficiency expected from the plateau curves is 75%. In the calculation of this quantity, efficiencies of WC1 and WC2 for both the incoming and scattered tracks must be taken into consideration, since the vertex reconstruction algorithm requires the presence of WC1 and WC2 hits for both the incoming and outgoing particles (WC4 was assumed to be 100% efficient). Comparison of the combined efficiency with that of the chambers suggests that the reconstruction algorithms are 99% efficient, accounting for an expected pion decay of $\sim$ 2%.

The computer dead time is calculated from the following relation:

$$\epsilon = \frac{N_t - N_c}{N_{pass} - N_c} \tag{8.97}$$

where N_t is the total number of events accepted by the first level trigger and N_{pass} is the total number of events which were allowed through the computer busy circuit to the second level trigger. In addition, N_c represents the total number of calibration events. These do not correspond to physical interactions and are generated for calibration purposes only. Hence, they must be subtracted from both the denominator and the numerator. For the data shown in figure 8.60 the computer efficiency was 1.7%.

The number of incident pions is computed using the total counts obtained from a plastic scintillator mounted approximately 2 meters upstream from the target in which an upper level discriminator setting removed the 20% proton contamination of the π^+ beam from the trigger. Let the number of counts from the scintillator be N_s; the number of incident pions is given by

$$N_\pi = N_s \times f_\pi \times (1 + f_d) \times (1 - f_{decay}) \times f_{tgt} \tag{8.98}$$

where f_π is the pion fraction of the beam, f_{decay} is the fraction of pions that decay before hitting the target and f_{tgt} is the fraction of the beam which hits the target. In addition, f_d is the doubles fraction of the beam, which represents the probability of having two pions in the target at the same time. In such cases, the beam counting scintillator would register only one count.

Since only a single in-beam scintillator was used, some of the above parameters, in particular f_{tgt}, are estimates obtained from previous runs that employed an active scintillating target. The same momentum and magnetic field settings were used, and the scintillating target was roughly the same size as the liquid hydrogen one. In addition, a single in-beam counter causes N_π to be susceptible to fictitious counts produced by activation of the scintillator and tube noise. Values of the above parameters for a 396 MeV/c positive pion beam arriving at the in-beam scintillator at a rate of 1.4 MHz are listed in table 8.3.

f_π	0.99
f_d	0.03
f_{decay}	0.02
f_{tgt}	0.61
N_s	6.915×10^9
N_π	4.22×10^9

Table 8.2: Table showing beam calculation parameters for 396 MeV/c π^+ at 1.4 MHz.

In order to determine the number of target particles per unit area, the effective target thickness must be known. Since the target cell was cylindrical, the beam profile is required to determine this quantity. The thickness of a cylinder of radius R, at a distance r from the center (see figure 8.62) is given by

$$d(r) = 2\sqrt{R^2 - r^2} \tag{8.99}$$

Assuming that the beam curvature is negligible over the target diameter, the effective target thickness, t, is obtained from the following relation:

$$t = \frac{\int_{-R}^{R} f(r)d(r)}{\int_{-\infty}^{\infty} f(r)} \tag{8.100}$$

where f(r) is the beam profile as a function of the distance from the center of the target, and is obtained from the target projection histogram which represents the beam projection on a plane oriented perpendicular to the incident beam. The radius of the target cell was 25.5 mm, resulting in an effective target thickness of 47.02 mm. The number of protons per unit area is given by

$$N_p = \frac{2\rho t A}{2.0159} \tag{8.101}$$

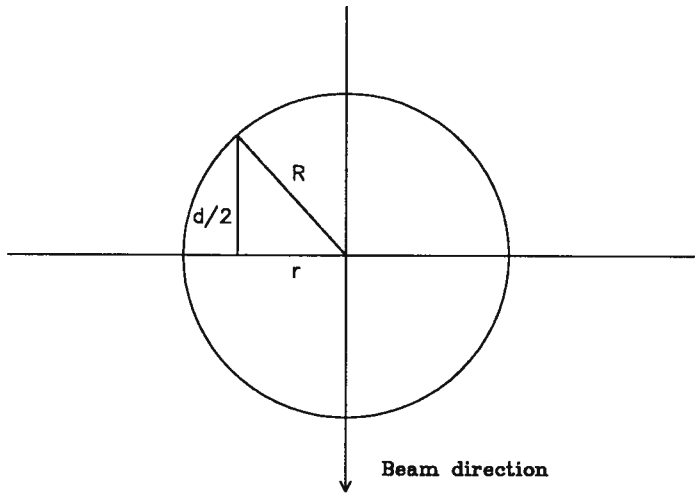

Figure 8.62: Illustration of $d(r)$.

where ρ is the target density in grams per cubic centimeter and A is Avagadro's number. The factor of 2 in the numerator is the number of protons in a hydrogen molecule and 2.0159 in the denominator represents the atomic weight of the hydrogen molecule. Given the target density of 0.074 gm/cm^3, the number of target particles per unit area was determined to be $2.078 \times 10^{23}\ cm^{-2}$. Using the parameters mentioned, the value of k was determined to be $2.16 \times 10^{-2}\ mb/sr$. There is a 2% discrepancy between the calculated and estimated values of k. However, given the crude nature of this calculation and the numerous simplifying assumptions, a relatively large uncertainty is associated with both values of k.

The aim of the above calculation is not to make a definitive absolute measurement of π^+p differential cross sections; it is simply meant as a semi-quantitative approach to the problem. Many parameters used in the calculation of k are rough estimates. For example, to completely eliminate scattering from the target vessel, background subtraction must be performed. Furthermore, accurate determination of the solid angle requires extensive

Monte Carlo simulations, which are currently underway. Over all, the above results are encouraging and seem to indicate that the CHAOS spectrometer is operating as expected. Figure 8.60 indicates that there is reasonable symmetry between the two halves of the spectrometer, which is perhaps the most important result of the above calculation.

It is impressive to note that the entire angular distribution shown in figure 8.60 was acquired with CHAOS in a single 45 minute long period of data acquisition. Were it not for the poor computer efficiency, the same data could have been acquired in about 1 minute.

Chapter 9

Conclusion

The results presented in this thesis clearly indicate that the CHAOS spectrometer has been a success. The preliminary momentum resolution as calculated for a 225 MeV/c π^+ beam at a magnetic field setting of 1.2 T is 1% (σ). Much has been learned from the commissioning results which will help improve the momentum resolution. An increase in the operating voltage of WC1, the implementation of the three dimensional momentum reconstruction algorithm, the application of magnetic field corrections to WC4 x(t) relations, and the reduction of multiple scattering by placing helium bags between the chambers are thought to increase the resolution. The horizontal resolution of WC1 will also be enhanced by raising the operating voltage since it will increase the fraction of events in which more than one wire per track is activated. Furthermore, the higher operating voltage will increase the cathode strip efficiency and signal to noise ratio, which will greatly enhance the vertical vertex resolution and efficiency.

In order to obtain an accurate vertical projection of the beam onto the target, separate ADC gates must be supplied to the FASTBUS system. This will be implemented in the next CHAOS beam period in January of 1994. Clearly the computer live time of 1.7% is unacceptable. Improvement of the computer efficiency is one of the major goals targeted for the next CHAOS running period, which we expect to accomplish by replacing the existing CAMAC based data acquisition system with one based on VME.

In future experiments, the number of incoming pions must be obtained using two in-beam scintillators in coincidence, which will virtually eliminate fictitious counts produced

by scintillator activation and tube noise. In addition, the fraction of the beam arriving at the target can be calculated accurately if the second scintillator is placed closer to the target. Although a cut placed on the location of the interaction vertex minimizes scattering from the target vessel, background runs with an empty target (only the vessel) are required to completely eliminate this problem. It is extremely difficult to correct the scattering angle distribution for dead wires in WC3; hence, in order to use the full angular coverage of the spectrometer, it is crucial that these channels be repaired. However, it is thought that corrections can be applied if Monte Carlo studies of the problem are performed. Furthermore, the implementation of the CFT gain stabilization software is essential for future analysis of experimental results.

It must be stressed that the CHAOS detector is new and as such further analysis is required in order to fully understand the data acquired with CHAOS. For example, extensive Monte Carlo analysis is required to model pion decay inside the spectrometer, which is a source of background.

The next set of CHAOS experiments are scheduled to begin in January of 1994 and will continue throughout the summer of that year. The first stage of the $(\pi, 2\pi)$ experiments has been completed and the analysis is currently underway. The second stage will begin in January 1994. The date for completion of the polarized target is the summer of 1994 at which time measurements of the πp analysing powers will begin. In conclusion, the CHAOS detector at TRIUMF offers a unique new facility for studying πN interactions which are crucial in testing low energy predictions of QCD.

Bibliography

[1] H.L. Anderson, E. Fermi, R. Martin and D.E Nagle Phys. Rev. **91**, 155 (1953).

[2] P.J. Bussey, J.R. Carter, D.R. Dance, D.V. Bugg, A.A. Carter and A.M. Smith, Nucl. Phys. **B58**, 363 (1973).

[3] P.Y. Bertin, B. Coupat, A. Hivernat, D.B. Isabelle, J.Duclos, A. Gerard, J. Miller, J. Morgenstern, J. Picard, P. Vernin, R. Powers, Nucl Phys. , **B106**, 341 (1976).

[4] E.G Auld, D. Axen, J.Beveridge, C. Duesdieker, L. Felawaka, C.H.Q. Ingram, R.R. Johnson, G.Jones, D. LePatourel, R Orth, M. Salomon, W. Westlund, L. Robertson, Can. J. Phys. **57**, 73, (1979).

[5] J.S. Frank, A.A. Browman, P.A.M. Gram, R.H. Heffner, K.A. Klare, R.E. Mischke, D.C. Moir, D.E. Nagle, J.M. Porter, R.P. Redwine, M.A. Yates, Phys. Rev. D, **28**, 1569, (1983).

[6] B.G. Ritchie, R.S. Moore, B.M. Preedom, G. Das, R.C. Minehart, K.Gotow, W.J. Burger, H.J. Zoik, Phys. Rev. Lett. **125B**, 128 (1983).

[7] J.T. Brack, R.A. Ristinen, J.J. Kraushaar, R.A. Loveman, R.J. Peterson, G.R. Smith, D.R. Gill, D.F. Ottewell, M.E. Sevior, R.P. Trelle, E.L. Mathie, N.Grion, R.Rui, Phys. Rev. C, **41**, 2202, (1989).

[8] J.T. Brack, J.J. Kraushaar, R.J. Peterson, R.A. Ristinen, D.R. Gill, R.R. Johnson, D.F. Ottewell, F.M. Rozon, M.E. Sevior, G.R. Smith, F. Tervisidis, R.P. Trelle, E.L. Mathie, Phys. Rev. C, **34**, 1771, (1986).

[9] Data obtained from the SAID data base on the TRIUMF computer cluster.

[10] Renton, Peter, **Electroweak Interactions** Cambridge University Press, Cambridge, (1990).

[11] Ulf-G. Meissner, **Chiral Perturbation Theory With Nucleons**, Lectures given at summer school on Nucleaons and Nuclear Structure, Institute of Nuclear theory, University of Washington, Seattle, USA, (1991).

[12] Donoghue, John F., **Chiral Symmetry As an Experimental Science**, Lectures presented at the International School of Low-Energy Antiprotons, Erice, (1990).

[13] Sauli, F., **Principles of Operation of Multi Wire Proportional and Drift Chambers**, Lectures given in the Academic Training Programme of CERN, (1975-76).

[14] G. Charpak, R. Bouclier, T. Bressani, J. Favier, C. Zupancic, Nucl. Instr. Meth., **62**, 235, (1968).

[15] R. Veenhof, **Garfield: a drift vhamber simulation program**, v.3.0, CERN program library entry W5050, (1991).

[16] G.J. Hofman, J.T. Brack, P.A. Amaudruz, G.R. Smith, Nucl. Instr. Meth., **A325**, 384, (1993).

[17] This is an alloy of Ni obtained from California Fine Wire Company.

[18] G.C. Barbarino, L. Cerrito, G. Paternoster, S. Particelli, Nucl. Instr. Meth. ,**179**, 353, (1981).

[19] C. Bino, R. Mussa, S. Palestini, N. Pastrone, L. Pesando, Nucl. Instr. Meth., **A271**, 417, (1988).

[20] A. Fainberg, N. Horwitz, I. Linscott, G. Montei, Nucl. Instr. Meth., **141**, 277, (1976).

[21] P. Camerini et. al., paper submitted to Nucl. Instr. Meth., (1993).

[22] S.J. McFarland, M.Sc. thesis, UBC, (1993).

[23] G.J. Hofman, Internal CHAOS document, (1992).

[24] H. Wind, Nucl. Instr. Meth., **115**, 431, (1974).

[25] R. Tacik, Internal CHAOS document, (1992).